Intrinsically Microporous Polymer Materials for Electrodes and Membranes

Rong, Yuanyang

Award date:
2017

Awarding institution:
University of Bath

Intrinsically Microporous Polymer Materials for Electrodes and Membranes

Yuanyang Rong

The thesis submitted for the degree of Doctor of Philosophy

University of Bath

Department of Chemistry

March 2017

Signature: . . . . . Date: . . . . . .

Table of contents

Acknowledgements

Firstly, I would like express my sincere appreciation to my supervisor, Professor Frank Marken for his invaluable guidance and support. He leads me to the field of electrochemistry and gives me a lot of advice on my research work. He supports me to take part in various research activities, which provides me the chance to present my work. This thesis would not have been possible without his help. I am also grateful to Professor Neil. B. Mckeown, Dr. Richard Malpass-Evans and Dr. Mariolino Carta in University of Edinburgh for their advice and help. They provide the polymer materials for my experiments and also give a lot of useful suggestions.

I would like to thank Dr. Qilei Song in Imperial College for his help in making thin polymer films. The useful techniques provide much facility to experiments and generate new ideas. Also, I would like to thank Adam Kolodziej for his contributions as a visiting student towards the work of anion uptake in PIM films.

I would like to thank the help and support from all my colleagues, Elena Madrid, Daping He, Barak Aaronson, Sara Dale, Gabriela Kissling, Andrew Gross, Grace Lewis, Christopher Hotchen, Sunyhik Ahn and James Webster. In addition, I would like to thank John Mitchels and Ursula Potter for helping me to acquire high quality SEM and TEM images and teaching me how to use the equipment.

I would also like to thank all my good friends I met in Bath, Dr. Jiangning Gao, Miss Lian Fan, Mrs Wentao Deng, Miss Andi Di, Dr. Meng Li, Dr. Boyang Mao, Mr Xinxing Liang, Dr. Zexian Low, Dr. Daping He, for all the unforgettable moments and emotional support during my PhD study.

Last but not the least, I would like to express my deepest gratitude to my parents for their continuous support and encouragement throughout my PhD. Finally, I would like to thank University of Bath for fee waiver and China Scholarship for maintenance fees and provide me the opportunity to complete a PhD.

Abbreviations

Roman symbols

Symbol	Meaning	Units
a_j	Activity of species *j*	None
A	Area	m^2
C	Capacitance	F
C_j	Concentration of species *j*	mol m^{-3}
D_j	Diffusion coefficient of species *j*	m^2 s^{-1}
E	Potential	V
E°	Standard potential	V
$E^{\circ\prime}$	Formal potential	V
E_e	Equilibrium potential	V
F	Faraday's constant	96485 C mol^{-1}
f	Frequency	Hz
G	Gibbs energy of transition state	kJ mol^{-1}
ΔG	Change in Gibbs Free energy	kJ mol^{-1}
I	Current	A
j	Diffusional flux	mol m^{-2} s^{-1}
k	Rate constant	cm s^{-1}
k^0	standard rate constant	cm s^{-1}
m	Mass	kg
n	Stoichiometric number of electrons transferred	None
O	Oxidized species	None
Q	Charge	C
R	(i) Universal gas constant	8.314 J $K^{-1}mol^{-1}$
	(ii) Reduced species	None
	(iii) Resistance	Ω
T	Absolute temperature	K
t	Time	s
u	Ionic mobility	m^2 V^{-1} s^{-1}

ν	(i)	Kinematic velocity of solution	$m^2\ s^{-1}$
	(ii)	Scan rate	$V\ s^{-1}$
X_C	Capacitive reactance		Ω
W	Warburg impedance		Ω
Z	Impedance		Ω

Greek symbols

α	Transfer coefficient	None
γ	Activity coefficient	$mol^{-1}\ m^3$
δ	Diffusion layer thickness	m
η	Overpotential	V
θ	Phase angle of resistance	degree (or rad)
ϕ	Phase difference in AC potential	degree (or rad)
∅	Electrode potential	V
ω	Angular frequency	$rad\ s^{-1}$

Chemical abbreviations

AFM	Atomic-force microscopy
CE	Counter electrode
cPIM	Carbonized PIM
C-PIM	Carboxylated PIM
FeTPP	Tetraphenylporphyrinato-iron
Fc	Ferrocene
FESEM	Field emission scanning microscopy
GC	Glassy carbon
HOMO	Highest occupied molecular orbital
Hatn	5,6,11,12,17,18-hexaazatrinapthylene
ITO	Indium tin oxides
LUMO	Lowest unoccupied molecular orbital

MTZ	Methyl tetrazole
PIM	Polymers of intrinsic microporosity
Pc	Phthalocyanine
PPP	4-(3-phenyl-propyl)-pyridine
PET	Poly-ethylene-terephthalate
RE	Reference electrode
RDE	Rotating disk electrode
S	Sensor electrode
SEM	Scanning electron microscopy
SAXS	Small angel X-ray scattering
TZ	Tetrazole
TEM	Transmission electron microscope
WE	Working electrode
XPS	X-ray photoelectron spectroscopy
EA	Ethanoanthracene

Abstract

Microporous materials have received much attention and offer new opportunities in electrochemistry because of their interesting properties. Compared with the corresponding nonporous materials, the highly porous structure may facilitate internal mass transport process, provide accessibility to binding sites and provide size selectivity. A new class of microporous materials, polymers of intrinsic microporosity (PIMs) emerged about ten years ago. They combine the microporosity generated from the rigid and contorted backbones and the processibility of linear molecular polymers, which make them particularly attractive for the applications in gas storage, membrane separations and also in electrochemistry. PIM-EA-TB containing ethanoanthracene (EA) and Tröger's base (TB) is one of the most interesting PIMs and has a high BET surface area around 1000 $m^2 g^{-1}$. Most of the work in this thesis are based on PIM-EA-TB. Results chapters focus on catalysis in PIM films, ion flux in free-standing PIM membranes and carbonization of PIM-EA-TB.

Electrochemical oxidation of glucose is important due to the practical applications in glucose sensing and in biological fuel cells. However, the practical application of many catalysts is limited by the poisoning by interferences such as proteins and chloride. Here, PIM-EA-TB was spin-coated onto the surface of supported gold nanoparticles to protect the catalysts from poisoning. It was demonstrated that the PIM-EA-TB film would not negatively affect the catalytic performance of gold nanoparticles for glucose oxidation. Also, it provided effective protection against protein poisoning because of its rigid backbone and rigid molecular structure preventing protein access. Chloride poisoning was reduced but not surpressed.

In addition to nanoparticle catalysts, water-insoluble molecular catalysts were investigated. PIM-EA-TB was used as a rigid host for model catalyst, tetraphenylporphyrin (FeTPP). FeTPP was immobilised in the PIM-EA-TB film and then deposited on the electrode to create a high density heterogenised catalysts. Different compositions of PIM and FeTPP and different scanrates were investigated to reveal the catalytic mechanism. The PIM hosted FeTPP catalysts showed facile electron transfer and effective electrocatalytic reduction of oxygen and peroxide. The 4-(3-phenyl-propyl)-pyridine was applied to the PIM-FeTPP film to give an organogel in

order to investigate the liquid-liquid interface. The PIM immobilisation method could offer a new opportunity to the immobilisation of a wide range of the molecular catalysts.

The understanding of transport processes in PIM-EA-TB membranes is important for the development of further applications in the electrochemistry. Different types of anions were investigated to see the anion uptake and charge transport in PIM-EA-TB films. Three cases were investigated, including the oxidation of ferrocene, the reduction of protons and the transport of anions and protons in the PIM-EA-TB thick films. In all three cases, the diameter and hydrophobicity of anions are important in the competing effects. The pKa of PIM-EA-TB was determined and novel ionic diode effects were observed.

Nanofluidic devices are used to regulate the flow of ions to one preferential direction and they have great importance because of the similarity to biological ion channels and the application in biochemical fields. PIMs were explored to the possibility to establish an artificial ion channel with the gate function. A thin film preparative method was introduced to produce thin free-standing polymer films. The 300 nm PIM-EA-TB films supported on a poly-ethylene-terephthalate (PET) film with a 20 μm diameter microhole exhibited ionic diode behaviour. Only when the cation and anion had different mobility, the current rectification effects were observed. Different pH values of the electrolyte were also investigated and resulted in a gradual change in rectification effects.

Porous carbon materials have wide applications in different fields such as gas separation, water purification, catalyst supports, and fuel cells. One of the common methods to produce the porous carbon is the carbonization of polymers. However, the challenge is that it is difficult to control the pore size and pore distribution. PIM-EA-TB was carbonized at 500 °C in vacuum to produce a novel type of microporous carbon. The microporosity and morphology of the PIM precursor remained after carbonization. The new material exhibited relatively low electrical conductivity and low activity in the electrochemical oxygen reduction. The capacitance of the new carbon material was investigated and found to vary with pH depending on the protonation status of micropores.

Finally, the carbonized PIM films were used to control the formation of platinum nanoparticles. Platinum nanoparticles are important catalysts in many areas but may suffer from high costs and lack of reproducibility. Therefore, it is important to reduce the amount of platinum, increase the utilization of platinum as well as control the particle size. The carbonized PIM films still have the microporosity and offer an ideal substrate for platinum nanoparticles. The platinum nanoparticles were formed at the same time with the carbonization of PIM, which helped to control the size of platinum nanoparticles. Compared with bare platinum, the platinum nanoparticles produced by PIM-EA-TB showed a high electrochemically active surface area and good catalytic performances for oxygen reduction, methanol oxidation and glucose oxidation. Much less platinum (1μg per cm^2) was needed to achieve the same catalytic performance compared to the bulk platinum.

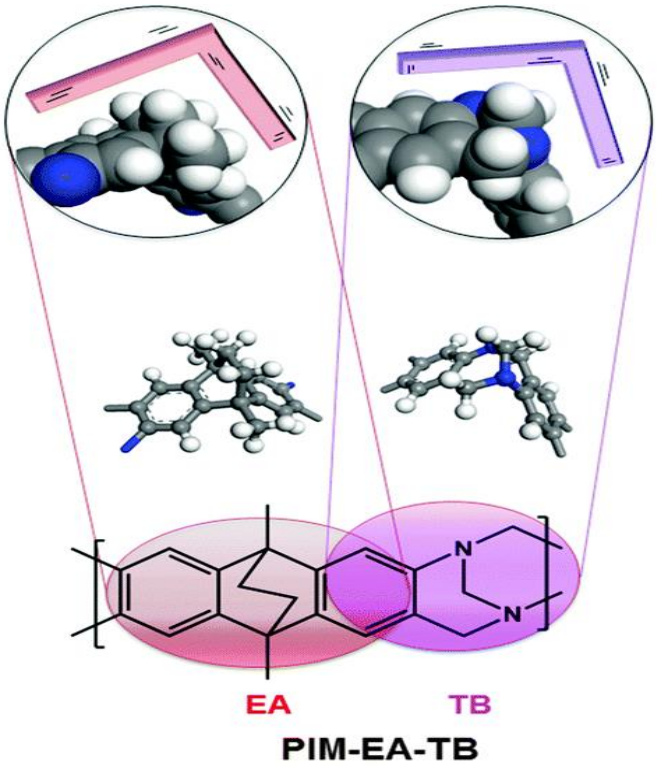

Aims

The aims of this thesis are:

- To investigate new applications of PIM-EA-TB in electrochemistry. The PIM-EA-TB film will be introduced into electrocatalytic system to explore catalyst stabilization, reactivity and poisoning. Different factors will be investigated and a model will be proposed to provide further insight into the effect of the PIM-EA-TB on the electrochemical mechanism.

- To provide a good substrate for water-insoluble molecular catalysts in aqueous solution. The composition and catalyst loading will be optimised to obtain good catalytic performance. This approach could facilitate the investigation of water-insoluble molecular catalysts for aqueous catalysis.

- To investigate the transport of anions and charge in the PIM-EA-TB films. Different types of electrolyte in three cases will be investigated to understand the transport mechanism. New experiments will be introduced to study the ionic diode effect of thick PIM-EA-TB membranes.

- To investigate the ionic diode effects of PIM-EA-TB thin membranes supported on the PET film with a single microhole. Different electrolyte solutions will be investigated on both sides of the membrane and a possible diode mechanism will be proposed.

- To produce a high surface area carbon material via vacuum carbonization of PIM-EA-TB. The carbon material will be characterized using a variety of techniques to determine its composition and morphology. The capacitance, conductivity and electrocatalytic activity of this material will also be investigated for further application.

- To develop a novel and simple method to produce high utilization metal nanoparticles catalysts based on PIM-EA-TB carbonization. The electrochemically active surface area and catalytic mass activity for platinum nanoparticles will be investigated compared with bare platinum.

Chapter 1: Introduction to Polymers of Intrinsic Microporosity (PIMs)

Chapter Abstract

New microporous materials have received considerable attention and may find wide ranges of applications in the long term. One of the emerging classes of microporous materials is a polymer-based organic material named polymer of intrinsic microporosity (PIM), which was first reported about ten years ago. PIMs possess the common properties of both conventional microporous materials and polymers, hence exhibit remarkable processibility and performances in various fields such as gas separation, gas storage, and catalysis. This chapter gives an overview of recent research developments with PIMs mainly regarding the classification and the applications of PIMs. One type of important PIM, PIM-EA-TB, which was synthesised by combining ethanoanthracene (EA) and a Tröger's base (TB), is highlighted due to its outstanding properties. PIMs offers a practical approach for the investigation of the relationship between performance and chemical structure including the pore design. The structural diversity of PIMs, which can be simply expanded by the choice of monomers and reaction conditions, remains largely unexplored and should have huge potential in future technologies.

1.1 Introduction

Microporous materials contain interconnected pores of dimensions < 2 nm and are of great importance as heterogeneous catalysts and adsorbents[1] due to their large and accessible surface area (typically 300-2000 m^2 g^{-1} as measured by gas adsorption). Conventional microporous materials include two main classes, crystalline inorganic frameworks (e.g., zeolites) and amorphous network structure (e.g., activated carbon)[2,3]. It has attracted much interests to synthesis the entirely novel microporous materials because of their wide potential for applications.

Particular interest has been focused on the construction of microporous materials from organic components, because organic-based materials allow precise control over the chemical structure, including the specific molecular sites and also the pore properties. It facilitates the investigation of the relationship between the structure and properties and then improve the synthesis of materials[4]. The past decade has seen great advances in organic porous materials, such as Yaghi's metal organic frameworks (MOFs)[5–7]and the structurally related purely organic covalent organic frameworks (COFs)[8,9]that mimic the structure of zeolites.

A novel class of high-free volume polymers termed polymers of intrinsic microporosity (PIMs) were first reported by Budd and McKeown in 2004[3,10]. It is this type of microporous organic materials that mimic amorphous structures of activated carbons, but in contrast to carbon, they are chemically well defined. In general, most polymers do not display classical microporisity because they have sufficient conformational flexibility to pack space efficiently and minimize the amount of void space. However, the PIMs exhibit large surface area of 500-1730 m^2 g^{-1} because of ladder-like rigid and contorted backbones[11]. The microporosity is termed intrinsic because it is solely generated from the molecular structure and is not dependent on the thermal or processing history of the materials. The surface areas of these polymers can maintain for a long period of time (>1 year) under ambient conditions and no significant change happens when they were heated to below their decomposition temperature (300 ℃ for 24 h)[4]. As long as the molecular structure of the polymers did not change, its intrinsic microporosity could be kept the same. PIMs have found wide applications in fields such as gas separation, gas storage and catalysis since reported, therefore the synthesis and application of PIMs has become a major research area in the past decade.

1.2 Classification of Polymer of Intrinsic Microporisty

1.2.1 Network PIM

Activated carbons are network polymers consisted of randomly arranged, inter-linked graphene sheets produced by carbonization of raw materials. The surface of activated carbons is usually chemically ill-defined with different sub-groups because of the complex nature of the source materials, which limit its applications for chemo-selective processes. Furthermore, it's difficult to control the pore size and pore shape of the activated carbon. Most of activated carbons possess a wide distribution of pore sizes ranging from microporous to mesoporous (2-50 nm) to macroporous (>50 nm)[4]. Therefore, it inspires the preparation of network polymers which combine the amorphous microporous structure and the well-defined surface chemistries.

Transient metal phthalocyanine-containing polymers are useful because of oxidative catalysis and microporous phthalocyanine network polymers was desired to be prepared. It is difficult to ensure the microporosity because of the strong non-covalent π-π interactions between the aromatic components[12]. Therefore, highly rigid and nonlinear linking groups are introduced to connect the phthalocyanine units to prevent aggregation and loss of microporosity. Commercially available 5,5′,6,6′-tetra-hydroxy-3, 3, 3′, 3′-tetramethyl-1, 1′-spirobisindane (monomer A1-Scheme 1.1) was selected as the linking group to ensure inefficient packing and give an amorphous microporous structure.

Except the phthalocyanine-based network polymer of intrinsic microporosity (Pc-Network-PIMs), other rigid structures, for example porphyrins were considered as a suitable unit[13] to make network PIMs. Rigid linking groups were introduced between Monomer A1 and B1 (Scheme 1.1) by the efficient dioxane-forming reaction to prepare porous network-PIMs. The dioxane formation reaction offers a general way to synthesis PIMs from appropriate rigid monomers (e.g. A1-A6) and aromatic monomers (e.g.B1-B6) as shown in Scheme 1.1 and Table 1.1.

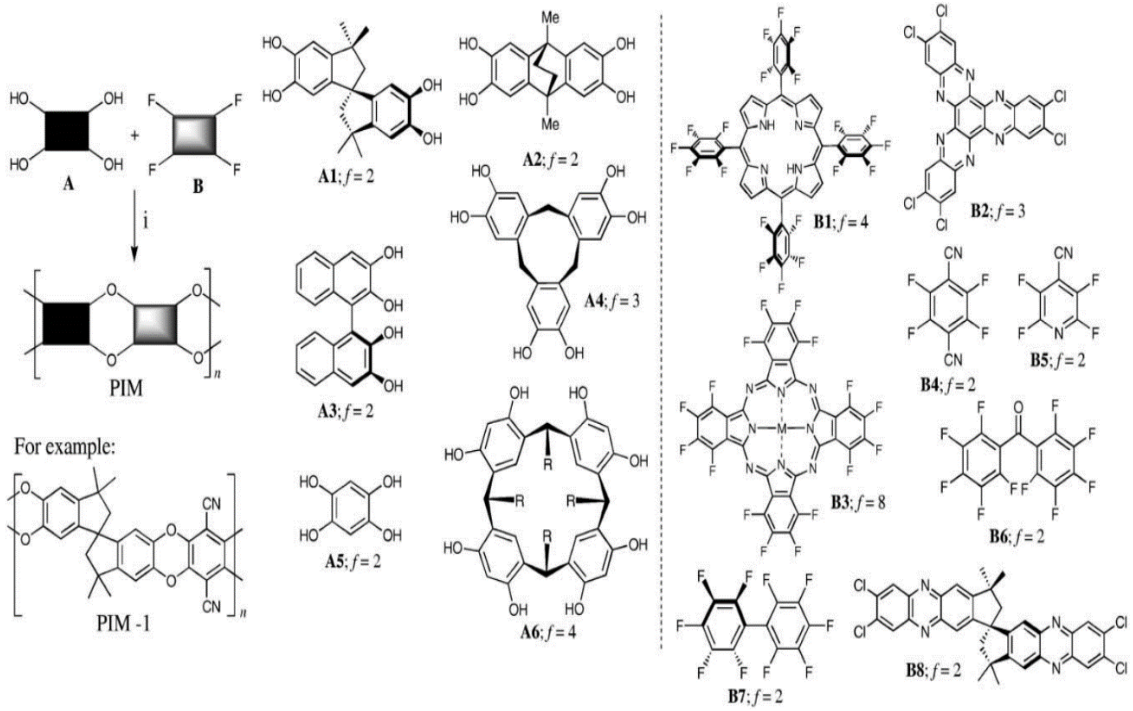

Scheme 1.1 Synthesis and properties of PIMs. *Reagents and conditions,* i. Monomer**A**, Monomer **B**, K_2CO_3, DMF[4]

Table1.1 Synthesis and properties of PIMs. *Reagents and conditions,* i.Monomer**A**, Monomer **B**, K_2CO_3, DMF[4]

Monomers		Insoluble network/Soluble polymer	Molecular mass M_w (g mole^{-1})	Surface area (BET; m^2 g^{-1})	Abbreviation	Analysed properties
A	**B**					
A1	**B1**	Network	—	1000	Por-network-PIM	Catalysis
A1	**B2**	Network	—	820	HATN-network-PIM	Catalysis; adsorption
A1	**B3**	Network	—	500	Mpc-network-PIM	Catalysis
A1	**B4**	Soluble	$>200 \times 10^3$	760	PIM-1	Membranes; H_2-adsorption
A1	**B5**	Soluble	$>100 \times 10^3$	750	—	—
A1	**B6**	Soluble	170×10^3	560	PIM-3	—
A1	**B7**	Soluble	36×10^3	600	PIM-2	—
A1	**B8**	Soluble	$>100 \times 10^3$	750	PIM-7	Membranes
A2	**B2**	Network	—	750	HATN-Network-PIM-2	Catalysis
A3	**B4**	Soluble	5×10^3	450	PIM-4	—
A4	**B4**	Network	—	830	CTC-network-PIM	H_2-adsorption
A5	**B7**	Soluble		550	PIM-6	—
A6	**B4**	Network	—	800	Calix-network-PIM	—
A6	**B4**	Insoluble	—	2	—	—

1.2.2 Non-network PIM

Non-network PIMs is usually linear and lack of cross-linking, so they could be soluble or forming gels in common organic solvents, which provides a significant advantages over network PIMs. The average molecular mass of the soluble PIMs are relatively low and has fewer repeating units, which is also helpful for dissolving in solutions. Therefore, the techniques for conventional polymers and one for microporous materials can be combined.

Robust, free standing membranes of high surface area can be prepared by simply casting from solution (Fig.1.1), which would greatly facilitate a range of potential applications such as gas separation[3,10]. The films are transparent, suggesting a wide band gap of the materials and therefore PIMs are electrically insulating. Generally, non-network polymers are not microporous, because of lack of robust network structure to maintain the microporosity. The backbones tend to bend and twist to maximise intermolecular interactions and to pack space efficiently[13]. However, some molecules are quite rigid, for instance possessing a chiral centre, they can have free volume themselves. When the free volume increased to some extent and is effectively interconnected, the polymer will probably have similar properties like network polymers in terms of microporosity.

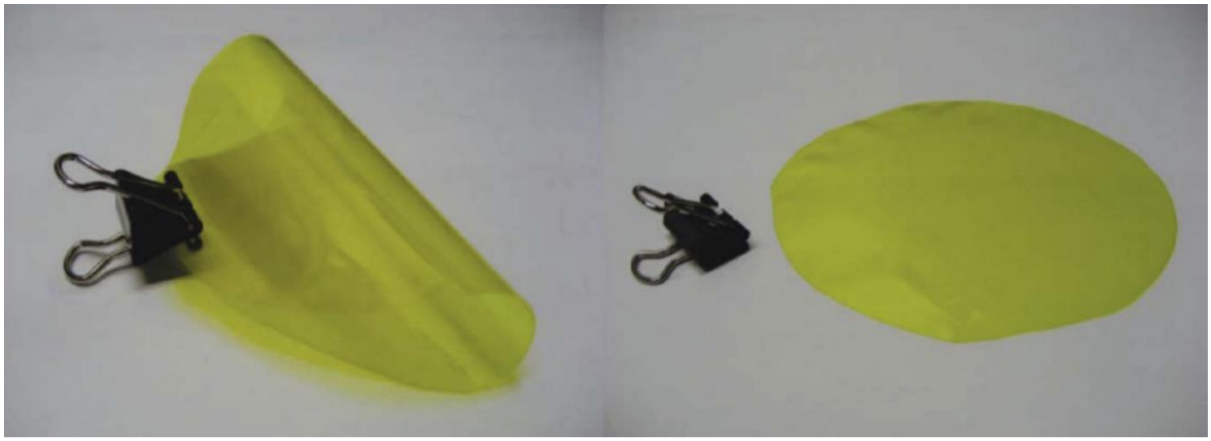

Figure. 1.1 Flexible and transparent PIM-1 film[14]

It was found that a 'site of contortion' (e.g. A1, A3, B7 or B8 in scheme 1), either a spiro-center, a single-covalent or a non-planar rigid skeleton is a necessary in at least one of the two precursor monomers to ensure a microporous resulting polymer. The first non-network soluble PIM was synthesised by Budd and Neil in 2003[3,10], which is termed PIM-1(Fig. 1.2b) later. Dibenzodioxane formation reaction was selected between the commercial available bis-catechol 5,5',6,6'-tetrahydroxy-3,3,3',3'-tetramethyl-1,1'-spirobisindane (A1) and 2,3,5,6-tetrafluroro-terephthalonitrile (B4) (Fig.1.2a), which has been successfully applied in network PIMs synthesis. A1 contains the spiro-center and provides the site of contortion to generate the microporosity. It has high molecular weight (M_w=140000 g mol^{-1}) and high surface area (600-900 m^2 g^{-1})[3]according to low-temperature N_2 adsorption-desorption analysis. PIM-1 can be casted to a yellow transparent free-standing film and exhibits strong fluorescence. Following PIM-1, PIM 2-6 were synthesised also by dibenzodioxane formation reaction. Except PIM-6, which is soluble only in acidic solvents (*e.g.* TFA), the polymers all have good solubility in

polar aprotic solvents (*e.g.* THF, DMAc).Another reported PIM with good properties is PIM-7[2](Fig.1.3, from monomers A1 and B8), which is suitable for gas separation because of its high permeability and maintaining selectivity.

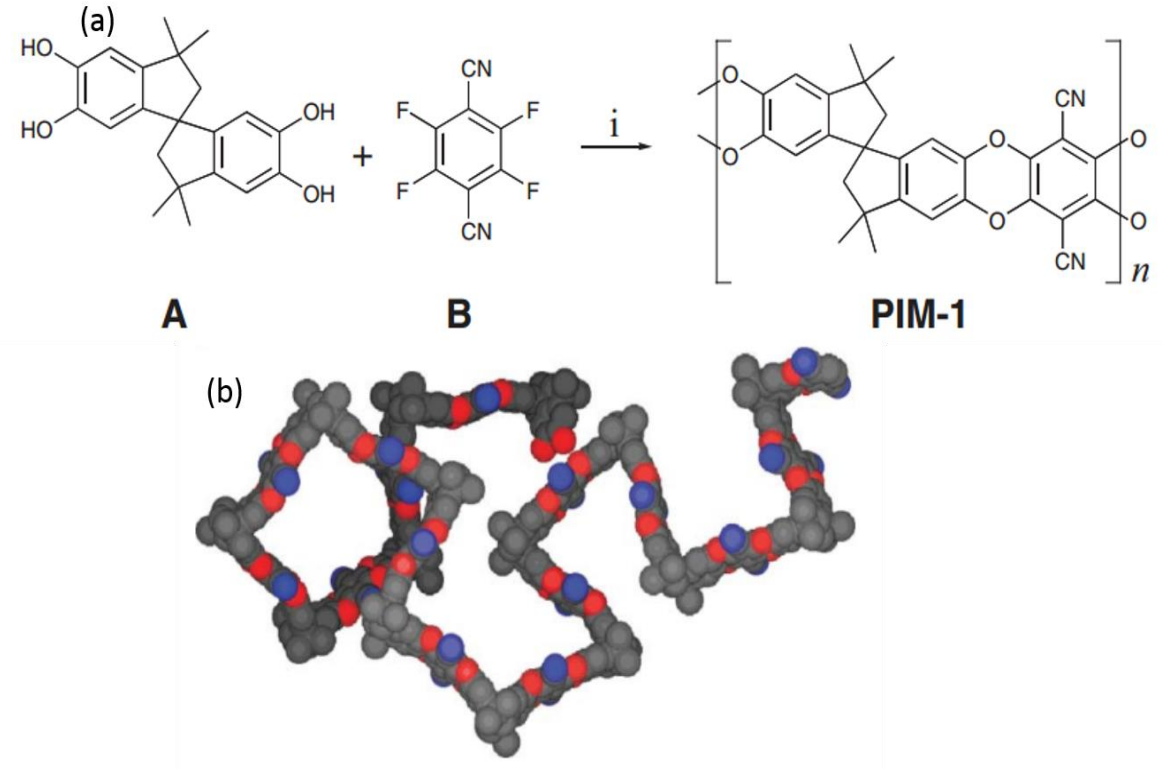

Figure. 1.2. (a) Synthesis of PIM-1,i) regents and conditions: K_2CO_3, DMF, 50-70℃ (b) A molecular model of PIM[4]

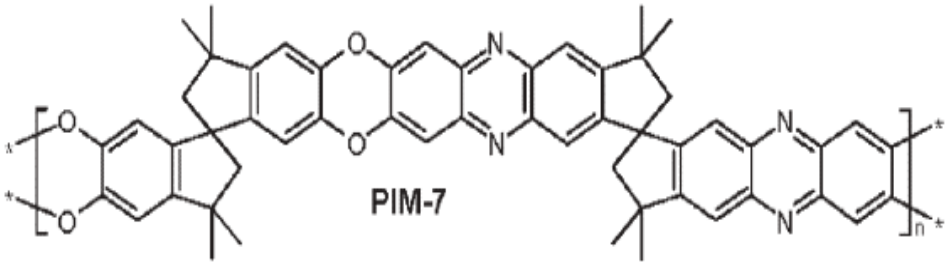

Figure 1.3. molecular structure of PIM-7[2]

The linear PIMs demonstrates that network is not a necessity to generate and maintain the microporosity within polymers. The molecular structure of these PIMs is quite rigid, just like a ladder, so the freedom along the polymers backbones is low to prevent efficient space packing and polymers will not collapse to non-porous solid.

1.2.3 Modification of PIMs

1.2.3.1 PIMs with substituted groups

There are two key factors that are generally required to ensure the intrinsic microporosity, one is the rigid ladder aromatic chain structure and the other is a contorted site to prevent free packing of the backbone. Up to now, there are only three common chemical reactions developed to prepare PIMs, dibenzodioxane-forming reaction, imidization and amidization[15]. Also, only several monomers are suitable to prepare the PIMs to make sure the porous structure. Therefore, the synthesis and investigation of PIMs are quite limited. In alternative to designing of new monomers and reactions, post-modification would be a good way to prepare structurally new PIM materials and lead to new properties[16]. One of the useful post-modification method is to introduce different substituted groups to PIMs.

Some work has been done to synthesise the functionalized PIMs, especially based on the nitrile groups on PIM-1, the most well-known and reported PIM-type material (Fig.1.2). PIM-1 can be modified to provide a polymer substituted with tetrazole group (TZ-PIM) and then further converted to a new PIM substituted with methyl tetrazole group (MTZ-PIM) (Fig.1.4). After modification, the TZ-PIM and MTZ-PIM have improved solubility in non-protic and protic solvents than PIM-1. Also, the new PIMs after modification show higher gas selectivity although decrease in gas permeability[17,18]. There are several ways to modify PIM-1. For instance, carboxylated PIMs (Fig 1.5) membranes have been prepared by simply in situ hydrolysis of the nitrile groups of PIM-1 films[19,20].All carboxylated-PIM membranes possess good mechanical properties and thermal stabilities while showing evident decreases in gas permeability and obvious increases in gas pair selectivity. These work demonstrate that it is a good way to change properties significantly by post modification of PIMs. It expands the spectrum of PIM material and also helps to better understand the relationship between the molecular structures and pores[21,22].

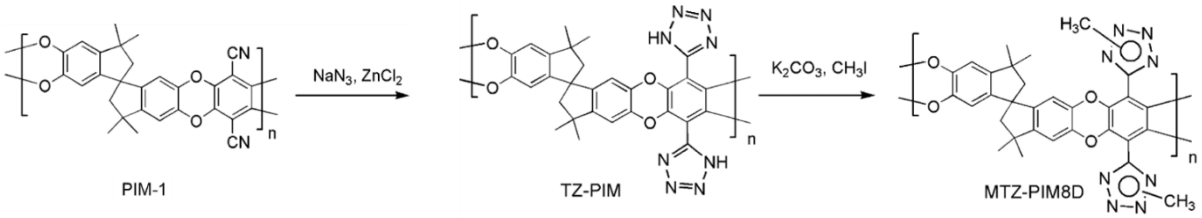

Figure 1.4. Reaction scheme for conversion from PIM-1 to MTZ-PIM8D[18]

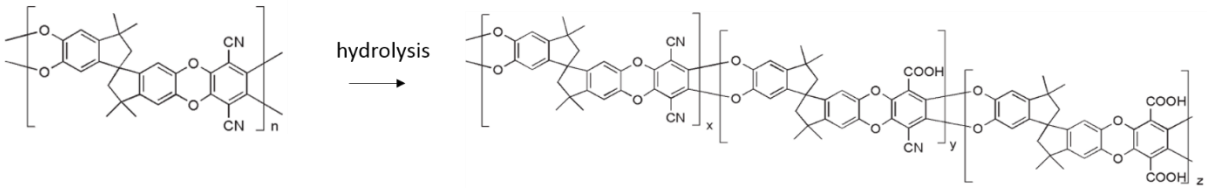

Figure 1.5. Reaction scheme for hydrolysis of PIM-1[19]

1.2.3.2 Cross-linked PIM

Cross-linking methods have been introduced into PIM membranes to improve the properties and generate new materials (Fig.1.6). First, A UV-cross-linking approach was proposed by the researchers[23] to tighten the backbone chains and reduce the internal spaces. PIM-1 were thermally cross-linked in the nitrile groups site, which leads to increase in porosity of polymers[24]. Another example of thermal cross-linking is after thermal decarboxylation of membranes derived from carboxylated PIMs (C-PIMs), the phenyl radicals can be cross-linked by thermal or radical reaction[25]. Cross-linking methods usually lead to higher structural stability.

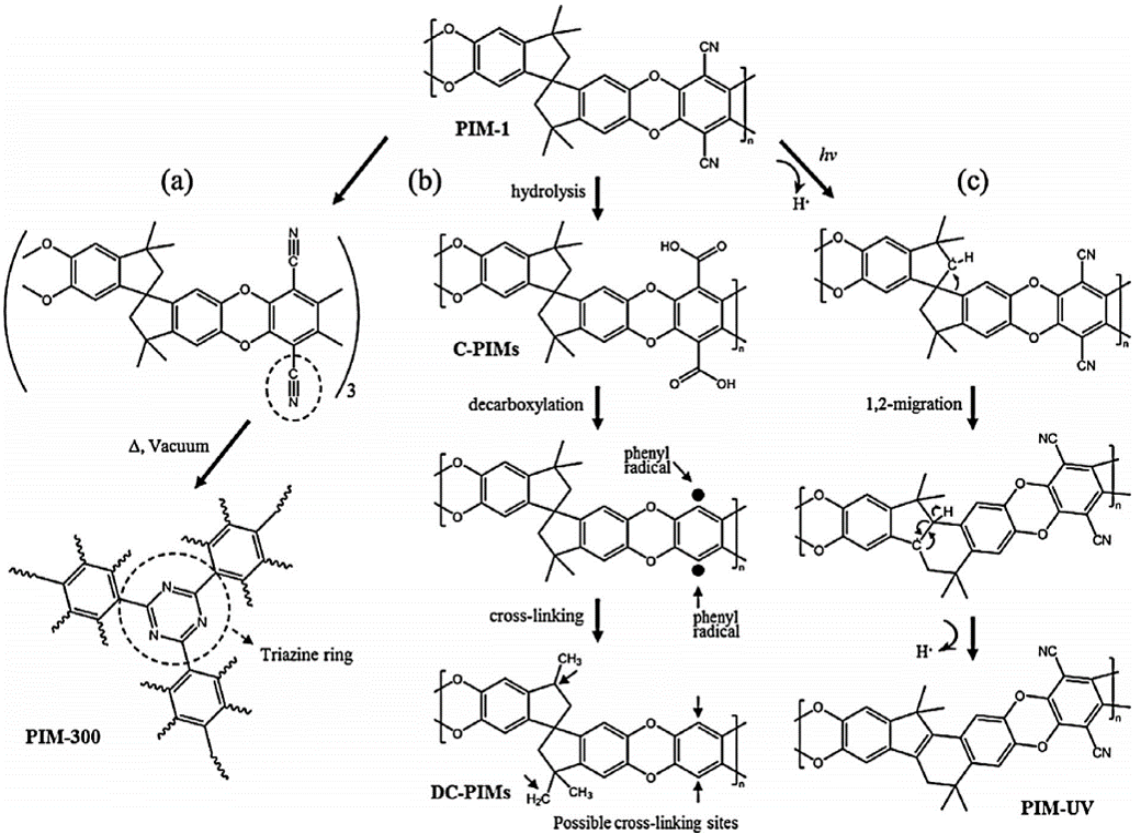

Figure 1.6. Cross-linked PIMs: (a) thermally self-cross-linked PIMs, (b) decarboxylation-induced cross-linked PIMs and (c) UV-rearranged PIMs[11]

1.2.3.3 Other modification methods

Several other modification methods have been developed to improve the properties of PIMs. A series of microporous polyimides are prepared, which are called PIM-PIs[18,26]. They combines the microporisity of PIMs and advanced physical properties of polyimides and demonstrated outstanding stability, solubility as well as permeability compared with conventional polyimide. In addition, PIMs can be mixed with other organic and inorganic materials to form polymer blend, such as zoolites, silica nanoparticles and so on[27]. For example, PIM-1 was selected to blend with commercially available Matrimid and demonstrate good thermal stability[28]. Different parameters including ratio of two compounds were investigated and compared for properties[29]. After that, further cross-linking were introduced to the PIM-1 blend membranes to improve the properties.

1.3 Applications of Polymers of Intrinsic Microporisity

1.3.1 Gas Permeation and Separation

Gas permeation and separation have long been an important research field because of the increasing commercial potential in which developing better materials are important. A variety of polymers have been prepared as gas separation membranes, but only a few succeeded in commercial application. Except the mechanical strength, a membrane material should have good permeability as well as good selectivity to separate different gases. However, the selectivity and permeability is a trade-off behaviour and can be demonstrated by a double logarithmic plot. Usually, polymers that have high permeability will possess relatively low selectivity. Robeson came up with the idea of upper bound[30,31] in the plot to quantify this trade-off empirically. Materials lie near to or exceed the upper bound line usually possess better performance for the gas separation. PIMs were investigated for the gas separation and show high gas permeation due to the high surface area. In addition, PIM-1 and PIM-7 for example[3]show better selectivity than other polymers of similar permeability and significantly exceed Robeson's upper bound plot for several commercially important gas pairs including O_2/N_2 and CO_2/CH_4 and H_2/N_2.

The polymers above the upper bound usually have twisted backbones to frustrate efficient packing. In contrast, rubbery polymers with flexible backbones usually lie well below upper

bound. A theory has been developed by Freedom[32] that a stiff backbone to interfere rotation freedom is an important design principle for polymers to achieve good gas separation properties. PIMs were prepared strictly following this principle, hence PIMs are better than hundreds of polymers in terms of gas permeation and separation.

1.3.2 Adsorption of Organics and Sensing

It is unsurprising that PIMs is suitable in organics adsorption because of their high accessible surface area. The 5,6,11,12,17,18-hexaazatrinapthylene (Hatn) based network PIM and PcCo-network-PIM[4] were synthesised and demonstrated to effectively adsorb phenol from aqueous solution[33]. Also, it can be used to remove the low concentration of phenol from water. The performance of these PIMs are comparable with activated carbons. In addition, PIMs could not adsorb dyes in big size from aqueous solution, which indicates the interesting size-selectivity effects of PIMs due to their narrow pore size distribution.

The removal of organics from water can also be achieved by PIM-1 and PIM-7 membranes by pervaporation. For instance, the phenol permeate through the PIM membrane as a vapour and then was condensed and collected. PIM-1 membrane is strongly organophilic and can accumulate phenol up to tenfold in the permeate[10].

A range of polymers have been investigated to detect the organic vapours in sensor construction to ensure proper safety. Sensors with PIM-1 layer can respond at low concentration, down to ppm levels to a wide variety of organic vapours. This can be attributed to the large surface area caused by microporosity, strong organophilic property and also the changes in the physic thickness of PIM-1 membrane swelling in organic solutions[34]. Based on this observation, Peter Budd, Neil Mckeown together with 3M company invented a visual indicator using PIM-1 film to help determine the time needed to change an organic vapour filter, which has become a commercial product now. When the amount of vapours collected by PIM exceeds a specified minimum indication level, the colour will change, indicating the end of service life for organic filters.

1.3.3 Heterogeneous Catalysis

The transient metal centre containing Network-PIMs have already been investigated for heterogeneous catalysis. Compared to a non-porous low molecular weight cobalt phthalocyanine, Cobalt-containing phthalocyanine PIM has been demonstrated to increase the rate of hydrogen peroxide degradation greatly[13].

In addition, certain ligands in the PIMs are capable of coordinating with metal ions to form a complex. For example, by exposing to a palladium solution, HATN-based network PIM will form a highly coloured material with a high loading of palladium. The intrinsic microporosity are retained after coordination. This material are able to catalyse the Suzuki coupling reaction effectively and more stable compared to the standard homogeneous $Pd(Ph_3)_4$ catalysts[4]. These metal ion coordination could be useful to catalysis and inspire the attempt to fabricate reactive membranes.

1.3.4 H_2 Storage

Hydrogen is a clean energy source with high chemical energy density (three times that of petrol), which provides an ideal alternative to replace the traditional fossil fuels[35]. However, the widespread use of hydrogen is frustrated by the lack of a safe and efficient storage method[35]. Besides compressing hydrogen, an attractive possibility is physisorption on the internal surface of microporous materials under moderate pressure (< 70 bar)[36,37]. Up to now, a variety of porous materials, such as carbon nanotubes and MOFs, have been investigated to this application and showed indeed promising hydrogen storage capacities[38]. However, it needs to be mentioned that there is still no material that are able to meet the requirement for a practical H_2 storage system nowadays.

Hence, it is an urgent and important task to design the materials with better hydrogen storage properties. High surface area microporous polymers have gained more and more attention as hydrogen sorption materials because they are only composed of relatively light elements (e.g., C, H, N, O)[39]. A range of PIMs were studied for the adsorption of H_2 using two different techniques, volumetric measurements and gravimetric measurements[40,41].It shows that the two methods have good agreement and H_2 sorption measurements were reversible. Several PIMs

showed a significant quantities of H_2 adsorption at relatively low pressures and reach the plateau at less than 10 bar pressure. Among these investigated PIMs, the triptycene-based polymer (Trip-PIM) performed the best for H_2 adsorption (1.6% , by mass at 1 bar and 2.7% at 10 bar)[42].These data are comparable with the best example of zeolites[43] and MOF[44]. Also, it is demonstrated that the small micropores (ultramicropores) dominate the H_2 adsorption[45]. Based on preliminary results, only when a PIM pocessing a surface area larger than 2500 m^2 g^{-1} with an ultramicroporous structure is possible to obtain practical hydrogen storage. Therefore, much efforts need to be devoted to the development of the appropriate molecular components of PIMs.

There are many other valuable applications of the porous polymers, including supports for catalysts[46–49], precursors of nanostructured carbon materials[50–52], encapsulation agents for controlled drugs release[53,54], templates for synthesis [55–57] and so on. Therefore, PIMs can be investigated for the applications above. What I am interested in is the application of PIMs in electrochemistry. The PIMs have good potential in electrochemistry for several reasons. First, the miroporous structure provides the accessibility to the binding sites to immobilize various molecules, for example, catalysts, which may improve the performance of electrocatalysts. Moreover, compared with the corresponding nonporous materials, the highly porous property may facilitate the mass transport process to enhance the sensitivity in electroanalysis. Also, the fixed pores may provide some kind of selectivity due to different size, charge or something else, which may find applications in separation or electro-sensor fields. This leads to the emergence of a wide variety of chemically modified electrodes to combine the microporosity of the materials with the particular redox probe. More importantly, the soluble PIMs can be casted to membranes easily, which offers a good way to investigate the membrane properties in electrochemistry.

1.4 PIM-EA-TB

Recently, a novel polymer of intrinsic microporosity with high molecular mass (Mw>70000 g mol^{-1}), called PIM-EA-TB (Fig.1.7a) was first reported by the group of Prof. Neil Mckeown in 2003[58]. It was synthesized by the polymerization of 2, 6(7)-diamino-9, 10-dimethyl-ethanoanthracene (EA) with dimethoxymethane in TFA, involving the formation of Tröger's base (TB) (Fig.1.7b). Compared with the spiro-centers and dioxane rings commonly used in

PIMs, the structure of EA is highly inflexible and also Tröger's base (TB) is rigid with the bridged bicyclic rings. Therefore, PIM-EA-TB is a highly shape-persistent ladder polymer with an apparent BET surface area of 1028 $m^2 g^{-1}$. It needs to be mentioned that the apparent surface area for PIM-EA-TB is greater than previously reported PIMs and other solution-processable, amorphous microporous materials[59,60]. Also, it is soluble in chloroform and can be casted into optically transparent films with good mechanical strength (Fig.1.7c). Due to its enhanced microporosity, PIM-EA-TB films showed particularly high gas permeabilities and also good selectivities for gas molecules. Therefore, it has huge potential for making large-scale gas separation membranes of commercial and environmental relevance.

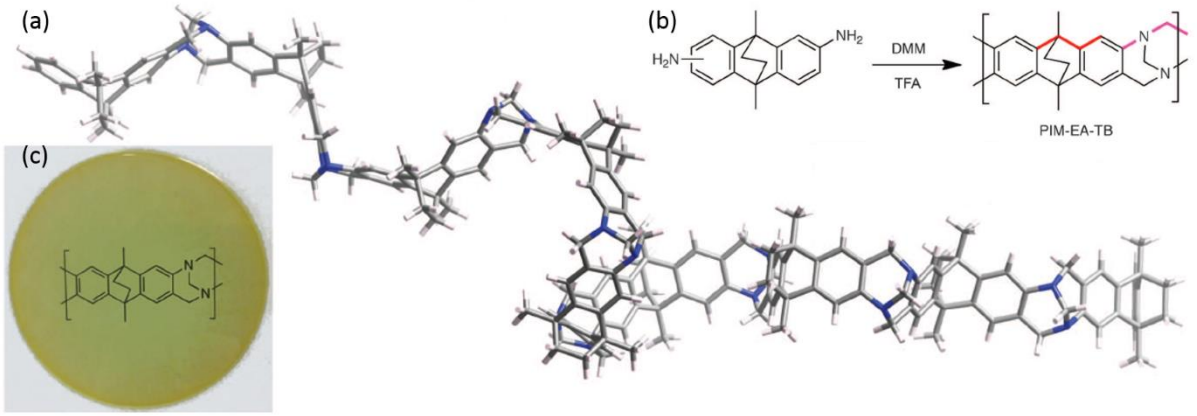

Figure.1.7. (a) A molecular model of PIM-EA-TB showing its contorted shape, which combined with its rigidity generates intrinsic microporosity due to an inability to pack efficiently in the solid state. (b) The synthesis and molecular structures of PIM-EA-TB. (c) A solvent-cast film (10 cm in diameter) of PIM-EA-TB, through which is visible its molecular structure printed on a piece of paper[58]

Due to its exceptional behaviour, deeper study has been performed to gain more fundamental understanding of its properties. The free volume probing experiments showed a relative large free volume and more importantly, there's little change of the size of free volume but more exchange between different connected environments during transport[61]. In addition, several computational models were established to reveal more information about size distribution and also the connectivity of the free volume. By comparing with other PIMs like PIM-1, the unique feature of PIM-EA-TB is the presence of intermediate-sized voids and fewer extremely large interconnected voids. This means the molecules has to make more "jumps" from one free volume to another when transported in PIM-EA-TB, which increased the size selectivity. Another interesting property of PIMs is that alcohol treatment will increase their permeabilities,

especially for PIM-EA-TB. After soaking in alcohol, the permeability increased significantly by 5-12 fold for PIM-EA-TB while by 3-fold for PIM-1, indicating the increase of free volume[61].

PIM-EA-TB has become the subject of detailed studies in various fields in addition to gas permeation and separation. Based on this PIM material, some creative work has been done by Fengjie Xia[62]. In his work, two polymers (i) PIM-EA-TB and (ii) a traditional structurally less rigid polymer are compared to highlight the benefits of the newly emerging PIM membrane materials in electrocatalysis and nanostructure formation. It is demonstrated that polymer membrane with intrinsic microporosity has a much higher number of active binding sites and binding ability/capacity of redox active anions such as indigo carmine and $PdCl_4^{2-}$. Interesting nano-lamella growth for Pd metal during electro-reduction of $PdCl_4^{2-}$ is observed within pores of PIM and show a promising catalytic activity of formic acid used in fuel cells.

PIMs open up a range of new opportunities for selective transport of reagents and improved stability in nano-catalyst systems and appears huge potential in electrocatalysis and electroanalysis. More progress has developed from this work, including hosting of the catalysts[63–65], improving catalyst stability[66,67], acting as ionic diode[68,69] and so on. In this thesis, more work will be developed for the application of PIM-EA-TB in electrochemistry.

1.5 References

1 N. B. McKeown and P. M. Budd, *Macromolecules*, 2010, **43**, 5163–5176.

2 B. S. Ghanem, N. B. McKeown, peter M. Budd and D. Fritsch, *Macromolecules*, 2008, **41**, 1640–1646.

3 P. M. Budd, B. S. Ghanem, S. Makhseed, N. B. McKeown, K. J. Msayib and C. E. Tattershall, *Chem. Commun.*, 2004, 230–231.

4 N. B. McKeown and P. M. Budd, *Chem. Soc. Rev.*, 2006, **35**, 675–683.

5 G. Férey, *Chem. Soc. Rev.*, 2008, **37**, 191–214.

6 M. Eddaoudi, D. B. Moler, H. Li, B. Chen, T. M. Reineke, M. O'Keeffe and O. M. Yaghi, *Acc. Chem. Res.*, 2001, **34**, 319–330.

7 M. Eddaoudi, J. Kim, N. Rosi, D. Vodak, J. Wachter, M. O'Keeffe and O. M. Yaghi, *Science*, 2002, **295**, 469–472.

8 G. V Knighten, a Weber, R. D. Turner, R. W. Smith, Y. R. Shen, R. Fitzgibbon, B. Lax, C. L. Evans, X. S. Xie, N. Dudovich, D. Yelin, Y. Silberberg, N. Dudovich, D. Yelin, Y. Silberberg, a G. Caster, S. R. Leone, H. Zhao, M. T. Cicerone, K. a Marko, L. Rimai, C. Otto, J. Greve, H. Hamaguchi, V. V Yakovlev, M. Bonn, M. Muller, W.

Holzapfel, W. Zinth, W. Kaiser, T. Lang, M. Motzkus, S. Roy, T. R. Meyer, J. R. Gord, R. Dasari, M. Feld, J. F. Sperry, J. Reintjes, T. J. Manuccia, G. R. Holton, X. S. Xie, S. Chen and D. D. Dlott, 2007, 268–273.

9 A. P. Cote, A. I. Benin, N. W. Ockwig, M. O'Keeffe, A. J. Matzger and O. M. Yaghi, *Science (80-.).*, 2005, **310**, 1166–1170.

10 P. M. Budd, E. S. Elabas, B. S. Ghanem, S. Makhseed, N. B. McKeown, K. J. Msayib, C. E. Tattershall and D. Wang, *Adv. Mater.*, 2004, **16**, 456–459.

11 S. Kim and Y. M. Lee, *Prog. Polym. Sci.*, 2015, **43**, 1–32.

12 N. B. McKeown, *J. Mater. Chem.*, 2000, **10**, 1979–1995.

13 P. M. Budd, N. B. McKeown and D. Fritsch, *J. Mater. Chem.*, 2005, **15**, 1977–1986.

14 J. Song, N. Du, Y. Dai, G. P. Robertson, M. D. Guiver, S. Thomas and I. Pinnau, *Macromolecules*, 2008, **41**, 7411–7417.

15 D. Wu, F. Xu, B. Sun, R. Fu, H. He and K. Matyjaszewski, *Chem. Rev. (Washington, DC, United States)*, 2012, **112**, 3959–4015.

16 R. Dawson, A. I. Cooper and D. J. Adams, *Prog. Polym. Sci.*, 2012, **37**, 530–563.

17 N. Du, H. B. Park, G. P. Robertson, M. M. Dal-Cin, T. Visser, L. Scoles and M. D. Guiver, *Nat. Mater.*, 2011, **10**, 372–375.

18 N. Du, G. P. Robertson, M. M. Dal-Cin, L. Scoles and M. D. Guiver, *Polym. (United Kingdom)*, 2012, **53**, 4367–4372.

19 J. Weber, N. Du and M. D. Guiver, *Macromolecules*, 2011, **44**, 1763–1767.

20 N. Du, G. P. Robertson, J. Song, I. Pinnau and M. D. Guiver, *Macromolecules*, 2009, **42**, 6038–6043.

21 N. Du, G. P. Robertson, J. Song, I. Pinnau, S. Thomas and M. D. Guiver, *Macromolecules*, 2008, **41**, 9656–9662.

22 C. R. Mason, L. Maynard-Atem, N. M. Al-Harbi, P. M. Budd, P. Bernardo, F. Bazzarelli, G. Clarizia and J. C. Jansen, *Macromolecules*, 2011, **44**, 6471–6479.

23 D. a Lesch, H. Estates and A. E. Shumate, *US Pat.*, 2010, **7758**, 751.

24 F. Y. Li, Y. Xiao, T. S. Chung and S. Kawi, *Macromolecules*, 2012, **45**, 1427–1437.

25 N. Du, M. M. Dal-Cin, G. P. Robertson and M. D. Guiver, *Macromolecules*, 2012, **45**, 5134–5139.

26 B. S. Ghanem, N. B. McKeown, P. M. Budd, N. M. Al-Harbi, D. Fritsch, K. Heinrich, L. Starannikova, A. Tokarev and Y. Yampolskii, *Macromolecules*, 2009, **42**, 7881–7888.

27 J. Ahn, W. J. Chung, I. Pinnau, J. Song, N. Du, G. P. Robertson and M. D. Guiver, *J. Memb. Sci.*, 2010, **346**, 280–287.

28 W. F. Yong, F. Y. Li, Y. C. Xiao, T. S. Chung and Y. W. Tong, *J. Memb. Sci.*, 2013, **443**, 156–169.

29 W. F. Yong, F. Y. Li, T.-S. Chung and Y. W. Tong, *J. Mater. Chem. A*, 2013, **1**, 13914–13925.

30 L. M. Robeson, *J. Memb. Sci.*, 2008, **320**, 390–400.

31 L. M. Robeson, *J. Memb. Sci.*, 1991, **62**, 165–185.

32 B. D. Freeman, *Macromolecules*, 1999, **32**, 375–380.

33 P. M. Budd, B. Ghanem, K. Msayib, N. B. McKeown and C. Tattershall, *J. Mater. Chem.*, 2003, **13**, 2721.

34 J. Christopher Thomas, J. E. Trend, N. a. Rakow, M. S. Wendland, R. J. Poirier and D. M. Paolucci, *Sensors*, 2011, **11**, 3267–3280.

35 L. Schlapbach and a Züttel, *Nature*, 2001, **414**, 353–358.

36 A. W. C. van den Berg and C. O. Areán, *Chem. Commun.*, 2008, 668–681.

37 A. M. Seayad and D. M. Antonell, *Adv. Mater.*, 2004, **16**, 765–777.

38 H. K. Chae, Y. D. Siberio-Perez, J. Kim, Y. Go, M. Eddaoudi, A. J. Matzger, M. O'Keeffe and O. M. Yaghi, *Nature*, 2004, **427**, 523–527.

39 A. Thomas, P. Kuhn, J. Weber, M. M. Titirici and M. Antonietti, *Macromol. Rapid Commun.*, 2009, **30**, 221–236.

40 N. B. McKeown, P. M. Budd and D. Book, *Macromol. Rapid Commun.*, 2007, **28**, 995–1002.

41 P. M. Budd, A. Butler, J. Selbie, K. Mahmood, N. B. McKeown, B. Ghanem, K. Msayib, D. Book and A. Walton, *Phys. Chem. Chem. Phys.*, 2007, **9**, 1802–1808.

42 B. S. Ghanem, K. J. Msayib, N. B. McKeown, K. D. M. Harris, Z. Pan, P. M. Budd, A. Butler, J. Selbie, D. Book and A. Walton, *Chem. Commun.*, 2007, **1**, 67–69.

43 A. Zecchina, S. Bordiga, J. G. Vitillo, G. Ricchiardi, C. Lamberti, G. Spoto, M. Bjorgen and K. P. Lillerud, *J. Am. Chem. Soc.*, 2005, **127**, 6361–6366.

44 J. L. C. Rowsell, A. R. Millward, K. S. Park and O. M. Yaghi, *J. Am. Chem. Soc.*, 2004, **126**, 5666–5667.

45 J.-Y. Lee, C. D. Wood, D. Bradshaw, M. J. Rosseinsky and A. I. Cooper, *Chem. Commun.*, 2006, 2670–2672.

46 S. J. Pierre, J. C. Thies, A. Dureault, N. R. Cameron, J. C. M. Van Hest, N. Carette, T. Michon and R. Weberskirch, *Adv. Mater.*, 2006, **18**, 1822–1826.

47 C. Féral-Martin, M. Birot, H. Deleuze, A. Desforges and R. Backov, *React. Funct. Polym.*, 2007, **67**, 1072–1082.

48 C. E. Chan-Thaw, A. Villa, P. Katekomol, D. Su, A. Thomas and L. Prati, *Nano Lett.*, 2010, **10**, 537–541.

49 Y. Zhang, L. Zhao, P. K. Patra and J. Y. Ying, *Adv. Synth. Catal.*, 2008, **350**, 662–666.

50 D. Wu, R. Fu, M. S. Dresselhaus and G. Dresselhaus, *Carbon N. Y.*, 2006, **44**, 675–681.

51 Q. Zeng, D. Wu, C. Zou, F. Xu, R. Fu, Z. Li, Y. Liang and D. Su, *Chem. Commun.*, 2010, **46**, 5927–5929.

52 Y. Wang, J. Liu, S. Christiansen, D. H. Kim, U. Gösele and M. Steinhart, *Nano Lett.*, 2008, **8**, 3993–3997.

53 M. R. Abidian, D. H. Kim and D. C. Martin, *Adv. Mater.*, 2006, **18**, 405–409.

54 Z. Shi, Y. Zhou and D. Yan, *Macromol. Rapid Commun.*, 2006, **27**, 1265–1270.

55 K.-H. Lo, W.-H. Tseng and R.-M. Ho, *Macromolecules*, 2007, **40**, 2621–2624.

56 W. H. Tseng, C. K. Chen, Y. W. Chiang, R. M. Ho, S. Akasaka and H. Hasegawa, *J.*

Am. Chem. Soc., 2009, **131**, 1356–1357.

57 Y. Wang, C. He, W. Xing, F. Li, L. Tong, Z. Chen, X. Liao and M. Steinhart, *Adv. Mater.*, 2010, **22**, 2068–2072.

58 M. Carta, R. Malpass-Evans, M. Croad, Y. Rogan, J. C. Jansen, P. Bernardo, F. Bazzarelli and N. B. McKewon, *Science (80-.).*, 2013, **339**, 303–307.

59 S. Jiang, J. T. a Jones, T. Hasell, C. E. Blythe, D. J. Adams, A. Trewin and A. I. Cooper, *Nat. Commun.*, 2011, **2**, 207.

60 M. W. Schneider, I. M. Oppel, H. Ott, L. G. Lechner, H. J. S. Hauswald, R. Stoll and M. Mastalerz, *Chemistry (Easton).*, 2012, **18**, 836–847.

61 E. Tocci, L. De Lorenzo, P. Bernardo, G. Clarizia, F. Bazzarelli, N. B. Mckeown, M. Carta, R. Malpass-evans, K. Friess, M. Lanc, Y. P. Yampolskii, L. Strarannikova, V. Shantarovich, M. Mauri and J. C. Jansen, *Macromolecules*, 2014, 7900–7916.

62 F. Xia, M. Pan, S. Mu, R. Malpass-Evans, M. Carta, N. B. McKeown, G. A. Attard, A. Brew, D. J. Morgan and F. Marken, *Electrochim. Acta*, 2014, **128**, 3–9.

63 H. Al Kutubi, L. Rassaei, W. Olthuis, G. W. Nelson, J. S. Foord, P. Holdway, M. Carta, R. Malpass-Evans, N. B. McKeown, S. C. Tsang, R. Castaing, T. R. Forder, M. D. Jones, D. He and F. Marken, *RSC Adv.*, 2015, **5**, 73323–73326.

64 S. D. Ahn, A. Kolodziej, R. Malpass-Evans, M. Carta, N. B. McKeown, S. D. Bull, A. Buchard and F. Marken, *Electrocatalysis*, 2016, **7**, 70–78.

65 A. Kolodziej, S. D. Ahn, M. Carta, R. Malpass-Evans, N. B. McKeown, R. S. L. Chapman, S. D. Bull and F. Marken, *Electrochim. Acta*, 2015, **160**, 195–201.

66 D. He, Y. Rong, M. Carta, R. Malpass-Evans, N. B. McKeown and F. Marken, *RSC Adv.*, 2016, **6**, 9315–9319.

67 D. He, Y. Rong, Z. Kou, S. Mu, T. Peng, R. Malpass-Evans, M. Carta, N. B. McKeown and F. Marken, *Electrochem. commun.*, 2015, **59**, 72–76.

68 E. Madrid, P. Cottis, Y. Rong, A. T. Rogers, J. M. Stone, R. Malpass-Evans, M. Carta, N. B. McKeown and F. Marken, *J. Mater. Chem. A*, 2015, **3**, 15849–15853.

69 E. Madrid, Y. Rong, M. Carta, N. B. McKeown, R. Malpass-Evans, G. A. Attard, T. J. Clarke, S. H. Taylor, Y. T. Long and F. Marken, *Angew. Chemie*, 2014, **53**, 10751–10754.

Chapter 2: Introduction to Electrochemical Techniques

Chapter Abstract

Electrochemistry can be seen a branch of physical chemistry, which studies the chemical reactions, usually oxidation and reduction, driven by an applied electrical potential. In order to understand the underlying processes and mechanisms of the reactions well, basic theories were established and a number of measurement methods were developed. This Chapter presents some of the fundamental insights of electrochemistry, including the thermodynamics of electrochemical reactions, electrode kinetics and mass transport. Some important electrochemical techniques are also introduced, such as cyclic voltammetry, potential step voltammetry, rotating disk electrode, electrochemical impedance spectroscopy and the development of two, three and four electrodes systems.

2.1 Introduction

Electrochemistry deals with chemical reactions which take place at the surface between a conducting electrode and the electrolyte solution. Similar to the case for all chemical reactions, the thermodynamic and kinetic information provide two important aspects in the understanding of the electrochemical reactions. Thermodynamics determines the direction of the reaction and also to what extent the reaction will proceed, while kinetics determines at what rate the reaction happens. In electrochemistry, the magnitude of current often represents the rate of the reaction. Many parameters will influence the electrochemical reaction, including the reactivity of the species, the nature of the electrode, the electrode potential, the solution composition and the mass transport.

Various electrochemical techniques are used to provide the detailed information of the electrochemical reactions. The most previous and simplest cell set-up is two electrodes system, i.e. working electrode (W.E) and reference electrode (R.E). Because a current flows in the solution between two electrodes, there is a voltage drop, iR and the applied potential E is not confined to the driving force. In addition, the passage of large current through the reference electrode change the potential of the electrode. Therefore, the two electrodes system is suitable for the microelectrode experiments in which the current is very small and the voltage drop could neglected. In order to solve this problem, a third electrode, counter electrode (C.E) was introduced to form the three electrodes system (Figure 2.1). They are connected to a potentiostat to control the potential difference between the reference and working electrode with minimal interference from IR drop. The current only flows between the working and counter electrode. Three electrodes system is commonly used in the electrochemical experiments.

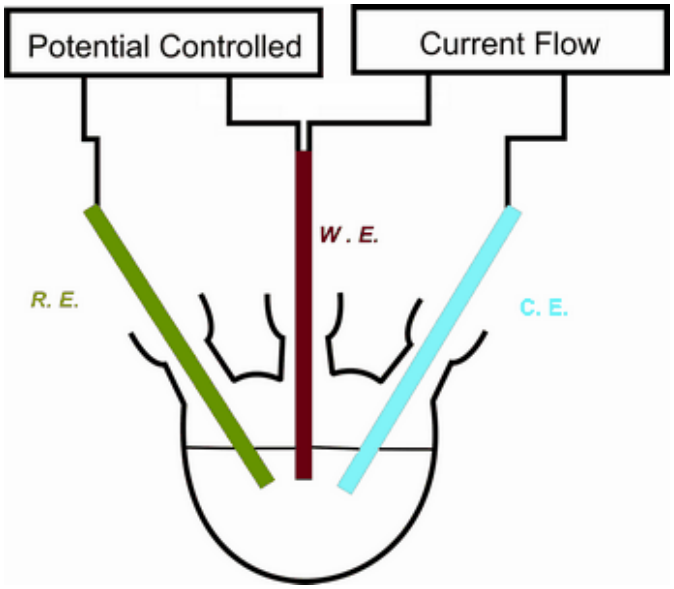

Figure 2.1. Schematic drawing of a three-electrode electrochemical cell

The four-electrode setup (Fig. 2.2) is not as common as three-electrode system while has its own place in electrochemical measurements. It is usually used to measure the interfaces, such as two nonmiscible liquid-liquid junctions[1] or membranes. Thus, it can measure the solution resistance or the resistance across the surface of some material accurately. This set-up have also been used in electrophoresis and coulometric titration[2].

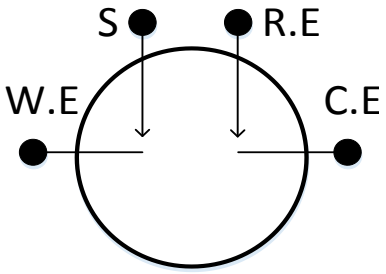

Figure 2.2. Schematic drawing of 4 electrode setup

In three electrodes mode, the working electrode (WE) is where the interested reactions occurred, the reference electrode (RE) has a stable potential and is used for the potential reference point and the counter electrode (CE) is to complete the current circuit. The sensor electrode (S) is decoupled from the working electrode to give the four electrode systems. Therefore, the potential is measured between the RE and the S and the current is flowed between the WE and CE. Compared with the high internal resistance, the electrode resistance can be ignored, the potential difference between the RE and the S is equal to the potential difference between the

corresponding points of the solution. In a membrane system, the potential is equal to the transmembrane potential if the electrodes are located close to the membrane and the solution conductivity is high[3]. Thus, the reactions occurring in the electrodes are not being measured. Instead, the change of the solution itself across the interface are measured in the four-electrode system.

2.2 Dynamic Electrochemistry

2.2.1 Thermodynamics of Electrochemical Reactions

The thermodynamic data for electrochemistry can be obtained in an equilibrium state between a metallic electrode (m) and a solution phase (aq). When a suitable electrode is inserted into the solution containing both oxidized and reduced species, the equilibrium condition will be achieved soon with fast rates of electron transfer.

A general electron transfer process can be illustrated by equation 2.1.

$$O_{(aq)} + ne^-_{(m)} \leftrightarrow R_{(aq)} \qquad (2.1)$$

Here the oxidised species O can be reduced to the species R at the electrode surface or vice versa. Once the equilibrium is established at the surface of the electrode, the rates of oxidation and reduction are exactly the same and there is no net current in the system. Different from the chemical equilibrium, there is transfer of charged species and electrons involved in electrochemistry. As a result, there is a net electrical charge on the two phases, metal and solution coupling to the potential. Either the reaction lies to left side or right side, charge separation arises when the reaction moves towards equilibrium. The potential difference between two phases ($\emptyset_m - \emptyset_s$) is called electrode potential. It has a fixed and precise value for any particular system and can be measured by the introduction of the reference electrode. If no current is flowing through the system, the equilibrium potential E_e is dependent on the relative concentrations of the species O and R. A standard reference electrode, the standard hydrogen electrode (SHE), is defined to have an absolute potential of zero (the pressure of hydrogen gas is 1 bar (100 kPa) and the activity of hydrogen ions in the solution is unity). Under that condition, the equilibrium potential of the electrode can be calculated by the Nernst equation 2.2[4,5].

$$E_e = E^\circ + \frac{RT}{nF}\ln(\frac{a_O}{a_R}) \quad (2.2)$$

Here E^o is the standard electrode potential, n is the number of electron transferred and a_O is the activity of oxidised species and a_R is the activity of reduced species. The activity of a species dissolved in a solution is proportional to its concentration (equation 2.3). Hence, the Nernst equation can be expressed in terms of concentration (equation 2.4).

$$a_A = \gamma_A[A] \quad (2.3)$$

$$E_e = E^{\circ\prime} + \frac{RT}{nF}\ln(\frac{[O]}{[R]}) \quad (2.4)$$

with $E^{\circ\prime} = E^\circ + \frac{RT}{nF}\ln(\frac{\gamma_O}{\gamma_R})$

Here, γ is the activity coefficient, $E^{\circ\prime}$ is termed formal potential and [O]/[R]is the concentration of oxidised and reduced species at the electrode surface respectively, which are the same as in the bulk solution under equilibrium conditions.

The inherent reason behind the electron transfer is the relative energy level between the species. The electrons tend to leave the higher energy level to the lower ones. Therefore, if the Fermi level in the metal is higher than the lowest unoccupied molecular orbital (LUMO) of the species, the electron will be transferred from the electrode to the species in solution, resulting the reduction of the species (Fig. 2.3(a)). On the contrary, the electron will be transferred to the electrode if the highest occupied molecular orbital (HOMO) is higher in energy than the Fermi level, which is the way oxidation occurs (Fig. 2.3(b)). The electron transfer will change the energy level of the metal and the solution until the equilibrium is reached[4].

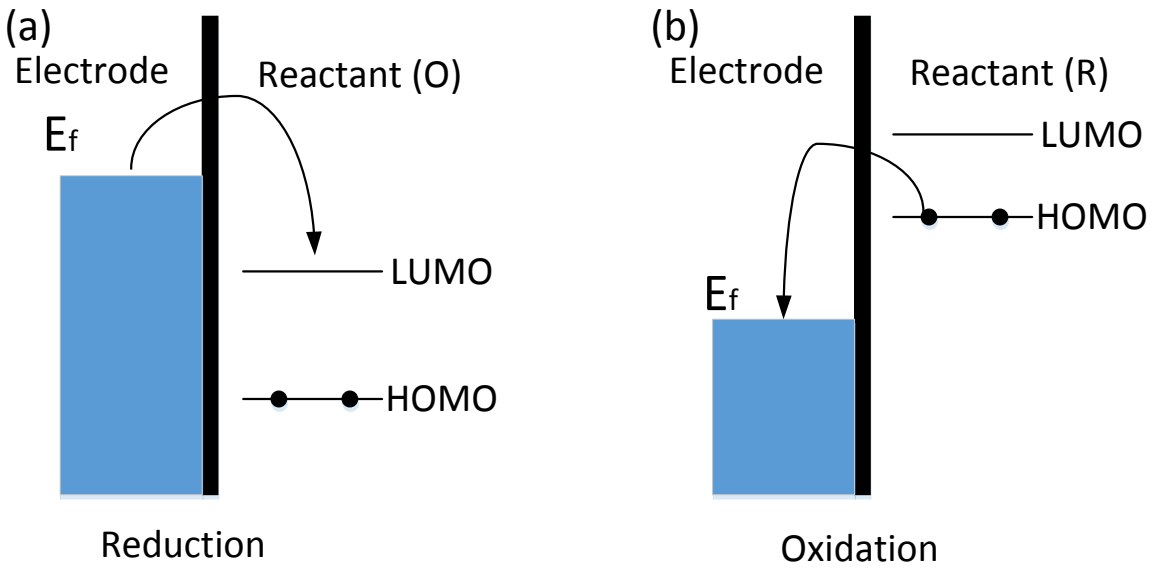

Figure 2.3 (a) Reduction occurs when the Fermi level is higher than the LUMO of the reactant. **(b)** Oxidation occurs when the HOMO of the reactant is higher than the Fermi level.

2.2.2 Kinetics of Electrode Reactions

Thermodynamic only describe the equilibrium, while kinetics explains the mechanism required to maintain the equilibrium. Electrode kinetics theory aims at understanding the rate of electron transfer quantitatively in electrochemical reaction. Assuming a simple, general reaction, one electron transfer happen in two directions, a molecule in solution can accept an electron and become reduced[5].

$$O_{(aq)} + e^-_{(m)} \xrightarrow{k_{red}} R_{(aq)} \quad (2.5)$$

Or the R can be oxidised to O by removing an electron:

$$R_{(aq)} \xrightarrow{k_{ox}} O_{(aq)} + e^-_{(m)} \quad (2.6)$$

Here k_{red} and k_{ox} is the first-order rate constants for the forward (reductive) and backward (oxidative) electron transfer reactions. So the current for the reduction (i_c) and oxidation (i_a) can be described in the equation 2.7 and 2.8.

$$i_c = -FAk_{red}[O]_o \quad (2.7)$$

$$i_a = FAk_{ox}[R]_o \quad (2.8)$$

Here F is the Faraday constant (96485 C mol^{-1}), A is the electrode area (cm^2), $[O]_o$ and $[R]_o$ are the concentrations at the electrode surface. Therefore, the net current (i) flowing in the reaction is

$$i = i_c + i_a = FA(k_{ox}[R]_o - k_{red}[O]_o) \quad (2.9)$$

Similar with chemical reactions, it is reasonable to use transition state model (Fig. 2.4) to describe the electron transfer reactions. The reactants need to overcome an energy barrier to become the product and the summit of energy barrier is termed the transition state[4].

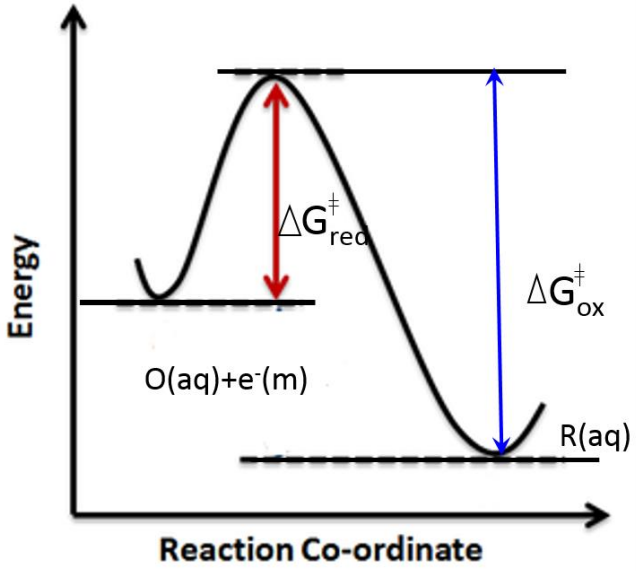

Figure 2.4. Free energy plot for a one electron reduction of O(aq)

So it is a common fact that rate of the reduction reaction is proportional to the barrier it needs to overcome.

$$k_{red} = \mathrm{Z}exp\left(\frac{-\Delta G^{\neq}_{red}}{RT}\right) \quad (2.10)$$

Where $\Delta G^{\neq}_{red}$is the free energy of activation and Z is a frequency factor accounting for the rate of the collisions of electroactive molecules with the electrode surface.

The significant difference of the electrode reaction, when compared to homogenous chemical reactions, is that the potential has a strong effect on the reaction kinetics. A certain reaction happens rapidly at some potential, but not at others. As discussed before, only when the applied potential E equals the equilibrium potential, E_e, there is no net current flowing in the system

and this is the equilibrium state. Any other potential applied will drive the reaction and result in a Faradaic current. The deviation of E from the equilibrium potential is given the term overpotential, η. The potential changes the rate constant by changing the free energy of activation. The dependence of k_{red} and k_{ox} on the potential can be described as follows,

$$k_{red} = Aexp(\left(\frac{-\Delta G_{red}^{\neq}}{RT}\right) \exp\left(\frac{-\alpha F(E-E_0}{RT}\right) \quad (2.11)$$

$$k_{ox} = Aexp(\left(\frac{-\Delta G_{ox}^{\neq}}{RT}\right) \exp\left(\frac{(1-\alpha)F(E-E_0}{RT}\right) \quad (2.12)$$

Here α is the tranfer coefficient, which reflect the symmetry of the barrier to reaction.

These relationship can be simplified by introduction of the standard rate constant, k^0, which is independent of potential.

$$k_{red} = k^0 exp\left(\frac{-\alpha F(E-E_0}{RT}\right) \quad (2.13)$$

$$k_{ox} = k^0 exp\left(\frac{(1-\alpha)F(E-E_0}{RT}\right) \quad (2.14)$$

Equation 2.13 and 2.14 are combined with equation 2.9 to give the Bulter-Volmer equation as follows.

$$i = \mathrm{FA}k^0\left([R]_0 exp\left\{(1-\alpha)(E-E^0)\frac{F}{RT}\right\} - [O]_0 exp\left\{-\alpha(E-E^0)\frac{F}{RT}\right\}\right) \quad (2.15)$$

Bulter-Volmer equation is an important equation to show how net current in the electrochemical system changes with the electrode potential. If k^0 is large, very little or zero overpotential is needed to induce the electrochemical reaction. However, for the process that have a small value of k^0, a high ovepotential is necessary to drive the electron transfer, which indicates an electrochemically irreversible system.

2.2.3 Mass Transport

Electron transfer is not the whole physical process of the electrochemical reaction. There are generally five steps that contribute to the overall kinetics[4].

1) Redox reactants moves to the electrode by mass transport.
2) Reactants adsorb onto the electrode surface.

3) Electron transfer.
4) Products desorb from the electrode surface.
5) Products move away from the electrode by mass transport.

The overall reaction rate will be limited by the slowest step, either electron transfer or mass transport. It has been discussed before that the current varies with potential in an electron transfer rate controlled reaction. In a reaction with fast electron transfer, mass transport may become dominated to the effective reaction. The process associated with mass transport can be divided into three different mechanisms, diffusion, convection and migration.

2.2.3.1 Diffusion

Diffusion is caused by the difference of concentration and aims to maximize the entropy of any systems. The species move from the high concentration area to low concentration ones and the rate is dependent on the concentration gradient at the particular location. It is governed by Fick's two laws, which can be expressed in Equation 2.16 and 2.17.

$$j_{Ox} = -D_{OX}\frac{\partial[\mathrm{Ox}]}{\partial \mathrm{x}} \tag{2.16}$$

$$\frac{\partial[\mathrm{Ox}]}{\partial \mathrm{t}} = D_{OX}\frac{\partial^2[Ox]}{\partial t^2} \tag{2.17}$$

Here j_{Ox} is the diffusional flux of the species O_x, D_{OX} is the diffusion coefficient of Ox and [Ox] is the concentration.

2.2.3.2 Convection

Convection happens because of the mechanical force in the solution, which can be naturally or forced. Natural convection can be caused by the thermal gradients or density differences and are usually not significant in experiments. The other type of movement is forced convection resulted from external forces such as stirring and pumping. The most common example is the rotating disk electrode technique, in which the electrode is rotated to enhance the rate of mass transport. The concentration changes of the species Ox resulting from the convection movement can be described mathematically as Equation 2.18.

$$\frac{\partial[\mathrm{Ox}]}{\partial \mathrm{t}} = -v_x\frac{\partial[Ox]}{\partial x} \tag{2.18}$$

Here v_x is the velocity of solution.

2.2.3.3 Migration

Migration is the movement of the charged species because of the electric field which exists at the electrode/surface interface. The flux of a species *Ox* caused by migration is proportional to concentration of the ion, $[Ox]$, the electric field gradient and the ionic mobility, u_{ox}.

$$j_{ox} \propto u_{ox}[Ox]\frac{\partial E}{\partial x} \qquad (2.19)$$

Here *E* is the potential at a distance *x* from the electrode surface.

In practical experiments, the existence of migration makes the mass transport difficult to control. To simplify this problem, high levels of background electrolyte are added to the solution, usually 100 times the concentration of the reactant to eliminate the migration effect.

2.3 Electrochemical Methods

2.3.1 Cyclic Voltammetry

Cyclic Voltammetry is one of the most important electrochemical techniques with its relative ease of use and high information content into the kinetic and thermodynamic details of many chemical systems. It has found a wide range of applications in the analysis of solids, solutions, polymers as well as membranes[4].

In cyclic voltammetry experiments, the potential of the working electrode is swept linearly forward and backward. The potential changes with time as shown in Fig. 2.5(a) and the basic shape of the current response for cyclic voltammetry experiment is shown in Fig. 2.5(b) below.

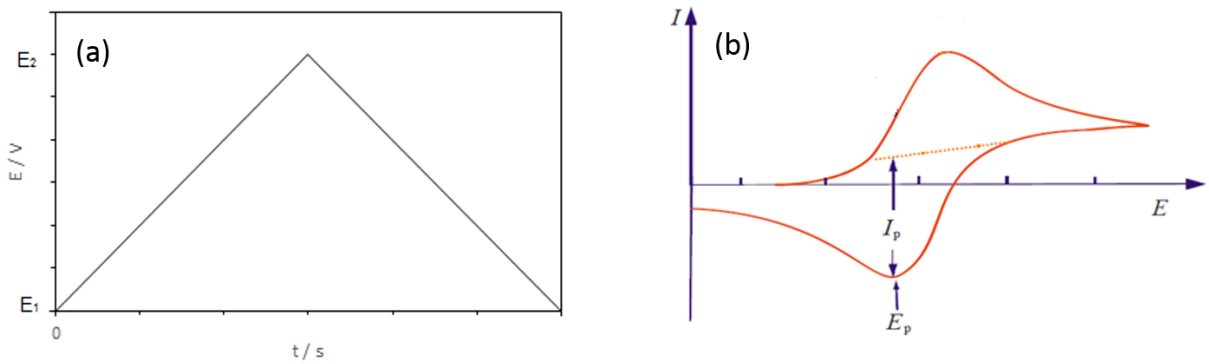

Figure 2.5. (a) A graph of potential against time for a cyclic voltammogram. **(b)** A typical cyclic voltammogram for a reversible electron transfer reaction.

If we consider the forward scan first, the potential of the working electrode is set initially in a value E_1 at which no oxidation occurs because the potential is not positive enough. Then the potential is gradually swept to more positive potential that inducing the oxidation of the reactant and the current starts to pass. The current of the reaction is determined not only by the electrochemical rate constant, k_o but also the surface concentration of the reactant, [A]. As the potential is swept in a positive direction, k increases while [A] decreases because the depletion of reactant is only replenished partially by diffusion from the bulk solution. Initially, the current increases approximately exponentially and then become slower until a maximum is reached. The maximum current is called peak current, I_p, at which the surface concentration of the reactant decreased to zero. All the reactant is depleted as soon as it is diffused to the electrode surface. Once the peak current is attained, the current decreases and is simply controlled the diffusion rate. The potential is reversed from E_2 to E_1 to give the backward scan[6, 7].

The shape of cyclic voltammogram reflects the reversibility of the redox system. For an ideal reversible couple when the mass transport are relatively slower than the electron transfer kinetics, the height of the forward and the reverse current peak are of the same magnitude and the peak separation can be calculated according to equation 2.20, which is independent of scan rate. When the transferred electron number is one, the peak separation is approximately 57 mV at 25℃. The peak current I_p for a reversible system can be determined by Randles-Sevcik expression 2.21.

$$\left|E_p^a - E_p^c\right| = 2.218\frac{RT}{nf} \tag{2.20}$$

$$I_p = -0.446nFA[Ox]_{bulk}\sqrt{\frac{nFvD}{RT}} \tag{2.21}$$

Here, n is number of electron transferred, v is the scan rate, the negative sign is used to conform to a reduction process. The absolute magnitudes of the peak currents for irreversible system is proportional to the square root of scan rate.

In an electrochemically irreversible system, the product diffuses to the bulk solution instead of reacting back on the surface of the electrode. For an irreversible electrode couple, an

appreciable overpotential is required so that the peak separation is wider than the reversible one. For the irreversible system, the Randles- Sevcik expression is changed to equation 2.22.

$$I_p = -0.496\sqrt{\alpha n'}nFA[Ox]_{bulk}\sqrt{\frac{FvD}{RT}} \qquad (2.22)$$

Here, n' is the number of electrons transferred in the rate-determining reaction step, whereas n is the overall transferred electrons per molecule diffusing to the electrode surface.

There exist intermediate cases called quasi-reversible reaction, where the reaction depends both the electron transfer rate and mass transfer rate. In that case, the peak separation is dependent on the scan rate and the peak current is not proportional to the square root of the scan rate. The Fig. 2.6 compares the shape of cyclic voltammogram and the peak current between three different systems.

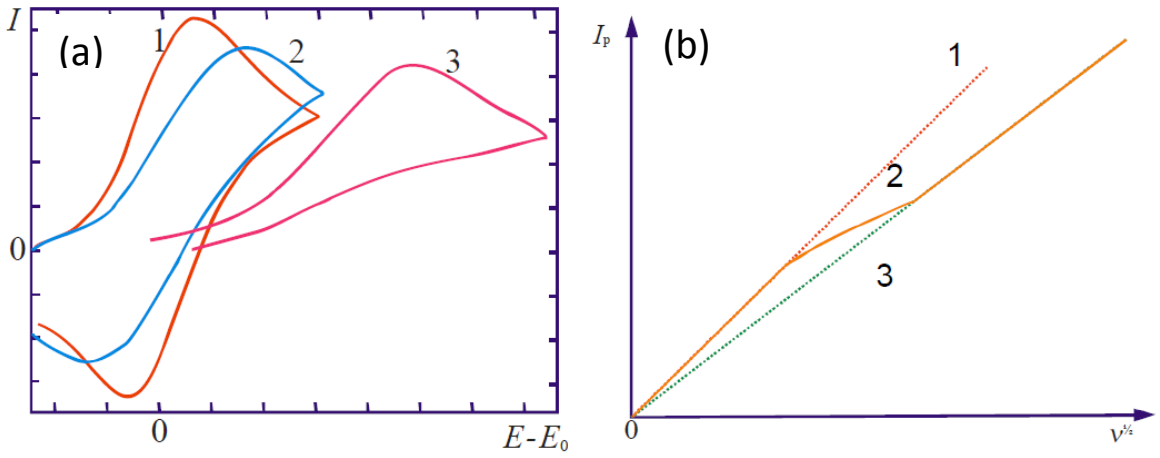

Figure 2.6. (a) Cyclic voltammogram for 1) a reversible, 2) a quasi-irreversible, 3) irreversible electron transfer. **(b)** The plot of peak current versus the square root of scan rate for three systems as before.

2.3.2 Chronoamperometry

There are many other electrochemical techniques besides cyclic voltammetry and one of them is chronoamperometry. In chronamperometry, the potential of working electrode is instantaneously stepped from the value E_1 where the species is inactive to E_2 at which the conversion is completed at the electrode surface (see Fig. 2.7(a)).

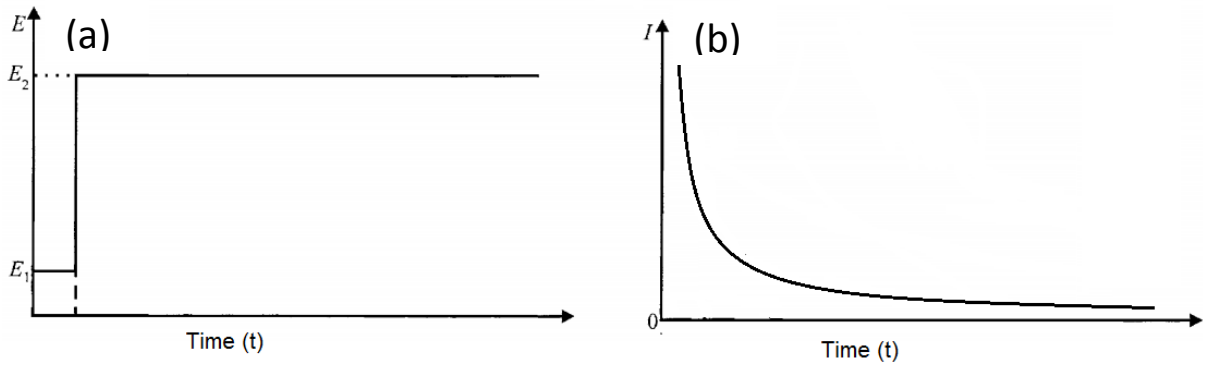

Figure 2.7. (a) The variation of applied potential in a chronoamperometry experiments. **(b)** The current response with time in chronoamperometry.

E_2 is restricted to a potential positive (for oxidation) than the cyclic voltammetric peak potential, therefore the current is only controlled by the diffusion rate of the reactant to the electrode. As the potential is stepped to E_2, there's a sharp increase of the current because the concentration gradients are large due to little time to deplete the electroacive materials. As time progresses, the current decreases gradually until zero because the concentration gradient become shallower and the diffusion layer becomes thicker. The current response as the function of time can be illustrated by Cottrell equation (equation 2.23) and plotted in Fig. 2.7(b). The plot can be linearized by plotting $1/i^2$ against t to determine the diffusion coefficients[6, 7].

$$|i| = \frac{nFAD_A^{1/2}[A]_{bulk}}{\pi^{1/2}t^{1/2}} \qquad (2.23)$$

2.3.3 Electrochemical Impedance Spectroscopy

Electrochemical impedance spectroscopy (EIS) is a powerful measurement tool used to reveal underlying chemical processes in an electrochemical systems, especially suitable for complex non-linear ones. This technique allows the characterization of the surface change and also give detailed information in the kinetics, charge transfer resistance, diffusion coefficients and so on, which is quite useful to tailor the system parameters in order to obtain a desirable effect on a surface. Impedance (Z) is defined as the ability of a circuit to resist the flow of electrical current, but unlike resistance, it is more complex. Usually in the experiments, an AC potential is applied to the electrochemical system and the current through the system is measured. Assume the AC potential (E) is a sinusoidal potential excitation, if the change of the potential is small enough

(typically <10 mV), then the system is a pseudo-linear and the response current (I) will also be a sinusoid at same frequency but shifted in phase (Fig.2.8).

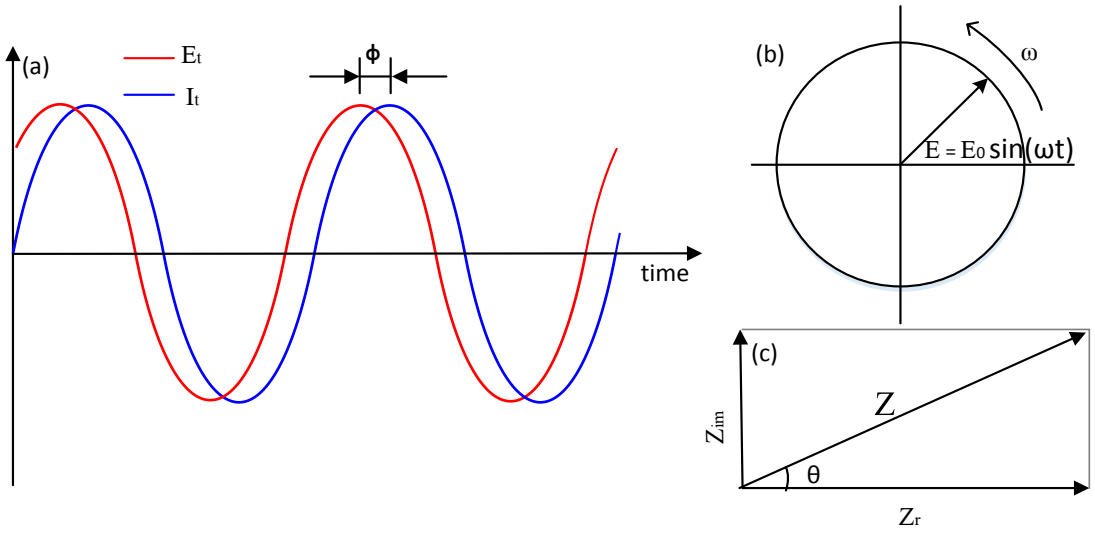

Figure 2.8 (a, b) Phase diagram showing E_t (red) and I_t (blue). **(c)** Phase diagram of impedance

To express EIS mathematically, we can use the equations as follows. E_t is given by the projection on the y-axis (Fig.2.7 (b) and equation 2.24). Since the phase angle difference (ϕ) between E_t and I_t is constant, the I_t can be expressed by equation 2.25.

$$E_t = E_0 \sin(\omega t) \text{ , where } \quad w = 2\pi f \; rad \; s^{-1} \tag{2.24}$$

$$I_t = I_0 \sin(\omega t + \phi) \tag{2.25}$$

The impedance can therefore be expressed as:

$$Z = \frac{E_t}{I_t} = \frac{E_0}{I_0} \frac{\sin(\omega t)}{\sin(\omega t + \phi)} \tag{2.26}$$

According to Fig. 2.7 (c), the total impedance can be expressed by the real component (Z_r) and imaginary component (Z_{im}). In order to represent the relative magnitude and phase of the signals more clearly, complex exponentials are introduced to simply the mathematics. All the parameters are expressed in polar form as follows.

$$E_t = E_0 e^{j\omega t} \tag{2.27}$$

$$I_t = I_0 e^{j(\omega t + \phi)} = I_0 e^{j\omega t} e^{j\phi} \tag{2.28}$$

$$Z = \frac{E_t}{I_t} = \frac{E_0}{I_0} e^{-j\omega} \tag{2.29}$$

If Z has the magnitude $|Z|$ and the phase θ, according to Eular's formula (equation 2.30)

$$Z = Z_r + Z_{im} = |Z|(\cos\theta + j\sin\theta) = |Z|e^{j\theta} \quad (2.30)$$

Any electrochemical cell can be illustrated by an equivalent electrical circuit which includes resistances, capacitances or inductances [electroanalytical methods]. If there's only an ideal resistor in the system, the impedance of the circle equals the resistance of the resistor and has no imaginary part, so the phase angle is zero (equation 2.31)

$$Z = \frac{E_0}{I_0} = R, \ \ \theta = 0 \quad (2.31)$$

If there is a single capacitance, the impedance can be calculated as follows,

$$E_t = E_0 e^{j\omega t}$$

$$I = \frac{dQ}{dt} = \frac{d(CE_t)}{dt} = C\frac{dE_t}{dt}$$

$$I = C\frac{d(E_0 e^{j\omega t})}{dt} = j\omega C E_0 e^{j\omega t}$$

$$Z = \frac{E}{I} = \frac{1}{j\omega C} = \frac{-j}{\omega C} = -\frac{j}{2\pi f C} = -jX_C \text{ , where } X_C = \frac{1}{\omega C} \quad (2.32)$$

X_C is known as the capacitive reactance with Ohms as the unit, which represents the internal resistance that restricted the current flow through the capacitor when the capacitor charges or discharges. Unlike resistance with a fixed value, capacitive reactance changes with the applied frequency. According to the calculation above, the impedance of a pure capacitor only has the imaginary part and phase angle is -90°. Also, the value of impedance is proportional to the reciprocal of frequency[6].

There are two common types of plots to display the impedance, Bode plot and Nyquist impedance plot (also called complex impedance plane). A Bode plot shows the impedance magnitude ($|Z|$) and phase angle (θ) against the frequency (f) of AC potential. The impedance magnitude and the frequency are plotted using logarithmic scale. A Nyquist plot display the real impedance (Z_r) in x-axis and imaginary impedance (Z_{im}) in y-axis.

The examples above are the most simple and ideal cases, while the real systems are more complex. The most common system is the redox reaction at flat electrodes. For a purely kinetically controlled electrode reaction, the equivalent circuit can be demonstrated as the double-layer C_d in parallel with the charge transfer resistance capacitance R_Ω (Fig. 2.9(a)).

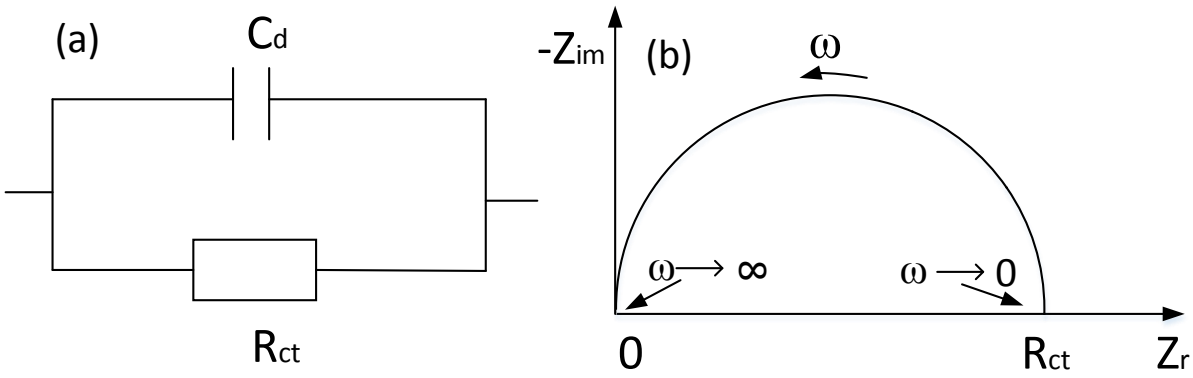

Figure 2.9. For purely kinetically controlled electrodes **(a)** Equivalent circuit **(b)** Nyquist plot

The Nyquist plot for such a circuit is a classic semicircle with the centre on the Z_r axis at Z_r= 0.5 R_{ct} and diameter R_{ct}. The impedance tends to be R_{ct} at low frequency and zero at high frequency and the maximum of the semicircle is located at $\omega_{max} = 2\pi f = \frac{1}{R_{ct}C_d}$.

Next, the effect of diffusion on the impedance properties are taken into account. The system is diffusion controlled at low frequencies. Hence, Warburg impedance W is introduced to represent the impedance associated with planar diffusion to the flat electrode. Warburg impedance has the equal real and imaginary components, therefore it's a linear plot with a slope of 45^o in the Nyquist plot. The electrolyte resistance R_Ω is also considered, which finally give the most common system, Randles Model. The equivalent circuit of Randles Model is displayed as Fig. 2.10.

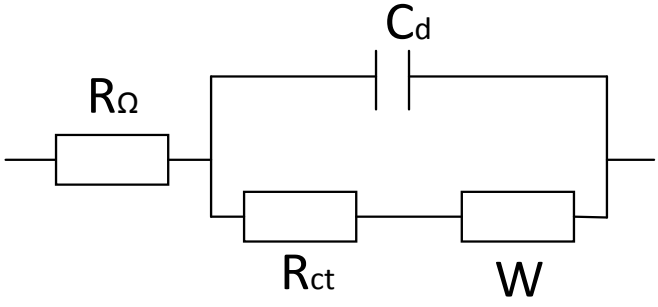

Figure 2.10. Randles equivalent circuit

And the impedance plot in the complex plane is shown in Fig. 2.11.

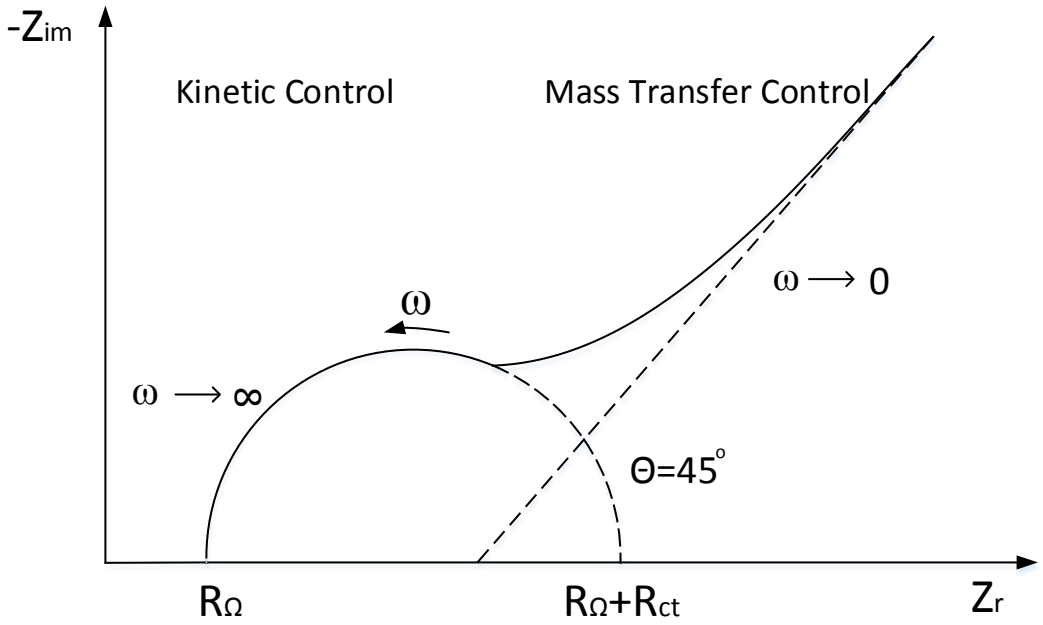

Figure 2.11. Nyquist plot of the impedance of the Randles equivalent

It gives a semicircle for high frequency (kinetic controlled) and a linear plot for low frequency (mass transfer controlled). The value of R_Ω and R_{ct} can be obtained from the intersection point of the semicircle at the Z_r axis. The maximum of the semicircle is located at $\omega_{max} = 2\pi f = \frac{1}{R_{ct}C_d}$, from which the C_d can be obtained.

2.3.4 Rotating Disk Electrode

The rotating disk electrode (RDE) is one of the common hydrodynamic electrode systems, which has wide applications in corrosion, electrocatalysis, fuel cell research and so on. In a RDE system, the working electrode consists of a disk of electrode material imbedded in a rod of an insulting material. It is connected to a motor and rotated by vertical axis at a certain frequency (angular velocity, ω) during the electrochemical measurements (Fig.2.12 (a)). The 2-dimensional flow profile for the rotating disc is illustrated in Figure 2.12(b). The solution is dragged to the surface by spinning disk and at same time expelled radially outwards from the centre due to the centrifugal force. The flow of fresh solution from the bulk, which is perpendicular to the electrode, replenish the fluid at the disk surface[6].

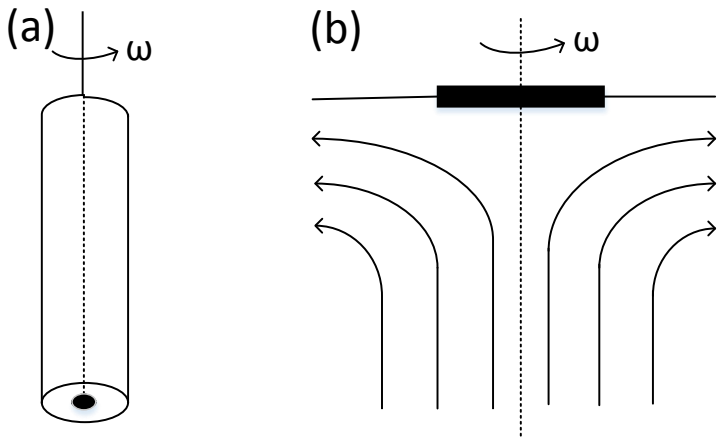

Figure 2.12 (a) A rotating disk electrode **(b)** Schematic drawing of 2-dimensional flow pattern at a rotating disc

In the rotating disk electrode systems, the concentrations of all species beyond a certain distance from the electrode, δ, is equal to the bulk values because of the convection. Within the layer $0 \leq x \leq \delta$, there is less solution movement and diffusion dominates. δ is introduced similarly with the diffusion layer in the steady-state mass transport. In the static macroelectrode, the diffusion layer will become thicker and thicker over time and lead to the current decay, which is observed as a peak in cyclic voltammetry. However, the thickness of diffusion layer at a rotating disk electrode is a constant in certain rotating speed, which results in the limiting current.

To quantitatively understand how the different parameters (such as rotation rates, solution viscosity and electrode dimensions) affect the current value, the mathematic equation is introduced. The flux of species *j*, J_j , is

$$J_j = -D_j \nabla C_j - \frac{z_j F}{RT} D_j C_j \nabla_{\emptyset} + v \cdot C_j \qquad (2.33)$$

Here on the right side, the first term represents diffusion, the second, migration and the last, convection due to the rotating of the electrode. The ionic migration is negligible in a solution with an excess of the supporting electrode. The variation of C_j with time can be given by

$$\frac{\partial C_j}{\partial t} = -\nabla \cdot J_j = div\, J_j \qquad (2.34)$$

Combining these two equations, we obtain the general convective-diffusion equation

$$\frac{\partial C_j}{\partial t} = D_j \nabla^2 C_j - v \cdot \nabla C_j \qquad (2.35)$$

The ∇ here is used to describe the gradient in three dimensions and ∇^2 is Laplacian operation.

If we consider the limiting current condition first, at $y = 0$, $C = 0$ and $\lim_{y\to\infty} C = C_{bulk}$ (y is the verticle axis across the centre of the electrode). After mathmatical processing, the Levich equation is obtained:

$$I_{lim} = 0.62nFAD_j^{2/3}\omega^{1/2}v^{-1/6}C_{j,bulk} \quad (2.36)$$

Here A is the electrode area (in m^2), D_j is the diffusion coefficient of species (in m^2s^{-1}), ω is angular frequency of the rotating electrode (in rad s^{-1}), v is the kinematic viscosity of the solution (in $m^2\ s^{-1}$) and $C_{j,bulk}$ is the bulk concentration of species (in mol m^{-3}).

The Levich equation indicates that the limiting current is proportional to the square root of the angular frequency. The plot of I_{lim} against $\omega^{1/2}$ will be a straight line and the diffusion coefficient of the species can be calculated from the slope.

However, the Levich equation is only suitable for the mass-transfer-limited condition. So for mixed kinetic and diffusion limiting current, the Koutecký-Levich equation is introduced,

$$\frac{1}{i} = \frac{1}{i_K} + \frac{1}{i_{l,c}} = \frac{1}{i_K} + \frac{1}{0.62nFAD_j^{2/3}\omega^{1/2}v^{-1/6}C_{j,bulk}} \quad (2.37)$$

Here, i_K represents the current under the kinetic limitation, that is mass transfer is efficient enough to maintain the concentration at the electrode surface same as the bulk solution. The plot of $1/i$ against $1/\omega^{1/2}$ is a line which has the same slope with the Levich plot and intercept with y axis at $1/i_K$.

2.4 Reference

1 Samec Z, Mareček V and Koryta J. *Journal of Electroanalytical Chemistry and Interfacial Electrochemistry*, 1977, **83**, 393-397.

2 R. P. Buck and R. W. Eldridge, *Anal. Chem*., 1965, **37**, 1242–1245.

3 S. Kalinowski and Z. Figaszewski, *Meas. Sci. Technol*., 1995, **6**, 1050–1055.

4 A. C. Fisher, Electrode Dynamics, *Oxford University Press*, Oxford, 1996.

5 A. J. Bard and L. R. Faulkner, Electrochemical methods: Fundamentals and applications, 2nd edn., *John Wiley*, New York; Chichester, 2001.

6 F. Scholz, Electroananlytical Methods, *Springer-Verlag*, Berlin, Heidelberg, 2005.

7 R. Compton and C. Bank, Understanding Voltammetry, 2nd edn., *Imperial College Press*, 2011.

Chapter 3: Intrinsically Porous Polymer Protects Supported Catalytic Gold Particles for Enzymeless Glucose Oxidation

Chapter Abstract

The enzymeless glucose oxidation process readily occurs on nano-gold electrocatalyst at pH 7, but it is highly susceptible to poisoning (competitive binding), for example from protein or chloride. It is shown here that gold nanoparticle catalyst can be protected against poisoning by a polymer of intrinsic microporosity (PIM-EA-TB with BET surface area 1027 m^2g^{-1}). This PIM material when protonated, achieves the catalyst protection effect by (i) size selective repulsion of larger protein molecules (albumins) and (ii) membrane ion selection effects due to limiting the chloride poisoning interactions with the catalysts. PIM materials allow "environmental control" to be introduced in electrocatalytic processes.

Graphical Abstract:

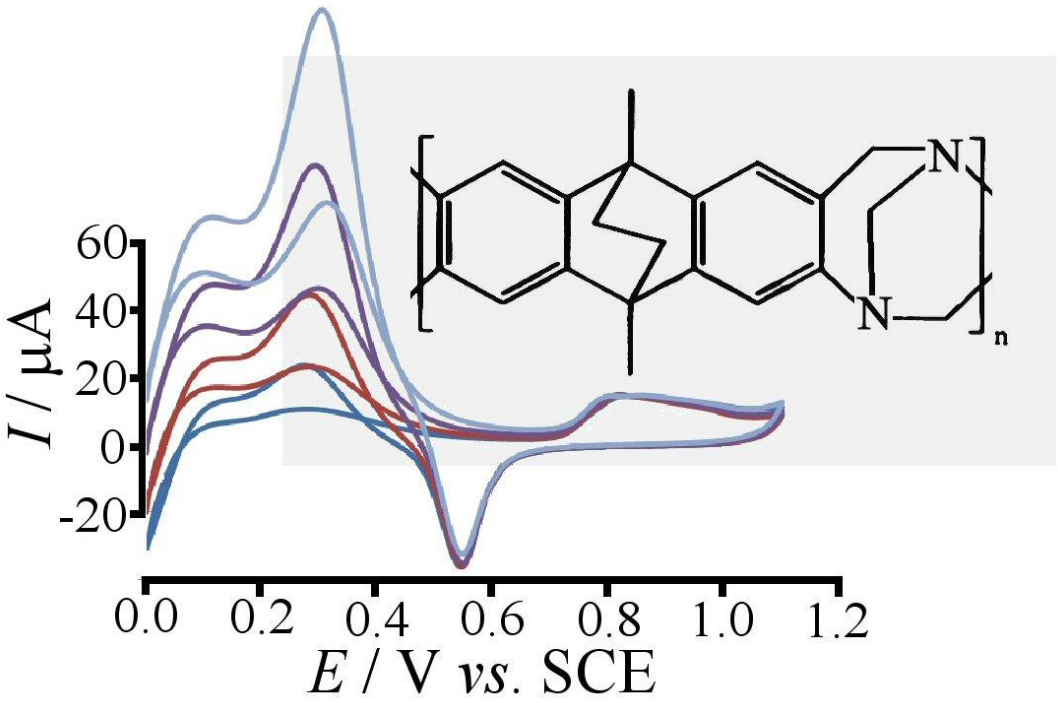

Chapter Publications

This chapter has been published in:

Y. Rong, R. Malpass-Evans, M. Carta, N. B. McKewon, G. A. Attard and F. Marken. *Electroanalysis*, **2014**, 26, 904-909.

Acknowledgement

I would like to thank Dr. Richard. Malpass-Evans, Dr. Mariolino Carta, Prof. Gary Attard and Prof. Neil McKeown for the supply of PIM material and helpful discussion.

3.1 Introduction

New materials in electrochemistry offer opportunities for improved devices and processes and in the recent years several cases of interesting novel porous solids, e.g. metal-organic frameworks[1], zeolitic materials[2], or mesoporous films[3], have emerged. In terms of polymeric materials, there have been many areas of progress including gels[4], conducting polymers[5], and brushes[6]. The recent development of polymers with intrinsic microporosity (PIMs) and similar novel materials[7] is particularly interesting with a range of potential applications in electrochemical technology. Uncharged PIM materials have been proposed[8] and developed for gas storage[9,10], gas separation[11–13], and as sensor component[14]. The structurally highly rigid and disordered PIM backbone achieves open packing to generate novel properties due to permanent microporosity. When charged, these PIM materials introduce ion selectivity, permselectivity, and further porosity effects which are closely linked to the molecular structure and functionalization of the backbone. Physicochemical characteristics are related to those observed for hydrogels[15,16] rather than those associated with polymeric systems. To date, potential applications are based on PIM-gas interaction, but our recent publication[17] has demonstrated benefits of PIM-electrolyte interactions and potential applications in solution phase electrocatalysis.

The preparation of amine-containing PIMs based on a polymerisation reaction involving the formation of Tröger's base (TB) was reported[18]. Thus, 2, 6(7)-diamino-9, 10-dimethylethanoanthracene was polymerised with dimethoxymethane in trifluoroacetic acid to give PIM-EA-TB (Fig.3.1) with high molecular mass (Mw >70,000 g mol^{-1}) and with an apparent BET surface area of 1027 m^2g^{-1}. This polymer backbone is readily protonated at the tertiary nitrogens to give a rigid poly-cationic framework.

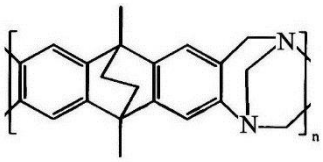

Figure 3.1. Molecular structure of PIM-EA-TB

Glucose oxidation is studied predominantly in the context of glucose sensing, enzymatic or non-enzymatic[19], and as in vivo energy source in enzymatic fuel cells[20]. The glucose concentration in a typical healthy individual is 4-7 mM. The enzymeless oxidation of glucose

on gold is of considerable interest[21,22] and can be seen as a more robust but less selective alternative technology. Pulse methods have been developed to overcome gold catalyst poisoning and interferences[23] and to control pH[24]. Chiral selectivity has been induced on gold electrocatalytst surfaces[25]. Novel high surface area gold electrodes have been proposed for more effective glucose oxidation even at lower pH[26,27] approaching conditions in blood serum. However, more progress is required to make gold nanoparticle catalysts as effective as biological catalysts. A considerable challenge remains in overcoming poisoning of the gold electrocatalysts under in vivo conditions.

It is shown here that the properties of PIM polymer membranes spin-coated over the gold nanoparticle catalyst can help protecting the catalyst from poisoning. The effect of the PIM membrane is studied (i) on the gold nanoparticle catalyst formation, (ii) on the electrocatalytic glucose oxidation mechanism, (iii) on the effect of protein on gold catalyst poisoning, and (iv) on the effect of chloride on gold catalyst poisoning in phosphate buffer at pH 7. PIM membranes are proposed as a versatile new class of materials for electrochemistry in particular for controlling the reaction environment in electrocatalytic processes.

3.2 Experimental

3.2.1 Chemical Reagents

Potassium gold(III) tetrachloride, D-(+)-glucose, albumin from bovine serum, sodium chloride, phosphoric acid (85%), potassium chloride, sulphuric acid (95%-98%), and sodium hydroxide were purchased from Aldrich or Fisher Scientific and used without further purification. PIM-EA-TB was prepared following a literature recipe[18]. Solutions were prepared with filtered and deionized water of resistivity 18.2 MΩ cm from a Thermo Scientific water purification system (ELGA).

3.2.2 Instrumentation

A potentiostat system (IVIUM Compactstat) was employed with a Pt wire counter electrode and a KCl-saturated calomel reference (SCE, Radiometer, Copenhagen). The working electrode was prepared from ITO coated glass (tin-doped indium oxide films sputter-coated

onto glass, active area 10 mm × 10 mm, resistivity *ca.* 15 Ω per square) obtained from Image Optics Components Ltd (Basildon, Essex, UK). ITO electrodes were rinsed with ethanol and water, heat-treated in a tube furnace (Elite Thermal System Ltd) for 30 minutes at 500 °C, and then re-equilibrated to ambient conditions. All experiments were conducted at a temperature of 293±2K.

3.2.3 Gold Nanoparticle Deposition Method

A gold (III) solution was prepared by dissolving 1 mM $KAuCl_4$ in 0.1 M KCl addition of sulphuric acid to pH 2. Electrodeposition was performed in chronoamperometry mode. ITO electrodes were pre-treated at 1 V vs. SCE for 10 s followed by plating at -0.2 V vs. SCE for 200 s, rinsing with water, and drying under ambient conditions.

3.2.4 Polymer with Intrinsic Microporosity Coating Method

Initially, a solution of 1 mg cm^{-3} PIM-EA-TB in chloroform was applied directly by dipping the electrode followed by drying under ambient conditions. Improved coatings were obtained by spin-coating (Laurell WS-650Mz-23NPP, 1500 rpm for 30 seconds).

3.3 Results and Discussion

3.3.1 Electrodeposition of Catalytic Gold Nanoparticles onto Tin-Doped Indium Oxide (ITO) Substrates

The gold electrodeposition approach was selected based on an aqueous solution of 1 mM $KAuCl_4$ in 0.1 M KCl at pH 2 (acidified with H_2SO_4). The deposition experiments were conducted at -0.2 V vs. SCE for 200 s (if not stated otherwise) to form a uniform deposit of gold nanoparticles on the ITO substrate (see Fig.3.2A, B). Particles are typically 100 nm to 200 nm in diameter and well distributed over the electrode surface.

In cyclic voltammetry experiments these gold deposits immersed in 0.1 M phosphate buffer at pH 7 give stable voltammetric responses (see Fig.3.3A) with gold oxidation (see peak I_{ox} at

0.80 V vs. SCE) and gold back-reduction (see peak I_{red} at 0.55 V vs. SCE) indicative of an active gold surface.

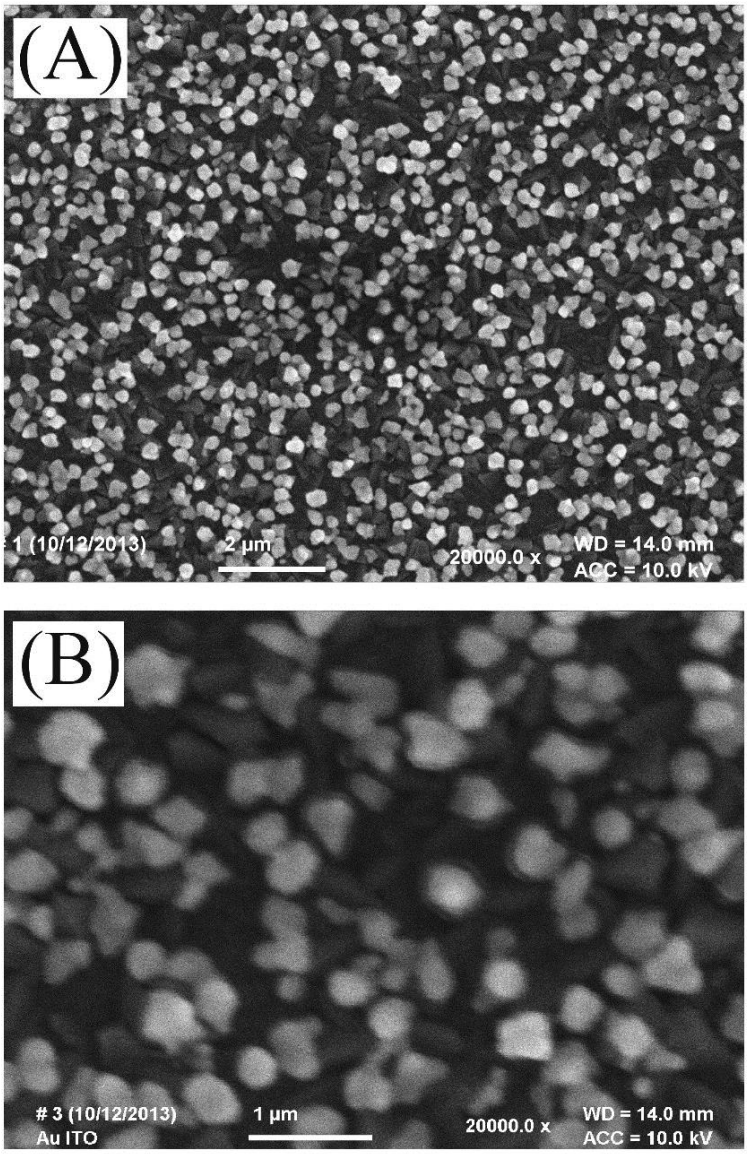

Figure 3. 2. Scanning electron microscopy images for (A) gold nanoparticles grown on ITO for 200 s, (B) higher magnification image of gold nanoparticles.

The gold electrodeposition was repeated in the presence of a PIM film spin-coated onto the ITO surface (ca. 500 nm thickness). The same type of gold nanoparticle deposit was formed (confirmed by voltammetry and electrocatalysis experiments, *vide infra*). But unfortunately these films were unstable and easily peeled off the surface together with the PIM film. Better quality films were obtained by first electroplating gold nanoparticles onto ITO and then coating with PIM. Drop-coating PIM resulted in film imperfection, but spin-coating a solution 1 mg cm^{-3} PIM in chloroform at 1500 rpm (see experimental) resulted in high quality film coatings.

3.3.2 Glucose Oxidation on Catalytic Gold Nanoparticles on Tin-Doped Indium Oxide (ITO) Substrates

The oxidation of glucose on gold nanoparticles immersed in phosphate buffer pH 7 has been reported previously and a typical anodic current peak is seen at 0.3 V vs. SCE (see Fig.3.3). As expected for a surface-catalytic kinetically controlled current response, this peak is not affected by scan rate (see Fig.3.3B) but strongly affected by the gold nanoparticle catalyst deposition time (see Fig.3.3C, peak II, note that this peak is observed most clearly during the potential sweep towards negative potentials). A plot of the effect of the gold nanoparticle deposition time on the glucose oxidation peak current is shown in Figure 3.3D. An improvement in the catalytic signal is seen up to approximately 400 s electrodeposition.

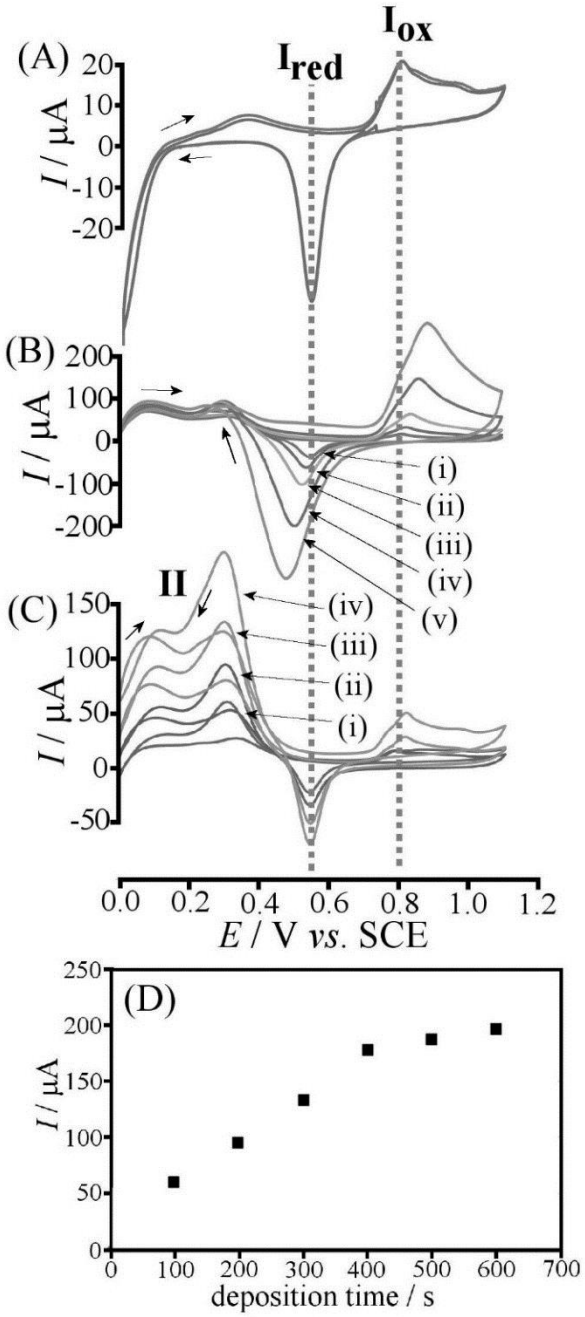

Figure 3. 3. (A) Cyclic voltammograms (first and second cycle, scan rate 5 mVs^{-1}, start point 0.0 V vs. SCE) for gold nanoparticles on ITO immersed in 0.1 M phosphate buffer pH 7. (B) As before, but with 8 mM glucose and scan rate (i) 5, (ii) 10, (iii) 20, (iv) 50, (v) 100 mVs^{-1}. (C) As before, but with 8 mM glucose, scan rate 5 mVs^{-1}, and (i) 100 s, (ii) 200 s, (iii) 300 s, (iv) 600 s gold nanoparticle deposition time. (D) Plot of the glucose oxidation peak versus gold nanoparticle deposition time.

An investigation of the effect of the phosphate buffer concentration on the catalytic process provides further insight into the mechanism. As shown in Figure 3.4A, a significant enhancement of the catalytic current for glucose oxidation is observed upon lowering the phosphate concentration. When plotted versus logarithm of phosphate concentration, the

catalytic current exhibits an approximately linear dependence. This can be reconciled with a Langmuirian binding model where the kinetically controlled glucose oxidation current I_G is proportional to the coverage with glucose Θ_G at the active surface sites (equation 3.1).

$$I_G = \text{constant} \times \Theta_G = \text{constant} \times \frac{K_G[G]}{1 + K_G[G] + K_P[P]} \tag{3.1}$$

Here, K_G and K_P represent Langmuirian binding constants for glucose and a competing molecule or ion. For the special case of half coverage, that is $K_G[G] \approx K_P[P]$ (here observed for 8 mM glucose and 100 mM phosphate buffer), an approximately linear relationship around the point of half-coverage is possible, which suggests that here $K_G / K_P \approx [P]/[G] \approx 12$. Therefore glucose is bound approximately an order of magnitude more strongly compared to other components in the phosphate buffer.

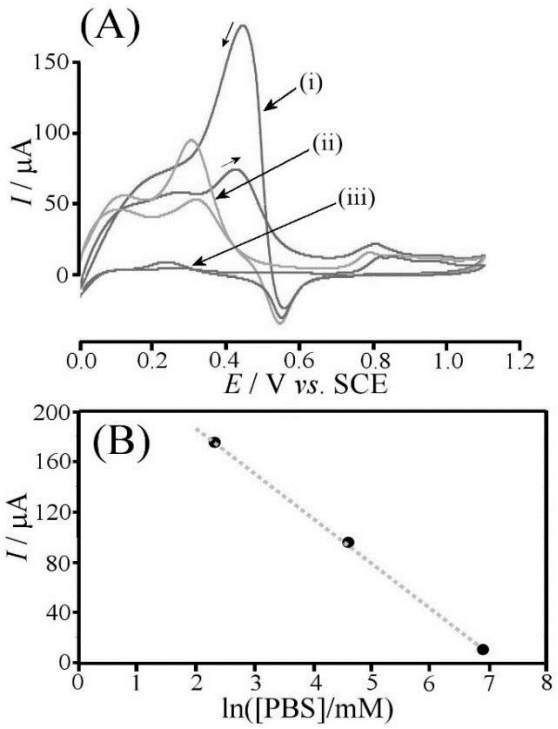

Figure 3. 4. (A) Cyclic voltammograms (scan rate 5 mVs^{-1}, start point 0.0 V vs. SCE) for the oxidation of 8 mM glucose at gold nanoparticles on ITO immersed in (i) 10, (ii) 100, (iii) 1000 mM phosphate buffer pH 7. (B) Plot of the peak current versus logarithm of phosphate buffer concentration.

Next, the effect of glucose concentration is investigated. Figure 3.5 shows data for gold nanoparticle catalyst in 0.1 M phosphate buffer pH 7 for different glucose concentrations. At low glucose levels an approximately linear increase in glucose oxidation current is observed with plateauing at glucose concentration higher than 12 mM. This observation is in agreement with the Langmuirian binding model introduced above. The binding constant can be estimated (here from the point of third coverage, where $\Theta_G = \frac{K_G[G]}{1 + K_G[G] + K_P[P]} = \frac{1}{3}$ with $K_G[G] \approx K_P[P]$) as $K_G \approx 200$ mol^{-1} dm^3.

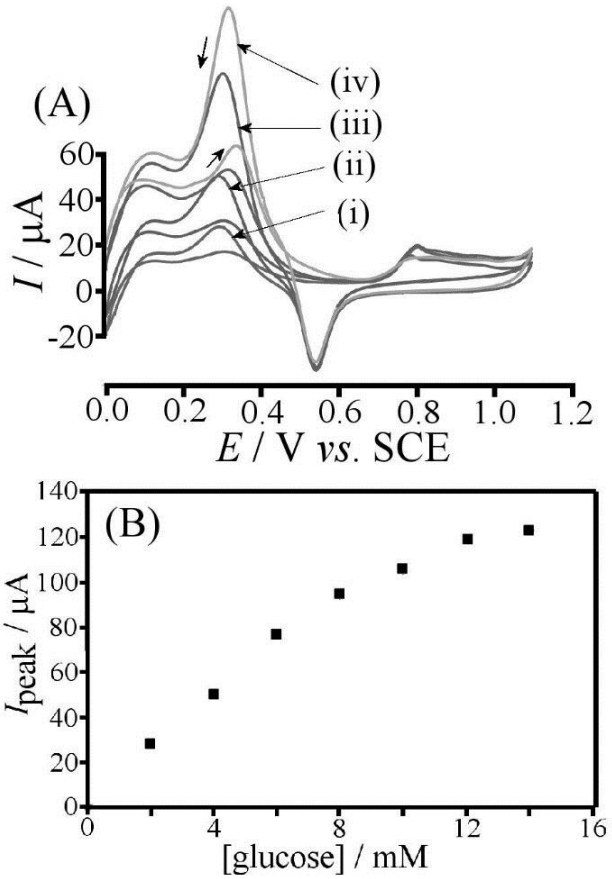

Figure 3. 5. (A) Cyclic voltmmograms (scan rate 5 mVs^{-1}, start point 0.0 V vs. SCE) for the oxidation of (i) 2, (ii) 4, (iii) 8, (iv) 14 mM glucose at gold nanoparticles on ITO immersed in 0.1 M phosphate buffer pH 7. (B) Plot of the peak current versus glucose concentration.

3.3.3 Suppressing Gold Nanoparticle Catalyst Poisoning with Polymer of Intrinsic Microporosity (PIM) Coating

Phosphate has been shown to compete with glucose for the active catalyst surface sites and many other molecules and ions potentially interfere or poison the catalyst surface. In order to explore poisoning and the remediating effects of a porous PIM-EA-TB polymer film two cases are studied: (i) bovine serum albumin and (ii) chloride.

The coating of the polymer of intrinsic microporosity (PIM) PIM-EA-TB is applied by spin-coating to give approximately 500 nm thick films. This type of film has recently been shown to allow small ions and molecules such as formic acid to pass with electrocatalysts working just as well with or without this coating (demonstrated for formic acid oxidation on palladium[17]). Here the PIM coating is shown to not detrimentally affect the glucose oxidation (see Fig.3.6A) with clear oxidation peaks detected at 0.3 V vs. SCE. The plot of the peak current versus glucose concentration has an extended range into higher glucose concentrations (see Fig.3.6B), indicative of less competition to phosphate buffer (the activity of the phosphate buffer is believed to be lower in the PIM environment).

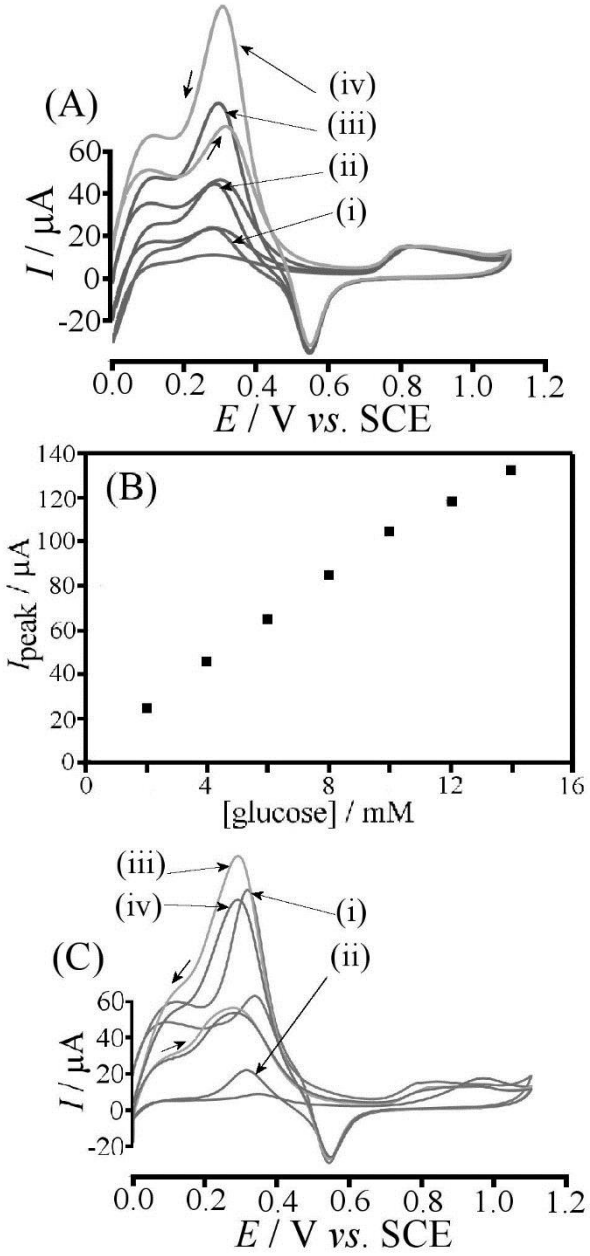

Figure 3. 6. (A) Cyclic voltammograms (scan rate 5 mVs^{-1}, start point 0.0 V vs. SCE) for the oxidation of (i) 2, (ii) 4, (iii) 8, (iv) 14 mM glucose at gold nanoparticle on ITO, coated with 500 nm PIM, and immersed in 0.1 M phosphate buffer pH 7. (B) Plot of the peak current for glucose oxidation versus glucose concentration. (C) Cyclic voltammograms (scan rate 5 mVs^{-1}) for the oxidation of 14 mM glucose at gold nanoparticle on ITO immersed in 0.1 M phosphate buffer pH 7 (i) without and (ii) with BSA (3 mg in 50 cm^{-3} solution) and the same experiment with PIM coating (iii) without and (iv) with BSA.

When adding bovine serum albumin (BSA) as a known catalyst poison[28], a dramatic change is observed in the glucose oxidation current. Fig.3.6C (i) and (ii) show the current for glucose oxidation on bare gold nanoparticle catalyst before and after addition BSA (3 mg in 50 cm^3 solution), respectively. The same experiment was repeated with PIM coating (see Fig.3.6C (iii)

and (iv)) with no detrimental effect of the protein. It is likely that the PIM coating can repel the protein based on size exclusion.

A further severe poisoning effect on the gold nanoparticle electrocatalyst is induced by chloride. An addition of 10 mM chloride into 0.1 M phosphate buffer pH 7 almost completely eliminates the catalytic glucose oxidation (see Fig.3.7A (i) and (ii)). When the PIM coating is applied this effect is considerably less dramatic. In Fig.3.7A (iii) and (iv) the glucose oxidation for 8 mM glucose in 0.1 M phosphate buffer pH 7 is shown without and with 10 mM chloride, respectively, and only a 50% drop in current occurs. Therefore the PIM membrane changes the access of chloride to the catalyst surface (e.g. by competition of phosphate and chloride for PIM anion sites).

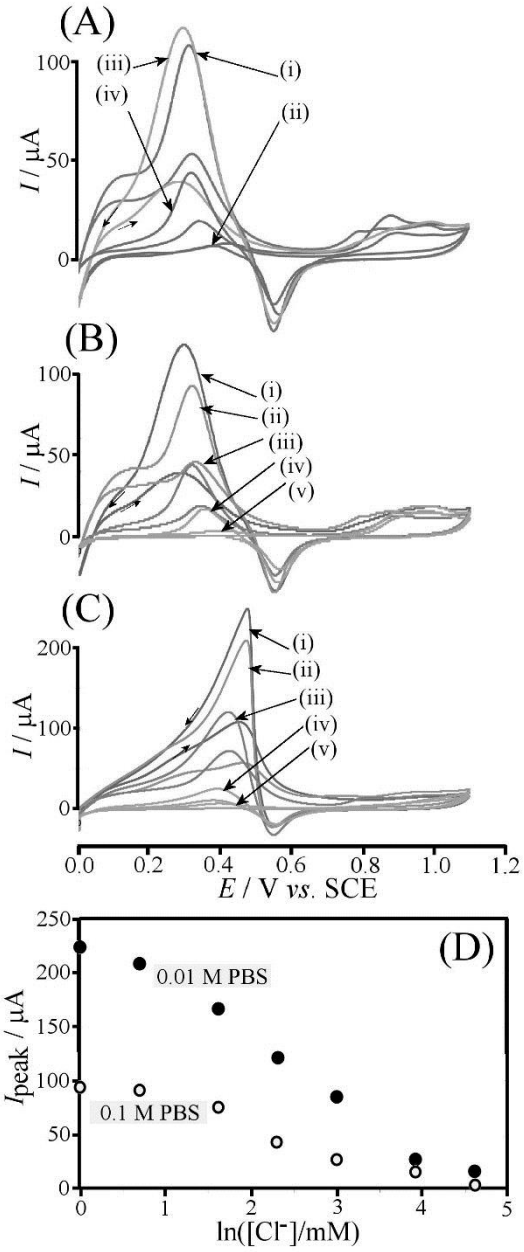

Figure 3. 7. (A) Cyclic voltammograms (scan rate 5 mVs^{-1}, start point 0.0 V vs. SCE) for the oxidation of 8 mM glucose at gold nanoparticles on ITO immersed in 0.1 M phosphate buffer pH 7 (i) without and (ii) with 10 mM chloride and the same experiment with PIM coating (iii) without and (iv) with 10 mM chloride. (B) (A) Cyclic voltammograms (scan rate 5 mVs^{-1}) for the oxidation of 8 mM glucose at gold nanoparticles on ITO with PIM coating immersed in 0.1 M phosphate buffer pH 7 with (i) 0, (ii) 2, (iii) 10, (iv) 50, (v) 100 mM chloride. (C) (A) Cyclic voltammograms (scan rate 5 mVs^{-1}) for the oxidation of 8 mM glucose at gold nanoparticles on ITO with PIM coating immersed in 0.01 M phosphate buffer pH 7 with (i) 0, (ii) 2, (iii) 10, (iv) 50, (iv) 100 mM chloride. (D) Plot of the peak current for glucose oxidation versus chloride concentration for 0.1 and 0.01 M phosphate buffer pH 7.

These experiments were repeated systematically for a range of chloride concentrations and for two phosphate buffer concentrations. The plot in Figure 3.7D shows both the effect of the lower buffer concentration increasing the glucose oxidation current and the effect of chloride

reducing the catalyst activity. The observed data plot is again consistent with the model of competitive Langmuirian binding (equation 3-1). Interestingly, with the PIM coating the gold nanoparticle electrocatalyst is able to effectively operate even in 20 mM chloride. Typical blood serum levels of chloride are higher and therefore the improvement in catalyst performance is still not sufficient. However, the observed improvement with a thin PIM film coating is promising and future development could focus on (i) improved PIM materials in terms of molecular structure and pore structure for controlling access of poisons to the catalyst and (ii) improved design of the "electrocatalyst PIM environment" to optimise conditions in the reaction zone close to the active catalyst sites.

3.4 Conclusion

It has been shown that novel PIM materials such as PIM-EA-TB with extremely high surface area and ability to be protonated (to be semipermeable towards anions) provide a new class of electrochemically effective components for application in electrocatalysis, for example for energy harvesting and sensing. The rigid nature of the PIM polymer backbone minimises structural fluctuations and leads to a stable pore size for selective transport of neutral and charged species. When protonated, the PIM-EA-TB film exhibits some degree of anion selectivity with potential benefits in electrocatalytic processes (e.g. widening the linear range, influencing competitive binding equilibria). Here, the oxidation of glucose on gold at pH 7 in phosphate buffer is investigated as a first model case. Three types of effects on the catalyst performance are observed:

(i) The size selection effect of PIM pores allows poisoning from larger proteins such as bovine serum albumin to be suppressed

(ii) The anion selection effect allows access of chloride to the catalyst surface to be reduced (in competition to phosphate)

(iii) The change in anion activity in the catalyst reaction zone (e.g. reduced phosphate binding relative to glucose binding and extended linear range)

In future novel PIM materials could be designed and further improved by molecular control over pore size, pore shape, pore charge distribution, etc. In contrast to hydrogels, the novel PIM materials are highly stable and more dense to impose a stronger effect on the membrane

permeability and catalyst environment. Rigidity and the molecular structure of the PIM polymer backbone play a key role in introducing new functionality and novel effects.

3.5 References

1 A. Morozan and F. Jaouen, *Energy Environ. Sci.*, 2012, **5**, 9269–9290.

2 Z. Dai and H. Ju, *Trends Anal. Chem.*, 2012, **39**, 149–162.

3 A. Walcarius, *Chem Soc Rev*, 2013, **42**, 4098–4140.

4 D. Lin and J. Che, *Prog. Chem.*, 2010, **22**, 1195–1202.

5 T. F. Otero and J. G. Martinez, *Electrochim. Acta*, 2012, **84**, 112–128.

6 N. Ayres, *Polym. Chem.*, 2010, **1**, 769–777.

7 Z. Xiang and D. Cao, *J. Mater. Chem. A*, 2013, **1**, 2691–2718.

8 P. M. Budd, B. S. Ghanem, S. Makhseed, N. B. Mckeown, K. J. Msayib and E. Tattershall, *Chem. Commun.*, 2004, **2**, 230–231.

9 N. B. McKeown and P. M. Budd, *Macromolecules*, 2010, **43**, 5163–5176.

10 N. B. Mckeown, B. Gahnem, K. J. Msayib, P. M. Budd, C. E. Tattershall, K. Mahmood, S. Tan, D. Book, H. W. Langmi and A. Walton, *Angew. Chemie*, 2006, **118**, 1836–1839.

11 S. V Adymkanov, Y. P. Yampol, A. M. Polyakov, P. M. Budd, K. J. Reynolds, N. B. Mckeown and K. J. Msayib, *Polym. Sci. Ser. A*, 2008, **50**, 444–450.

12 P. M. Budd, N. B. Mckeown, B. S. Ghanem, K. J. Msayib, D. Fritsch, L. Starannikova, N. Belov, O. Sanfirova, Y. Yampolskii and V. Shantarovich, *J. Membr. Sci. J.*, 2008, **325**, 851–860.

13 C. G. Bezzu, M. Carta, A. Tonkins, J. C. Jansen, P. Bernardo, F. Bazzarelli and N. B. Mckeown, *Adv. Mater.*, 2012, **24**, 5930–5933.

14 Y. Wang, N. B. Mckeown, K. J. Msayib, G. A. Turnbull, I. D. W. Samuel and O. S. Centre, *Sensors*, 2011, **11**, 2478–2487.

15 D. Buenger, F. Topuz and J. Groll, *Prog. Polym. Sci.*, 2012, **37**, 1678–1719.

16 A. Guiseppi-elie, *Biomaterials*, 2010, **31**, 2701–2716.

17 F. Xia, M. Pan, S. Mu, R. Malpass-Evans, M. Carta, N. B. McKeown, G. A. Attard, A. Brew, D. J. Morgan and F. Marken, *Electrochim. Acta*, 2014, **128**, 3–9.

18 M. Carta, R. Malpass-Evans, M. Croad, Y. Rogan, J. C. Jansen, P. Bernardo, F.

Bazzarelli and N. B. McKewon, *Science (80-.).*, 2013, **339**, 303–307.

19 G. Wang, X. He and L. Wang, *Microchim Acta*, 2013, **180**, 161–186.

20 Q. Liu, X. Xu, G. Ren and W. Wang, *Prog. Chem.*, 2006, **18**, 1530–1537.

21 Y. Li, Y. Song, C. Yang and X. Xia, *Electrochem. commun.*, 2007, **9**, 981–988.

22 Y. Zhou, S. Yang, Q. Qian and X. Xia, *Electrochem. commun.*, 2009, **11**, 216–219.

23 M. Pasta, F. La and Y. Cui, *Electrochem. commun.*, 2010, **12**, 1407–1410.

24 L. Rassaei and F. Marken, *Anal. Chem.*, 2010, **82**, 7063–7067.

25 A. Martins, V. Ferreira and A. Queir, *Electrochem. commun.*, 2003, **5**, 741–746.

26 A. Celebanska, A. Lesniewski, M. Paszewski, M. Jonsson-niedziolka, J. Niedziolka-jonsson and M. Opallo, *Electrochem. commun.*, 2011, **13**, 1170–1173.

27 H. Toit and M. Di Lorenzo, *Sensors Actuators B. Chem.*, 2014, **192**, 725–729.

28 Y. Chen, K. Flowers, M. Calizo and S. W. Bishnoi, *Colloides Surfaces B Biointerfaces*, 2010, **76**, 241–247.

Chapter 4: High Density Heterogenisation of Molecular Electrocatalysts in a Rigid Intrinsically Microporous Polymer Host

Chapter Abstract

A water-insoluble polymer with intrinsic microporosity (or PIM, here for the particular case of the Tröger's base system PIM-EA-TB, BET area ca. 10^3 m^2g^{-1}) is demonstrated to act as a rigid host environment for highly water-insoluble molecular catalysts, here tetraphenylporphyrinato-iron (FeTPP), surrounded by aqueous solution-filled micropores. A PIM-EA-TB film containing catalyst is deposited onto the electrode and immersed for voltammetry (i) with 4-(3-phenyl-propyl)-pyridine to give an organogel, or (ii) bare directly into aqueous solution. The porous host allows processes to be optimised as a function of solution phase, composition, and catalyst loading. Effective electron transfer as well as effective electrocatalysis is reported for aqueous oxygen and peroxide reduction. Given the use of completely water-insoluble catalyst systems, the methodology offers potential for application with a wide range of hitherto unexplored molecular electrocatalysts and catalyst combinations in aqueous media.

Graphical Abstract:

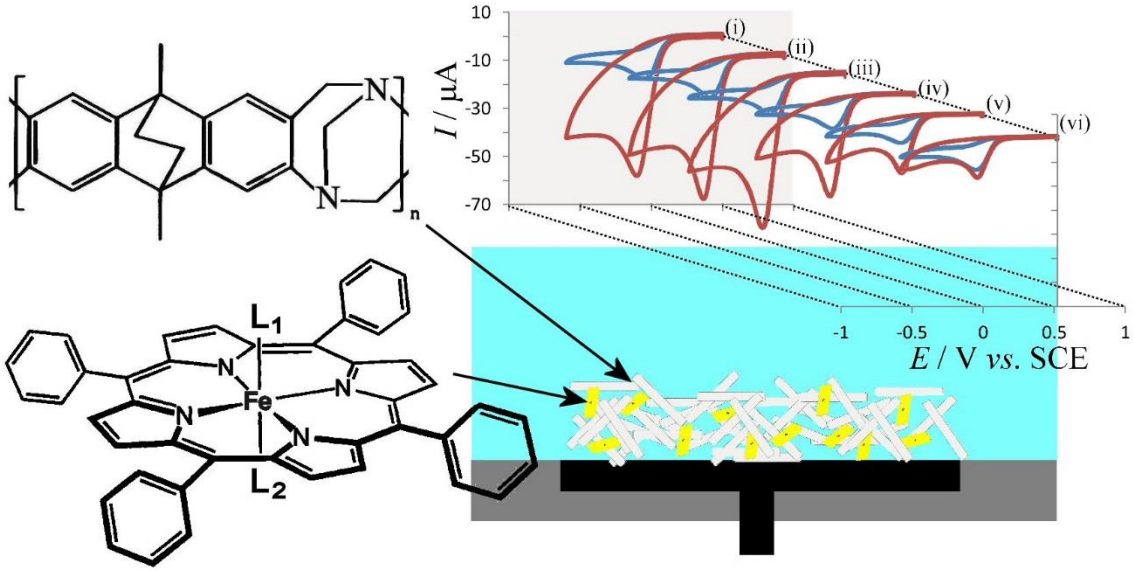

Chapter Publications

This chapter has been published in:

Y. Rong, R. Malpass-Evans, M. Carta, N. B. McKewon, G. A. Attard and F. Marken. *Electrochemistry Communications*, **2014**, 46, 26-29.

Acknowledgement

I would like to thank Dr. Richard. Malpass-Evans, Dr. Mariolino Carta, Prof. Gary Attard and Prof. Neil McKeown for the supply of PIM and helpful discussion.

4.1 Introduction

High density heterogenisation of molecular catalysts and/or catalyst systems is desirable (i) to exploit the benefits of assembled molecular catalysts at electrode surfaces, (ii) to avoid catalyst losses due to dissolution and separation, (iii) to enable "families" or "ensembles" of catalysts and co-catalysts to be assembled into active films, and (iv) to allow screening of catalyst activity as a function of solvent system, electrolyte, ionic strength, or pH. Most commonly applied are direct surface immobilisation strategies based on adsorption of catalysts[1,2], electrostatic attachment[3] or covalent attachment via carbon[4] or ethyny[5] bonds. These methods require suitable surfaces, high surface area, and carefully executed surface chemistry. An alternative strategy can be based on porous host materials such as conducting polymer[6], network polymers[7], zeolites[8], intercalation materials[9], sol-gels[10], which in turn need to be immobilised or pasted[11] into the electrode material. In particular gels and polymer hosts are beneficial and readily applied, although stability of these host materials, aging, cross-linking, and non-rigidity causing mobility of guest species can be problematic.

Recently, a novel family of highly rigid and therefore highly intrinsically microporous polymer (PIM) materials has been proposed[12,13]. In dry gas media these porous polymers allow gas separation[14] and gas storage[15]. When immersed in electrolyte media and in particular when carrying intrinsic charge (e.g. the poly-amine PIM-EA-TB when protonated, see Fig.4.1A[16]), these rigid and microporous polymer materials become desirable for applications in electrochemistry[17,18].

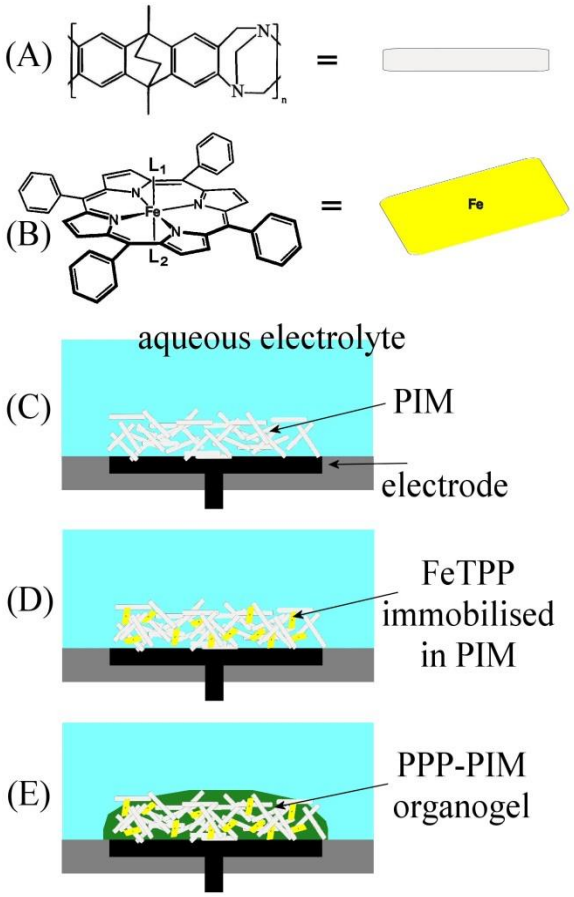

Figure 4.1. (A) Molecular structure of PIM-EA-TB. (B) Molecular structure of FeTPP. Also shown are schematic drawings of (C) PIM immobilised onto an electrode, (D) with FeTPP immobilised into the rigid microporous structure, and (E) with PPP to form a separate organic gel phase.

In this report, it is demonstrated that the microporous PIM-EA-TB offers an ideal rigid (suppressing Ostwald ripening by supressing surface diffusing) environment for molecular catalysts, such as the water-insoluble model system FeTPP (see Fig.4.1B). Fig.4.1D represents a schematic depiction of the case of molecular FeTPP catalyst randomly distributed within the rigid host and surrounded by aqueous electrolyte. Figure 4.1E depicts the case of a water-immiscible organic solvent, here 4-(3-phenyl-propyl)-pyridine or PPP[19], co-deposited into the porous PIM-EA-TB host to give an organogel, which is used here to characterise the chemically reversible one-electron transformation Fe(II/III)TPP (with coordination of PPP in L1 and L2 position, Fig.4.1B) coupled to anion transfer from the aqueous phase. The aqueous system (Fig.4.1D) is demonstrated for the electrocatalytic reduction of oxygen and of hydrogen peroxide.

4.2 Experimental

4.2.1 Chemical Reagents

4-(3-phenylpropyl)-pyridine (Aldrich, 97%), 5,10,15,20-tetraphenyl-21H,23H-porphine iron(III) chloride (FeTPPCl, Aldrich), phosphoric acid (Fischer Scientific, 85%wt), sodium hydroxide (Aldrich, >97%), dimethylformamide (Aldrich, HPLC grade, >99.9%), NaClO4, NaPF6, NaNO3 (Aldrich), hydrogen peroxide (Acros Organics, 35%wt) were used as received. PIM-EA-TB was prepared following a literature recipe[16]. Solutions were prepared with filtered and deionized water of resistivity 18.2 MΩ cm from a Thermo Scientific water purification system.

4.2.2 Instrumentation

A potentiostat system (IVIUM Compactstat) was employed with a Pt wire counter electrode and a KCl-saturated calomel reference (SCE, Radiometer, Denmark). The working electrode was a glassy carbon electrode (3 mm diameter, BAS). The UV/Vis experiments were performed with a Varian UV-Visible spectrophotometer. All experiments were conducted at a temperature of 293 ± 2K.

4.2.3 Procedures for Electrode Preparation

Solution A of PIM-EA-TB (1 mg cm^{-3}) in dimethylformamide (DMF) acidified with 5 μL $HClO_4$ was prepared. Solution B of FeTPPCl (1 mg cm^{-3}) in DMF solution was prepared. Then solution A and B were mixed and 1 μL deposited onto the glassy carbon electrode surface with solvent evaporation at 90 ^oC in an oven. A free-standing membrane 1:1 FeTPPCl:PIM was prepared by solution evaporation in a Teflon mould (see Fig.4.2B). Films deposited onto glass slides were characterised by UV/Vis (Fig. 4. 2A) and the characteristic Soret band at 414 nm[20] is observed.

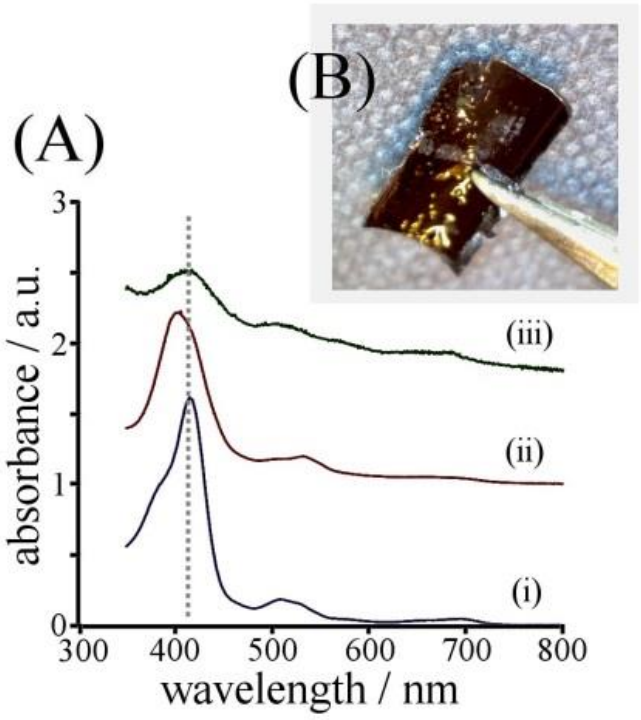

Figure 4. 2. (A) UV/Vis spectra for (i) 0.1 mg cm^{-3} FeTPPCl in DMF, (ii) a film of 1:5 FeTPPCl:PIM, and (iii) a film of 5:1 FeTPPCl:PIM (ii and iii are offset for clarity). (B) Photograph of a free-standing PIM-TeTPP membrane.

4.3 Results and Discussion

4.3.1 PIM-Catalyst Films I.: Voltammetry of FeTPP in Organogel Environments

In order to investigate the immobilised FeTPP redox system initially the organic solvent 4-(3-phenyl-propyl)-pyridine or PPP is applied to the FeTPP-PIM film to give a water-immiscible organogel film (see Fig. 4.3A). The liquid-liquid interface are established between organogel and liquid interface. The electron transfer at the electrode surface is coupled to ion transfer at liquid-liquid interface. The axial positions L_1 and L_2 (see Fig.4.1B) are likely to be occupied by the pyridine-derivative solvent giving chemically reversible one-electron character to the Fe(III/II)TPP redox system[21] (equation 4.1).

$$Fe(III)TPP^{+}(org) + A^{-}(org) + e^{-} \rightleftharpoons Fe(II)TPP(org) + A^{-}(aq) \qquad (4.1)$$

The anion A^-(aq) here is the perchlorate anion, which is transferred between organic and aqueous phase with a midpoint potential of 0.145 V vs. SCE consistent with literature reports. By varying the type of anion from PF_6^- to ClO_4^- to NO_3^- a characteristic sequence of midpoint potentials is observed (Fig.4.3Biv-vi) due to the variation in anion transfer potential[21].

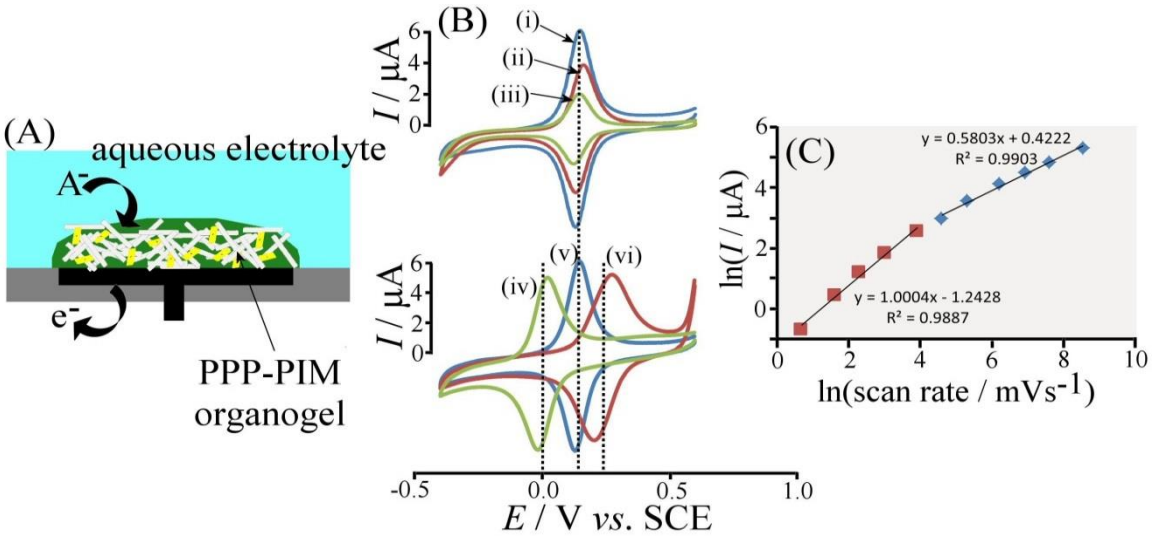

Figure 4. 3. (A) Schematic drawing of the liquid|liquid anion transfer process coupled to the $FeTPP^{+/0}$ redox process at the electrode surface. (B) Cyclic voltammograms (scan rate 20 mVs^{-1}) for the oxidation of FeTPP immobilised into PIM and coated with PPP (to give an organogel phase separate from the aqueous phase) immersed in 0.1 M phosphate buffer pH 7 with 0.1 M $NaClO_4$ for FeTPP:PIM weight ratios (i) 1:1, (ii) 1:5, (iii) 1:20. Also shown are data for 1:1 FeTPP:PIM immersed in phosphate buffer with (iv) 0.1 M $NaPF_6$, (v) 0.1 M $NaClO_4$, and (vi) $NaNO_3$. (C) Plot (double logarithmic) of the peak current for the oxidation of FeTPP:PIM 1:1 in phosphate buffer with 0.1 M $NaClO_4$ as a function of scan rate.

When varying the FeTPP:PIM film composition from 1:1 to 1:5 to 1:20 (by weight) the peak current for both oxidation and back-reduction changes accordingly (Fig.4.3Bi-iii). The effect of scan rate is investigated for FeTPP:PIM 1:1 as shown in Figure 4.3C. At lower scan rates up to ca. 50 mVs^{-1}, an approximately linear increase in peak current with scan rate is indicative of a nearly complete electrolysis of the FeTPP contained in the film (thin film case, the charge under the peak, ca. 30µC, is consistent with the amount of deposit). At higher scan rates approximately square root dependence of peak current versus scan rate is indicative of diffusion (thick film case). Overall, an active organogel film containing FeTPP-PIM surrounded by solvent is demonstrated. In these films FeTPP is not catalytically active due to axial pyridine ligands. Next, the electrocatalytic characteristics in purely aqueous media without organic phase are investigated. Under this condition, there is no voltammetry response for the catalysts FeTPP itself.

4.3.2 PIM-Catalyst Films II.: Voltammetry of FeTPP in Aqueous Environments

The molecular catalyst FeTPP and derivatives thereof have biomimetic significance and have been employed previously in oxidation chemistry as well as in the electrocatalytic reduction of O_2 and CO_2[22]. When immobilised in the form of the FeTPP-PIM film and immersed into aqueous 0.1 M phosphate buffer pH 2, there is no direct electrochemical response to be attributed to the FeTPP catalyst. However, the catalytic reduction of oxygen (ca. 0.18 mM ambient concentration[23]) is readily detected at -0.044 V vs. SCE with a peak current of -17 μA (see Fig.4.4B). In contrast, at bare glassy carbon or PIM-EA-TB coated glassy carbon, this reduction peak is shifted more negative by ca. 0.4 V (not shown). The peak current in the presence of catalyst can be compared to the value estimated by the Randles-Sevcik equation[24] (equation 4.2).

$$I_{peak} = 2.69 \times 10^5 n^{3/2} A D^{1/2} c v^{1/2} \approx 16\ \mu A \qquad (4.2)$$

In this equation the diffusion controlled peak current I_{peak} is expressed in terms of n, the number of electrons transferred per molecule diffusing to the electrode surface, $A = 7.1 \times 10^{-6}$ m^2, the geometric electrode area, $D = 1.65 \times 10^{-9}$ m^{2}s^{-1}, the diffusion coefficient for oxygen, $c = 0.18$ mM, the ambient concentration of oxygen, and v, the scan rate. The agreement is good and a four-electron reduction appears likely. When adding H_2O_2 into the solution to give a 4 mM concentration, the cathodic current increases accordingly (Fig.4.4Bi), consistent with catalytic reduction of H_2O_2 to water at the potential of oxygen reduction.

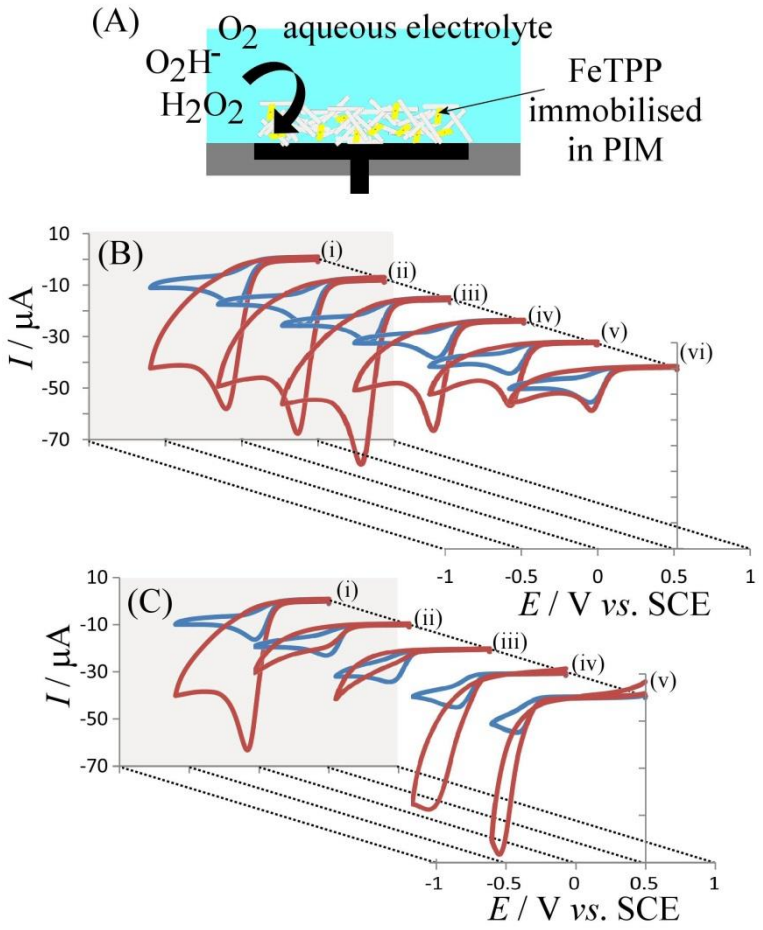

Figure 4. 4. (A) Schematic drawing of the FeTPP-PIM film coated electrode immersed in aqueous electrolyte. (B) Cyclic voltammograms (scan rate 20 mVs^{-1}) for the reduction of ambient oxygen (blue) and 4 mM H_2O_2 (red) at electrodes coated with (i) 1:1, (ii) 1:2, (iii) 1:5, (iv) 1:10, (v) 1:20, and (vi) 1:40 weight ratio FeTPP:PIM immersed in aqueous 0.1 M phosphate buffer pH 2. (C) Cyclic voltammograms (scan rate 20 mVs^{-1}) for the reduction of ambient oxygen (blue) and 4 mM H_2O_2 (red) at electrodes coated with 1:5 FeTPP:PIM immersed in aqueous 0.1 M phosphate buffer at pH (i) 2, (ii) 4, (iii) 7, (iv) 9, and (v) 12.

When changing the FeTPP:PIM ratio, the cathodic response for the reduction of oxygen remains approximately constant (with a decrease in peak current to ca. 10 µA), however, the reduction of H_2O_2 is substantially suppressed at ca. 1:10 weight ratio. Therefore, a high concentration of FeTPP in PIM is necessary for the reduction of H_2O_2 to water, but not for the reduction of oxygen to H_2O_2, indicative of two mechanisms.

When changing the pH of the solution, significant changes in catalytic activity are observed (see Fig.4.4C for FeTPP:PIM 1:5). For the oxygen reduction only a shift in peak potential (ca. 40 mV per pH unit) is observed with the peak current remaining approximately constant (i.e. the electrocatalytic reduction remains a four-electron process). However, the reduction of H_2O_2

is suppressed at pH 4 and pH 7 and then re-emerges at pH 9. These changes are likely to be linked to (i) the presence of reaction intermediates, (ii) the inter-catalyst site distance, (iii) disproportionation/dismutation processes, as well as (iv) charge transport within the film and require further study.

4.4 Conclusion

It has been shown that a highly water-insoluble molecular electrocatalyst, FeTPPCl, is readily immobilised in a rigid microporous PIM-EA-TB polymer film. Electrochemical activity is demonstrated in the presence of an organic solvent (with PPP as water-insoluble organic phase liquid-liquid anion transfer coupled to electron transfer is observed) and electrocatalytic activity is demonstrated in aqueous electrolyte media. Four-electron reduction of oxygen and two-electron reduction of hydrogen peroxide occur at a similar potential with both (i) the density of electrocatalyst in the polymer matrix and (ii) the pH playing a crucial role in making the catalytic reaction effective.

In future, a broader range of PIM-hosts for electrocatalysts could be developed specifically for application in sensing and/or in fuel cell catalysis. High density co-immobilisation of several catalysts and co-catalysts in layers or nano-structures (mimicking bio-films) will allow reactions to be controlled and/or coupled effectively.

4.5 References

1 C. Kang, Y. Xie and F. C. Anson, *J. Electroanal. Chem.*, 1996, **413**, 165–174.

2 T. Schilling, A. Okunola, J. Masa, W. Schuhmann and M. Bron, *Electrochim. Acta*, 2010, **55**, 7597–7602.

3 M. Huang, Y. Shao, X. Sun, H. Chen, B. Liu and S. Dong, *Langmuir*, 2005, **21**, 323–329.

4 J. D. Watkins, K. Lawrence, J. E. Taylor, T. D. James, S. D. Bull and F. Marken, *Electroanalysis*, 2011, **23**, 1320–1324.

5 M. V. Sheridan, K. Lam and W. E. Geiger, *Angew. Chemie - Int. Ed.*, 2013, **52**, 12897–12900.

6 F. BEDIOUI, M. VOISIN, J. DEVYNCK and C. BIED-CHARRETON, *J. Electroanal. Chem. interfacial Electrochem.*, 1991, **297**, 257–269.

7 N. Chikushi, E. Ohara, A. Hisama and H. Nishide, *Macromol. Rapid Commun.*, 2014, **35**, 976–980.

8 F. C. Skrobot, I. L. V Rosa, A. P. A. Marques, P. R. Martins, J. Rocha, A. A. Valente and Y. Iamamoto, *J. Mol. Catal. A Chem.*, 2005, **237**, 86–92.

9 S. Nakagaki, K. A. D. F. Castro, G. S. Machado, M. Halma, S. M. Drechsel and F. Wypych, *J. Braz. Chem. Soc.*, 2006, **17**, 1672–1678.

10 A. T. Papacídero, L. A. Rocha, B. L. Caetano, E. Molina, H. C. Sacco, E. J. Nassar, Y. Martinelli, C. Mello, S. Nakagaki and K. J. Ciuffi, *Colloids Surfaces A Physicochem. Eng. Asp.*, 2006, **275**, 27–35.

11 T. Skeika, C. Marcovicz, S. Nakagaki, S. T. Fujiwara, K. Wohnrath, N. Nagata and C. a Pessoa, *Electroanalysis*, 2007, **19**, 2543–2550.

12 Z. Xiang and D. Cao, *J. Mater. Chem. A*, 2013, 2691–2718.

13 P. M. Budd, B. S. Ghanem, S. Makhseed, N. B. McKeown, K. J. Msayib and C. E. Tattershall, *Chem. Commun.*, 2004, 230–231.

14 S. V Adymkanov, Y. P. Yampol, A. M. Polyakov, P. M. Budd, K. J. Reynolds, N. B. Mckeown and K. J. Msayib, *Polym. Sci. A*, 2008, **50**, 444–450.

15 N. B. McKeown and P. M. Budd, *Macromolecules*, 2010, **43**, 5163–5176.

16 M. Carta, R. Malpass-Evans, M. Croad, Y. Rogan, J. C. Jansen, P. Bernardo, F. Bazzarelli and N. B. McKeown, *Science (80-.).*, 2013, **339**, 303–307.

17 F. Xia, M. Pan, S. Mu, R. Malpass-Evans, M. Carta, N. B. McKeown, G. A. Attard, A. Brew, D. J. Morgan and F. Marken, *Electrochim. Acta*, 2014, **128**, 3–9.

18 Y. Rong, R. Malpass-Evans, M. Carta, N. B. Mckeown, G. A. Attard and F. Marken, *Electroanalysis*, 2014, **26**, 904–909.

19 F. Marken, K. J. McKenzie, G. Shul and M. Opallo, *Faraday Discuss*, 2005, **129**, 219–229.

20 C. De Silva, K. Czarnecki and M. D. Ryan, *Inorganica Chim. Acta*, 1999, **287**, 21–26.

21 M. J. Bonne, C. Reynolds, S. Yates, G. Shul, J. Niedziolka, M. Opallo and F. Marken, *New J. Chem.*, 2006, **30**, 327–334.

22 C. Costentin, M. Robert and J.-M. Savéant, *Chem. Soc. Rev.*, 2013, **42**, 2423–2436.

23 L. Nei, *J. Electrochem. Soc.*, 1997, **144**, 3019–3026.

24 A. J. Bard and L. R. Faulkner, *Electrochemical Methods: Fundamentals and Applications*, Wiley, New York, 2nd edn., 2001.

Chapter 5: Polymers of Intrinsic Microporosity in Electrochemistry: Anion Uptake and Transport Effects in Thin Film Electrodes and in Free-Standing Ionic Diode Membranes

Chapter Abstract

Anion uptake and charge transport in a Polymer of Intrinsic Microporosity (here PIM-EA-TB) is investigated for three cases: (i) the oxidation of ferrocene embedded into a thin film of PIM-EA-TB on a glassy carbon electrode, (ii) the reduction of protons absorbed into a thin film of PIM-EA-TB on a platinum electrode, and (iii) the potential-driven transport of anions and protons in an asymmetrically deposited free-standing PIM-EA-TB membrane working as a current rectifier or "ionic diode". In all three cases the competing effects of the diameter and hydrophobicity (size and hydration energy) of the anion are important. For free-standing membranes very high ionic diode rectification ratios (>10^3 at +/-1 V) are observed in particular for thicker deposits of PIM-EA-TB and for chloride or perchlorate containing electrolyte.

Graphical Abstract:

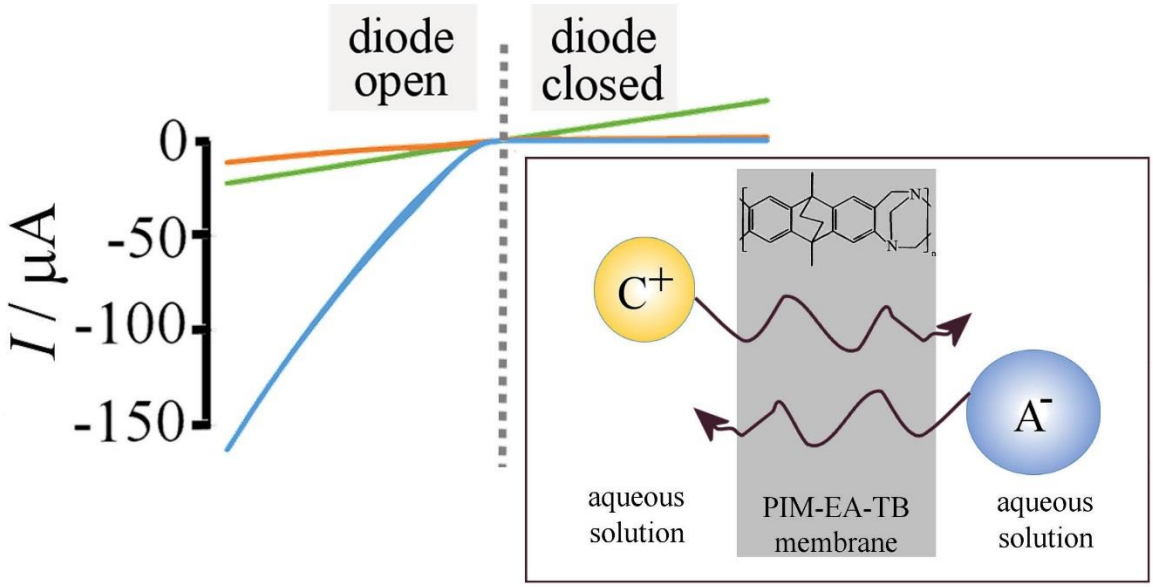

Chapter Publications

This chapter has been published in:

Y. Rong, A. Kolodziej, E. Madrid, M. Carta, R. Malpass-Evans, N. B. McKewon and F. Marken. *Journal of Electroanalytical Chemistry*, **2015**, 26, 904-909.

Acknowledgement

I would like to thank the Adam Kolodziej for his contribution on oxidation of ferrocene in PIM and Elena Madrid for her help with four-electrode experiments with PIM film.

5.1 Introduction

Novel porous materials and membranes are constantly introduced into applications in electrochemistry due to the rapidly progressing research in the field of microporous materials[1–3]. The development of Polymers of Intrinsic Microporosity (PIMs) has resulted in significant interest particularly over last three years due to features combining microporosity with chemical stability and processability[4]. In general, the class of structure-tuneable PIM molecules is characterized by very high specific surface area (reaching over 1000 m^2g^{-1})[5], a rigid molecular structure, permanent porosity, and size-dependent permeability for example for gas separation applications[6]. PIMs have been proposed for gas management systems with a particular attention to storage[7] and separation[8]. PIMs have also been employed as high temperature templates for metal oxide nanostructures[9].

More recently, microporous PIM materials have been introduced directly to electrochemistry, where potential applications range from novel approaches to catalyst heterogenisation[10], fuel cell catalyst stabilisation[11], switchable membranes[12], and water desalination[13]. In our previous articles, we have reported in particular the use of a PIM material obtained in a Tröger's base (TB) polymerization of diaminoethanoanthracene (EA), PIM-EA-TB (see molecular structure indicated in Fig.5.1, average molecular weight ca. 70kDa, BET surface area >1000 $m^2\ g^{-1}$), as a host for tetraphenylporphyrinato-iron metal complexes[10], as a protective layer for gold nanoparticles during glucose oxidation[14], and as a host for immobilising TEMPO-electrocatalysts onto electrode surfaces for the heterogeneous electro-oxidation of carbohydrates[15] and primary alcohols[16]. PIM-EA-TB membranes contain tertiary amine sites and may be regarded as mixed cation/anion conductors. When deposited into micropores, PIM-EA-TB has been shown to act as current rectifier or "ionic diode"[12,13]. A more in-depth understanding of processes in PIM-EA-TB membranes is desirable in order to further broaden the range of applications in electrochemistry and to widen the scientific scope. This report focuses on the interaction of different types of anions with PIM-EA-TB and in particular the selectivity towards perchlorate.

The perchlorate anion is a pollutant[17] and a strong oxidant produced in large amounts by industrial companies all over the world. As an extremely mobile ion, it may easily travel within surface waters and reservoirs with a very slow rate of degradation. Water contaminated with

perchlorate is deemed harmful and new methods for electroanalytical detection have been proposed[18]. However long-term effects are not fully understood. Having the same ionic radius as iodine anions results in an inhibition of iodine uptake into thyroid (perchlorate competes with iodide intake), and therefore decreased release of thyroid hormones into the human body. Phyto-mediated removal of perchlorate has been proposed[19]. Similar effects have been observed also in bodies of fishes and rats left in the presence of this contaminant. Here, it is shown that perchlorate can interact with PIM-EA-TB membranes preferentially when compared to other more hydrophilic anions.

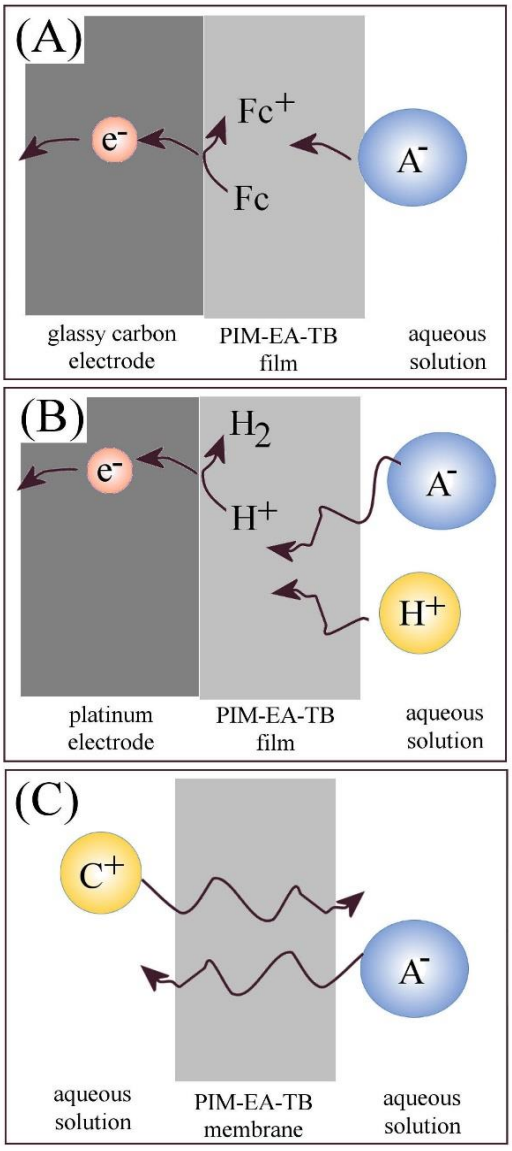

Figure 5.1. Schematic drawing of (A) a film of PIM-EA-TB with ferrocene embedded as redox active component, (B) a film of PIM-EA-TB with protons as redox active component, and (C) a free-standing membrane of PIM-EA-TB with cation and anion transport resulting in ionic diode characteristics.

We present an investigation of the effects of anions, in particular perchlorate, on the reactivity of PIM-EA-TB for three types of processes (Fig.5.1). PIM-EA-TB (see molecular structure in Fig.5.2) has the ability to act as poly-cation when protonated, which allows anion transport through micropores. However, little is known about the mobility of anions and of protons and the link between charge transport and state of protonation and hydration. Protonation of the PIM-EA-TB membrane introduces both anions and protons (due to electro-neutrality). Therefore the mobility of both anions and protons should depend on the state of protonation as well as on effects of hydration.

In the first part of this report the oxidation of ferrocene (as a model redox system, Fig.5.1A) immobilised into a PIM-EA-TB film and immersed into aqueous electrolyte solution is investigated. The ferrocene - ferricenium redox system is successfully contained by PIM-EA-TB at the electrode surface and the role of perchlorate and tetrafluoroborate in enhancing the current responses is demonstrated. Then, the protonation of the PIM-EA-TB film (Fig.5.1B) is investigated directly by reduction of protons at platinum to molecular hydrogen. Perchlorate is shown to enhance protonation, although only a very small fraction of protons can be reduced at the electrode surface to molecular hydrogen. The question of coupled proton/anion mobility in the PIM-EA-TB film is raised. Finally, in preliminary and exploratory experiments films of PIM-EA-TB immobilised in a 20 μm diameter pore are shown to give rise to strong "ionic diode" phenomena and current responses which are strongly anion dependent. Chloride and perchlorate are proposed to act as "catalyst" for proton conduction to explain very high current rectification effects.

5.2 Experimental

5.2.1 Chemical Reagents

Sodium phosphate dibasic heptahydrate, sodium tetrafluoroborate, sodium chloride, sodium sulphate decahydrate, sodium perchlorate, potassium perchlorate, lithium perchlorate, ferrocene, eosin Y, agarose, phosphoric acid, formic acid, perchloric acid, hydrochloric acid, and chloroform were purchased from Sigma Aldrich or Fluka and used as received. PIM-EA-TB was synthesized according to the literature recipe[20]. Aqueous solutions were prepared with

filtered and deionized water of resistivity 18 MΩ cm (at 20 ºC) from a Thermo Scientific water purification system.

5.2.2 Instrumentation

A potentiostat system (Metrohm micro-Autolab II) was employed with a conventional three-electrode cell configuration: a Pt wire as a counter electrode and a KCl-saturated calomel electrode (SCE, Radiometer, Copenhagen) as a reference. A glassy carbon electrode with a diameter of 3 mm was used as a working electrode for ferrocene oxidation experiments. A 1.6 mm diameter platinum electrode was employed for protonation experiments. For membrane experiments an Ivium Compactstat system in 4-electrode configuration was employed (counter/reference in one half cell and working/sense in the opposite half-cell, see Figure 2A). All experiments were conducted at a temperature of 293 ± 2 K.

5.2.3 Procedures

For film voltammetry, a solution of ferrocene was prepared by dissolving 5 mg in 1 cm^3 of chloroform to give a ca. 27 mM solution. A solution of PIM-EA-TB (MW ca. 70 kDa) was prepared by dissolving 5 mg of the polymer in 1 cm^3 of chloroform. One volume of ferrocene solution and an appropriate volume of PIM-EA-TB solution were mixed for deposition and stored in the dark at 4 °C. An appropriate amount of ferrocene with PIM-EA-TB polymer (typically 5 μL) was pipetted directly on the surface of the 3 mm diameter glassy carbon electrode and the deposit dried in air flow under a fume hood. For PIM-EA-TB protonation experiments a solution of 1 mg PIM-EA-TB in 1 cm^3 chloroform was used. A 5 μL volume was deposited onto a 1.6 mm diameter platinum electrode. After evaporation of the chloroform the electrode was immersed into buffer solution.

For experiments with PIM-EA-TB membrane, a poly-(ethylene-terephthalate) (PET) film (6 μm thick with a 20 μm pore laser drilled into the centre[12], see Fig.5.2) was first placed onto 1% agarose gel (to block one surface) and then a solution PIM-EA-TB in chloroform was applied. The solvent was allowed to air-dry and the PET is then lifted off the agarose gel to give asymmetric "one-sided" deposits. Fluorescence imaging of the PIM-EA-TB deposit (soaked in

the 1 mM fluorescent dye eosin Y in ethanol for 12 h) shows that one side of the PET film (left) is coated with an approximately 10 μm thick film whereas the other side of the membrane (right) has a small area with only the 20 μm diameter pore exposed to the solution phase. Membrane voltammetry was performed in four-electrode configuration (Fig.5.2A) with counter/reference and working/sense immersed in opposite sides of the electrochemical cell. The side of the membrane with the PIM-EA-TB deposit is placed facing the working electrode.

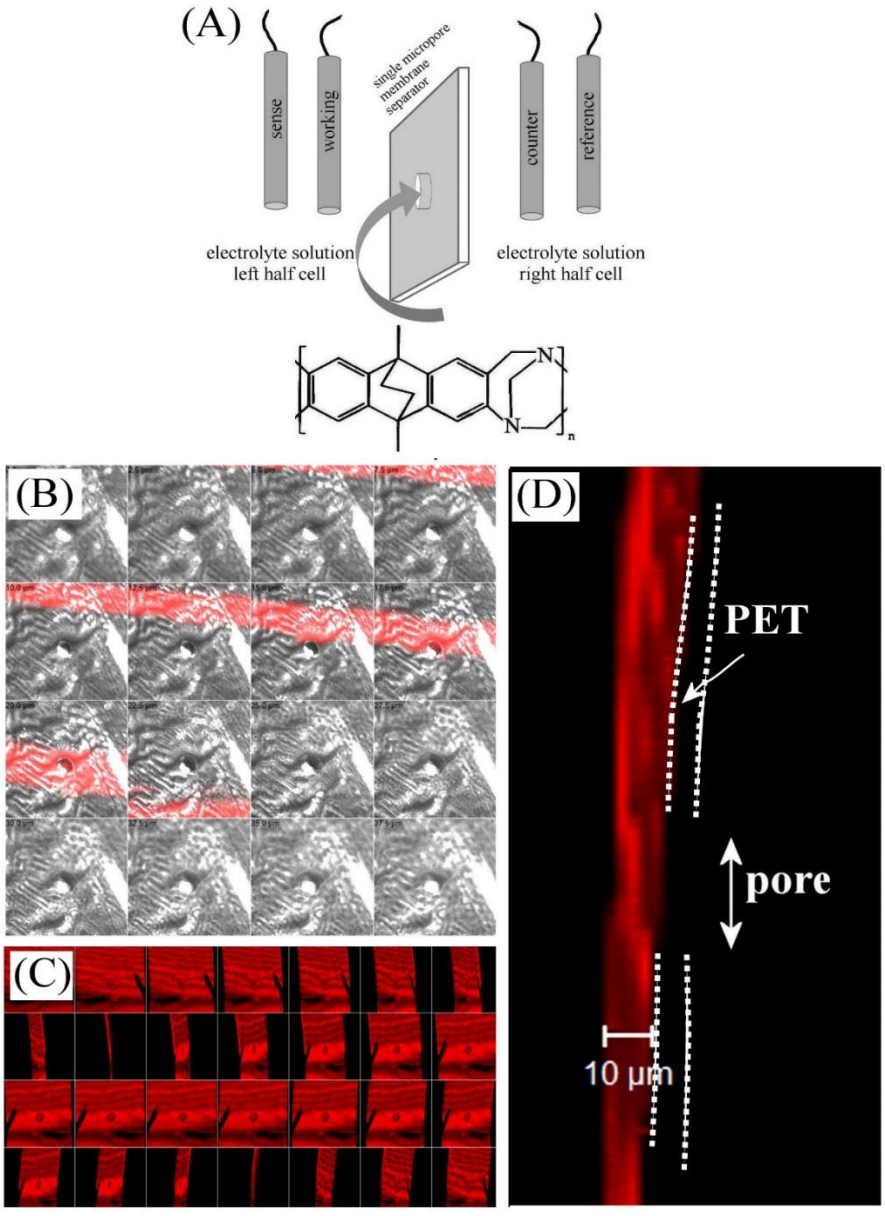

Fig 5.2. (A) Schematic drawing of the experimental four-electrode configuration with PIM-EA-TB deposited into a 20 μm diameter pore in PET. (B) Layered fluorescence microscopy images, (C) z-stack images, and (D) the reconstructed cross section (side view) showing the PIM-EA-TB with eosin Y adsorbed in the pore region. The underlying PET film is indicated but invisible under these conditions.

5.3 Results and Discussion

5.3.1 Anion Effects on the Oxidation of Ferrocene Embedded in PIM-EA-TB

Ferrocene is a well-known one-electron redox species widely studied in organic solvents[21], but also recognised to be electrochemically active in aqueous electrolyte media[22]. The ferrocene molecule is known to be reversibly oxidized and reduced for example at a glassy carbon electrode (equation 5.1).

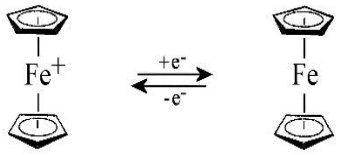

(5.1)

Ferrocene itself is only poorly soluble in aqueous media. However, when oxidized to the ferricenium cation, it becomes slightly more soluble and a part of the solid deposit leaves the electrode surface via diffusion into the solution phase[22]. Figure 5.3A shows data from voltammetry experiments with pure solid ferrocene deposited onto a glassy carbon electrode and immersed into 0.1 M $NaClO_4$ solution. After 10 consecutive potential cycles a clear loss of redox active material is observed. However, when co-deposited with PIM-EA-TB as a rigid host, the loss can be suppressed. Data in Figure 5.3B-5.3D demonstrate that with a decreasing content of ferrocene in the polymer host film, the voltammetric responses stabilise. For 17 wt% ferrocene in PIM-EA-TB (or a 1:5 weight ratio) the voltammetric response appears completely stable so that further investigations are possible. The PIM-EA-TB host material has to be seen here as a highly rigid framework that allows ferrocene to be retained even when switching the redox state and when anion (here perchlorate) uptake and expulsion occurs in conjunction with the ferrocene oxidation and back-reduction.

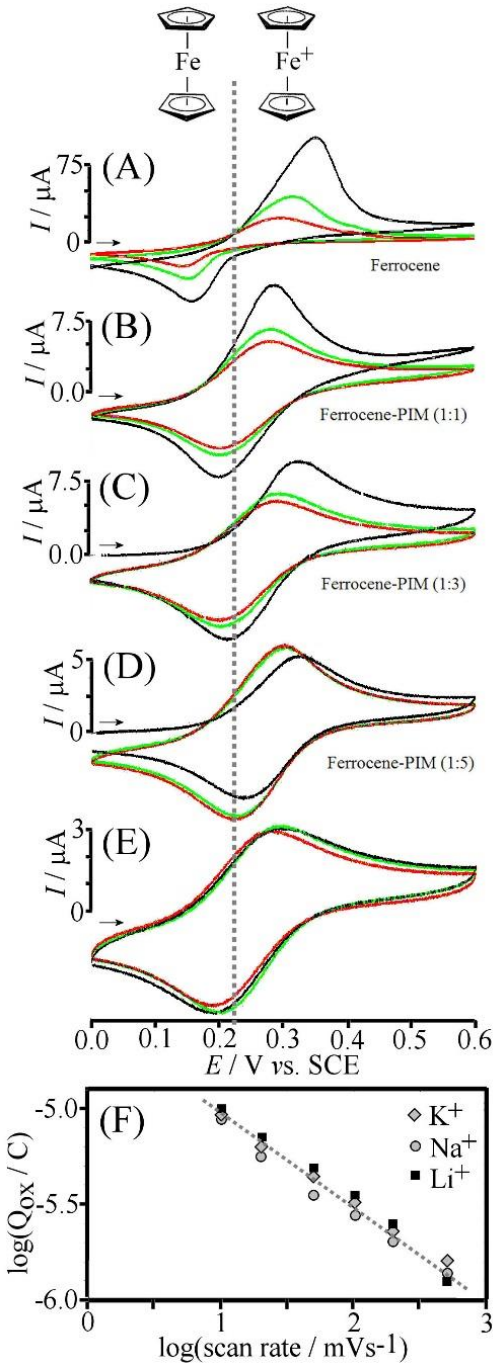

Figure 5.3. Cyclic voltammograms (scan rate 100 mVs^{-1}) for the oxidation of a deposit of (A) ferrocene, (B) ferrocene-PIM-EA-TB 1:1, (C) 1:3, (D) 1:5 (black curve 1st cycle, green curve 5th cycle, red curve 10th cycle) at a 3 mm diameter glassy carbon electrode immersed in aqueous 0.1 M $NaClO_4$. (E) As in D, but comparing black 0.1 M $KClO_4$, green 0.1 M $LiClO_4$, red 0.1 M $NaClO_4$. (F) Plot (double logarithmic) of the charge under the oxidation peak (comparing K^+, Na^+, Li^+) versus scan rate with a dotted line indicating slope –½.

In order to investigate the effect of electrolyte cation during oxidation and back-reduction of ferrocene immobilized in PIM-EA-TB, aqueous solutions of lithium, sodium and potassium salts of perchloric acid have been used as electrolyte. Figure 5.3E shows that there is no

particular discernible difference between all cations used. Therefore only anion uptake and expulsion in the PIM-EA-TB film appears to be important. Repeat experiments at a range of potential scan rates were performed and a double-logarithmic plot of peak charge versus scan rate reveals a -1/2 slope consistent with diffusion control (Figure 5.3F) for all three cations. Therefore, it is likely that in this case the rate limiting diffusion process is that of the perchlorate anions through the PIM-EA-TB - ferrocene composite films (*vide infra*).

The investigation of the effect of the electrolyte anion was carried out using 0.1 M sodium salts of perchlorate, tetrafluoroborate, chloride, phosphate, sulfate and tetraphenylborate (Figure 5.4). With ferrocene - PIM-EA-TB (1:5) immobilised at the glassy carbon electrode well-defined voltammetric responses were obtained for $NaClO_4$ and for $NaBF_4$ (Figure 5.4A and 5.4B, respectively). Peak-to-peak separation values for ClO_4^- and for BF_4^- anions are below $\Delta E_p \approx 100$ mV (at a scan rate of 100 mVs^{-1}) indicative of close to reversible conditions. Peak currents suggest diffusion rates for BF_4^- even higher compared to those for ClO_4^-. Perhaps surprisingly, for other types of anions the behaviour becomes much more complicated. When NaCl (Figure 5.4C) is employed as electrolyte, peak responses can still be observed, however their shape is distorted in particular for the anodic reaction. In aqueous electrolyte media containing Na_2HPO_4 (Figure 5.4D) and Na_2SO_4 (Figure 5.4E) only weak and ill-defined oxidation and back-reduction peaks are observed. Data in Figure 5.4F is for the oxidation of ferrocene - PIM-EA-TB in the presence of tetraphenylborate anions. Only very weak responses are observed indicative of suppressed redox activity most likely due to tetraphenylborate anions being too bulky to diffuse into the microporous PIM-EA-TB host framework with pore sizes typically 1-2 nm[12]. A shift of the midpoint potential (here defined as $E_{mid} = ½ E_{p,ox} + ½ E_{p,red}$) in sequence $ClO_4^- < BF_4^- < Cl^-$ can be interpreted in terms of the more hydrophilic chloride requiring a higher transfer potential to enter the more "organic" environment in the PIM-EA-TB framework. However, peak responses for phosphate and for sulfate appear to deviate from this trend based on hydrophobicity (or more correctly on anion hydration energies), indicating that the role of hydration in these reactions is more complex compared to, for example, the simple case of anion transfer across a liquid|liquid phase boundary[23]. Some part of the hydration shell may be retained by the anions, in particular for strongly hydrated anions.

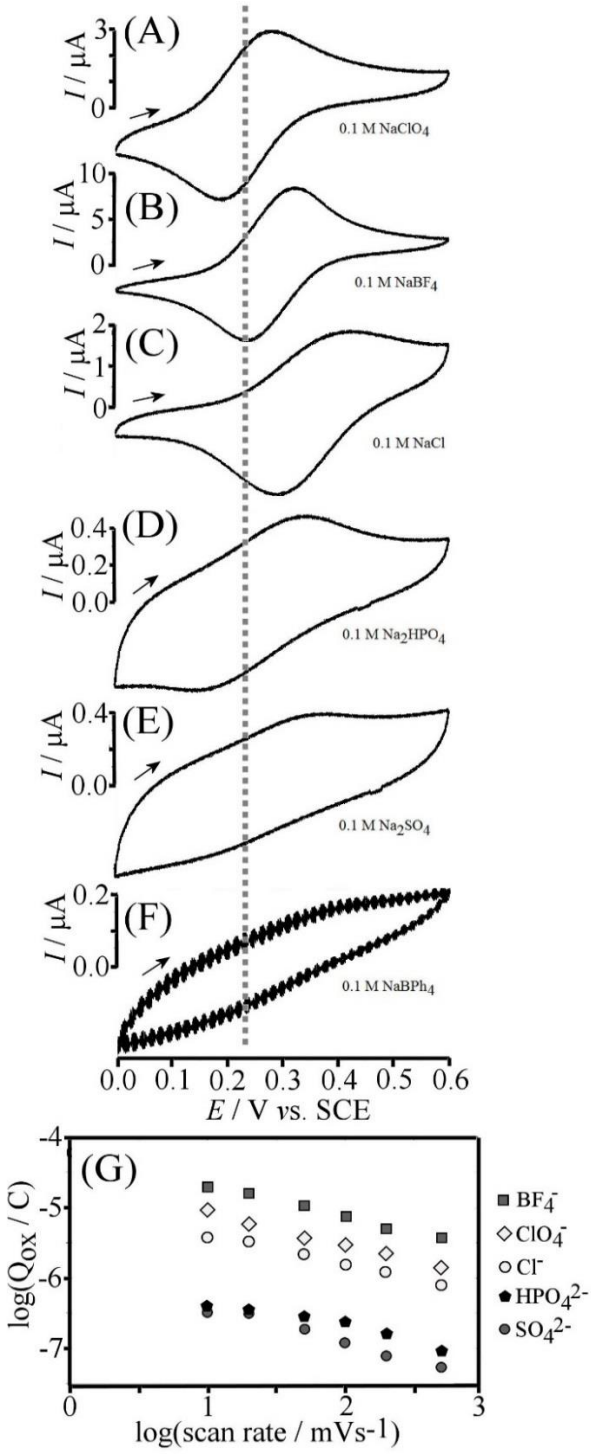

Figure 5.4. Cyclic voltammograms (scan rate 100 mVs^{-1}) for 1:5 ferrocene – PIM-EA-TB deposited on a glassy carbon electrode and immersed in (A) 0.1 M $NaClO_4$, (b) 0.1 M $NaBF_4$, (C) 0.1 M NaCl, (D) 0.1 M Na_2HPO_4, (E) 0.1 M Na_2SO_4, and (D) 0.1 M $NaBPh_4$. (G) Double logarithmic plot of the charge under the oxidation peak versus scan rate for the different anions.

It appears that the PIM-EA-TB membrane is selective towards certain hydrophobic (and not too big) anions, in particular BF_4^- and perchlorate, giving significantly higher current responses. To further investigate this effect, ferrocene - PIM-EA-TB (1:5) immobilised at a glassy carbon electrode was immersed initially in 0.1 M Na_2HPO_4. Cyclic voltammograms were obtained (see Fig.5.5D) showing very low redox peak signals. Then, appropriate amounts of $NaClO_4$ were added and cyclic voltammograms were recorded as a function of perchlorate concentration. An increase in oxidation and back-reduction peaks suggest that the ferrocene - PIM-EA-TB membrane may be affected by perchlorate anions even at the level of nano-molar concentration (Fig.5.5E). At this low level, traces of perchlorate are likely to carry over into other experiments to cause contamination or "memory" effects. Figure 5.5A shows ferrocene – PIM-EA-Tb (1:5) co-deposited and immersed in 0.1 M $NaClO_4$. Voltammograms were obtained with scan rate 100 mVs^{-1} giving well-developed redox peaks (Fig.5.5A). Subsequently, the electrode was transferred into 0.1 M solution of Na_2HPO_4 and studied at the same scan rate. The change of the electrolyte results in continuing decrease of current peak values for the reversible oxidation of ferrocene linked to only gradual loss of perchlorate. The process is reversed when the electrode is immersed back into 0.1 M $NaClO_4$. From these measurements it is clear that perchlorate is retained to some extent in the PIM-EA-TB host film and "memory" effects have to be taken into account.

The special nature of perchlorate (and BF_4^-) in the PIM-EA-TB host framework may be linked to the size of the hydrated versus the dehydrated anion as well as the energy for (partial) dehydration. It is interesting to compare mono-anion hydration energies[24] for BF_4^- -200 $kJmol^{-1}$, ClO_4^- -219 $kJmol^{-1}$, Cl^- -347 $kJmol^{-1}$, HSO_4^- -335 $kJmol^{-1}$, $H_2PO_4^-$ -473 $kJmol^{-1}$, acetate -373 $kJmol^{-1}$, and tetraphenylborate 42 $kJmol^{-1}$. If partial dehydration of anions is necessary for uptake and transport in the PIM-EA-TB film environment, then BF_4^- and ClO_4^- are clearly preferred. Dehydration of chloride is energetically much more costly. Tetraphenylborate, although being associated with a very low hydration energy, appears too bulky to allow permeation into PIM-EA-TB. Anion effects will be investigated further for the case of protonation.

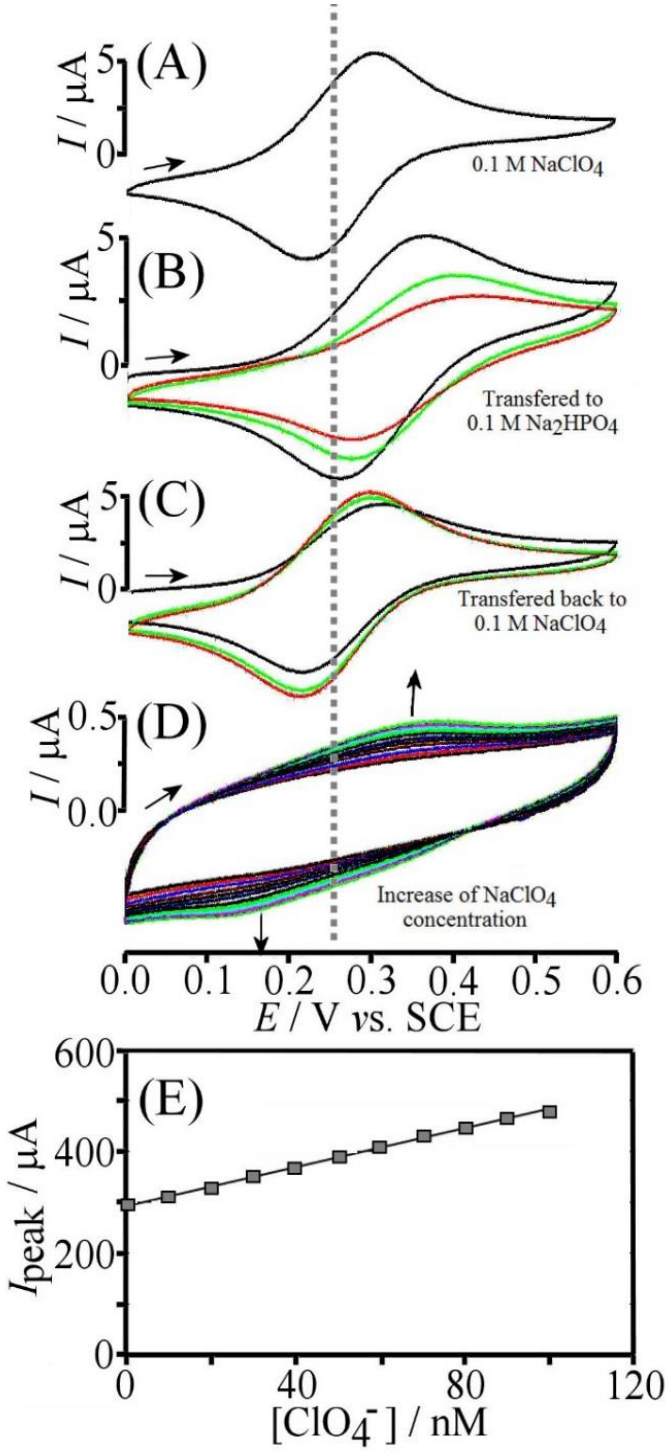

Figure 5.5. Cyclic voltammograms (scan rate 100 mVs^{-1}) for ferrocene – PIM-EA-TB (1:5) film deposited onto glassy carbon and immersed initially (A) 0.1 M $NaClO_4$, (B) then transferred to 0.1 M Na_2HPO_4 (three consecutive cycles: black 1st, green 5th, red 10th), (C) then transferred back to 0.1 M $NaClO_4$ (three consecutive cycles: black 1st, green 5th, red 10th). (D) Cyclic voltammograms (scan rate 100 mVs^{-1}) for ferrocene – PIM-EA-TB (1:5) immersed in 0.1 M Na_2HPO_4 with small additions of ClO_4^- causing a voltammetric signal to emerge. (E) Plot of the anodic peak current versus concentration of ClO_4^- added.

5.3.2 Anion Effects for the Reduction of Protons Absorbed into PIM-EA-TB

The structure of PIM-EA-TB contains two backbone nitrogen atoms in the form of tertiary amines linked to the phenyl group (see Fig.5.2). The pK_A values for the two amines has been suggested to be in the range of 4.0 for the first protonation and 0.4 for the second protonation[13]. These values are likely to be environment/electrolyte dependent and impedance conductivity measurements have confirmed that protonation starting at pH 5[12] is associated with an increase in conductivity. In order to more directly investigate the protonation of the PIM-EA-TB films immobilised at a platinum electrode surface, the electrode was first immersed into a buffer solution (step 1) and then immersed into neutral 0.1 M $NaClO_4$ (step 2) for the reduction of immobilised protons to molecular hydrogen at the platinum electrode surface (equation 5.2).

$$2\ H^+\ (\text{PIM-EA-TB}) \ + \ 2\ e^- \quad \rightleftharpoons \quad H_2\ (aq) \qquad (5.2)$$

Figure 5.6B shows typical cyclic voltammetry responses with a well-defined reduction response at -0.55 V vs. SCE. The reduction is chemically irreversible due to hydrogen product diffusing away into the solution without being re-captured by oxidation. When repeating this experiment as a function of pH in the phosphate buffer solution (containing 0.1 M $NaClO_4$ to avoid memory effects), a series of proton reduction peaks can be measured. The plot in Figure 5.6C shows gradual protonation starting at pH 5 and continuing to pH 2. Similar experiments performed without $NaClO_4$ in the buffer solution proved to be poorly reproducible and complicated by anion effects. The presence of perchlorate anions in the buffer during step 1 is important for reproducible protonation of the PIM-EA-TB film in agreement with observations during ferrocene oxidation (*vide supra*). The magnitude of the charge under the proton reduction peak (reaching 1 μC) is indicative for only a very small fraction of the PIM-EA-TB film close to the platinum electrode being active (the charge expected for 3 μL or 3 μg deposit for single protonation is approx. 1 mC). Therefore, low proton mobility in the presence of anions appears to be important to explain the limited extent of proton reduction in these experiments. Next, anion and proton mobility and "ionic diode effects" are investigated for different anions in a free-standing PIM-EA-TB membrane.

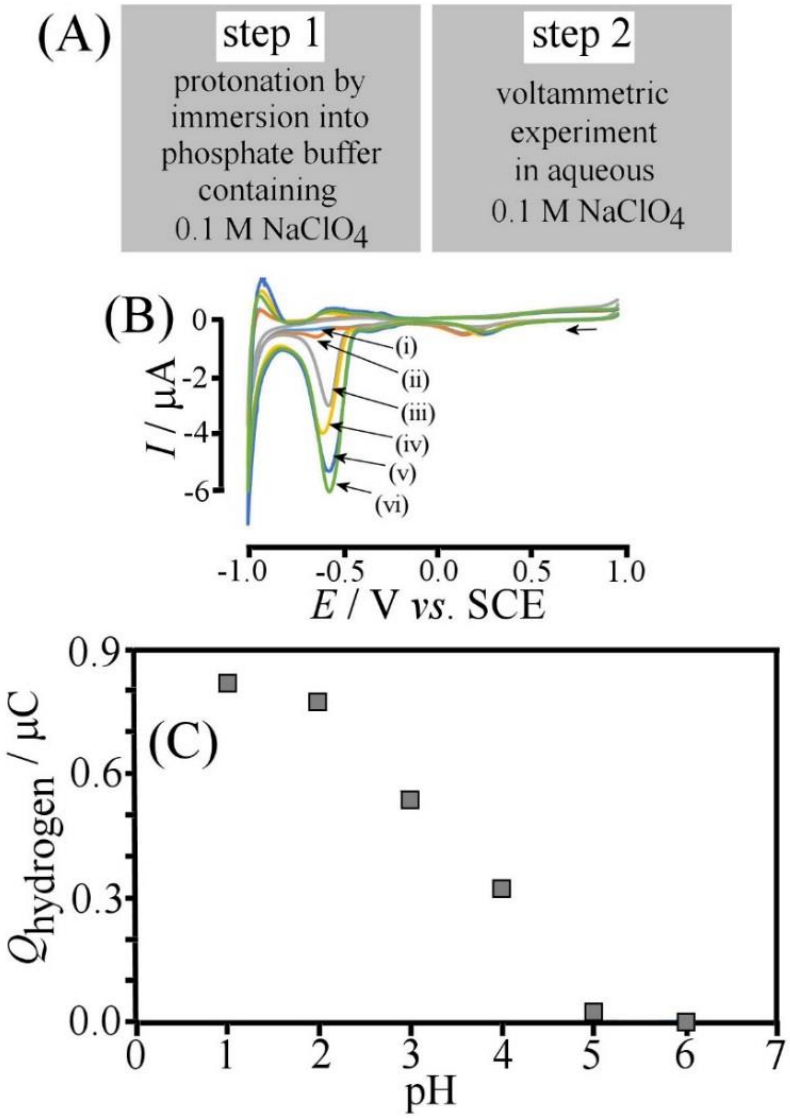

Figure 5.6. (A) Description of the two step experiment with first immersion into phosphate buffer solution containing 0.1 M $NaClO_4$ and second voltammetry in aqueous 0.1 M $NaClO_4$. (B) Cyclic voltammograms (scan rate 5 mVs^{-1}, at a 1.6 mm diameter platinum disc electrode) for the reduction of protons absorbed into 3 μg PIM-EA-TB, 3 μL. Electrodes were pretreated at (i) pH 6, (ii) pH 5, (iii) pH 4, (iv) pH 3, (v) pH 2, and (vi) pH 1. (C) Plot of the charge under the proton reduction peak versus buffer pH.

5.3.3 Anion Effects on Charge Transport through a Free-Standing Membrane of PIM-EA-TB

Membrane electrochemical measurements are performed with a 6 μm thick PET film with a 20 μm diameter pore drilled with a laser[12]. The PET-pore is filled initially by placing 3 times a 2.5 μL drop of PIM-EA-TB in chloroform (1 mg cm^{-3}) over the surface (on agarose gel to reproducibly achieve asymmetric deposits, see experimental). After evaporation of the

chloroform, PIM-EA-TB uniformly covers the surface. Staining with eosin Y and fluorescence imaging allows the PIM-EA-TB material close to the pore to be visualised as highly asymmetric deposit (see Fig.5.2B) with a layer of approximately 10 μm thickness coated only on one side. The surface area exposed to the aqueous solution phase is consistent with the 20 μm diameter pore area on one side and much more extended on the opposite coated side. This asymmetry causes a current rectification or "ionic diode" effect[13] as shown in Figure 5.7.

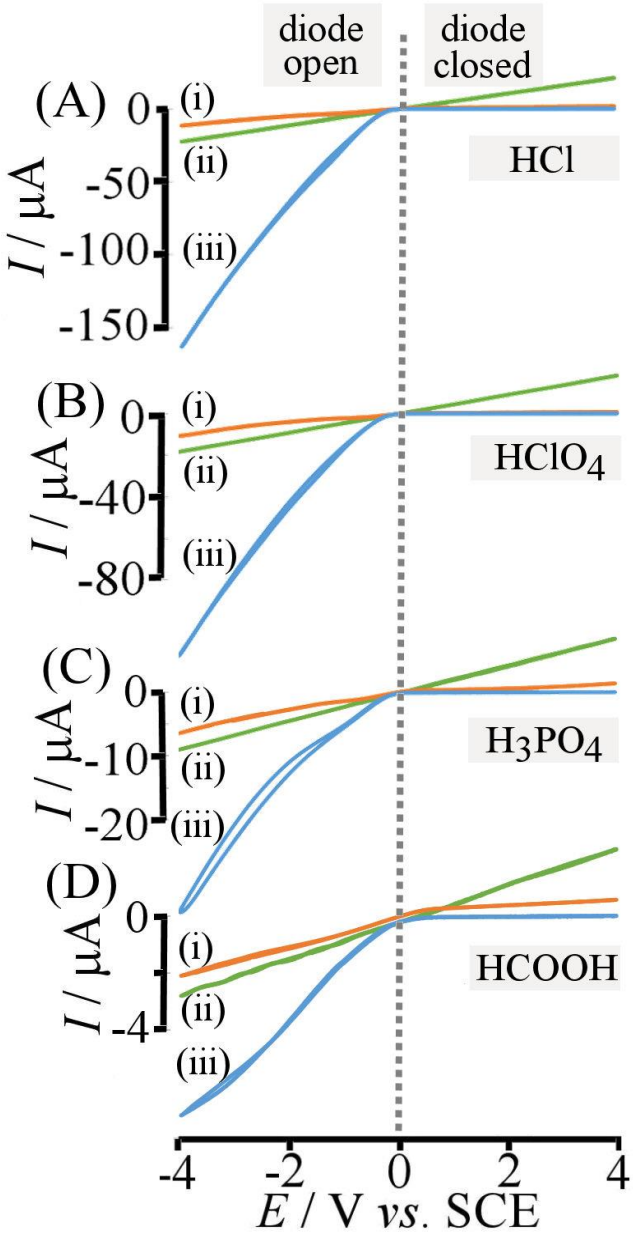

Figure 5.7. (A) Cyclic voltammograms (scan rate 20 mVs^{-1}) for a 20 μm diameter pore in PET asymmetrically filled with PIM-EA-TB between two half-cells with (A) 10 mM HCl, (B) 10 mM $HClO_4$, (C) 10 mM H_3PO_4, and (iv) 10 mM HCOOH. Cyclic voltammograms are shown for (i) a deposit of 7.5 μL 1 mg mL^{-1} PIM-EA-TB, (ii) the open pore, and (iii) a deposit of 7.5 μL 4 mg mL^{-1} PIM-EA-TB. For measurements, the PET film was placed between two half-cell with 10 mM aqueous acid each (see experimental).

The membrane voltammetry experiment is performed in 4-electrode mode (counter / reference electrode in one half cell and working / sense electrode in the opposite half cell) to measure ion flow across the polarised membrane. Note that the PIM-EA-TB deposit is facing towards the working electrode. Figure 5.7A shows voltammetry data for the PET film sandwiched between two aqueous half cells with 10 mM HCl each. Steady state voltammetric responses (at a scan rate of 20 mVs^{-1}) are observed for three cases: (i) a thin film of PIM-EA-TB (7.5 μL of 1 mg mL^{-1}), (ii) the open pore without PIM-EA-TB, and (iii) a thicker film of PIM-EA-TB (7.5 μL of 4 mg mL^{-1}). The voltammogram for the thin PIM-EA-TB deposit shows current rectification with low currents in the positive potential range (see "closed ionic diode") and "Ohmic" characteristics in the negative potential range (see "open ionic diode"). It suggests that anions is conductive in PIM films and contribute to the open current in the negative range. Perhaps surprisingly, a thicker film of PIM-EA-TB considerably enhances the current rectification effect with currents in the positive potential range lower and currents in the negative potential range even higher than those observed for the open pore (*vide infra*).

It is interesting to consider the magnitude of the currents. In the presence of 10 mM HCl, steady state currents (scan rate independent) plateauing at typically 3 μA at -1 V are observed for charge transport through the protonated membranes. When going to more negative potentials the currents further increase presumably due to migration driven ion transport. The theoretical diffusion limited current only towards a 20 μm diameter disc (pore) can be estimated based on microdisc voltammetry theory[25] (equation 5.3).

$$I_{\text{diffusion}} = 4\,F\,D\,c\,r = 70\ \text{nA} \qquad (5.3)$$

In this equation F is the Faraday constant, D is the diffusion coefficient for chloride (approximately 1.8×10^{-9} m^2s^{-1} at 293 K[26]), c is the concentration, and r is the pore radius. The estimated anion diffusion only current, 70 nA, is much lower compared to the observed plateau current. Therefore proton transport must be occurring in addition to chloride anion transport. The diffusion coefficient for protons in water is an order of magnitude higher compared to that for chloride[27] so that the observed initial current plateau can be explained (with an additional contributions from migration within the PIM-EA-TB membrane). Figure 5.8C schematically depicts the additional proton transport in the presence of partially hydrated chloride anions.

For 10 mM $HClO_4$ in both half cells (Fig. 5.7B), a similar trend and strong rectification effects are evident. At positive applied potentials only very low currents flow due to a resistive "depletion layer" forming inside of the membrane (only at the low surface area side of the deposit facing the counter electrode). Figure 5.8A depicts the proposed mechanism in which deprotonation of the membrane occurs in competition with anion uptake. As a result a "depletion zone" is formed where both perchlorate and proton concentration are low and therefore currents are impeded. In contrast, with a negative potential applied the equivalent "depletion zone" effect at the large surface area side of the PIM-EA-TB membrane remains negligible and high currents can flow. The rectification current ratio is dependent on the applied potential and on the type of anion in solution. Transport of anions through the PIM-EA-TB membrane with partial dehydration (*vide supra*) is depicted in Figure 5.8B. Trends for phosphoric acid (Fig. 5.7C) and for formic acid (Fig. 5.7D) are similar to those for chloride and perchlorate, except that the magnitude of currents is much lower.

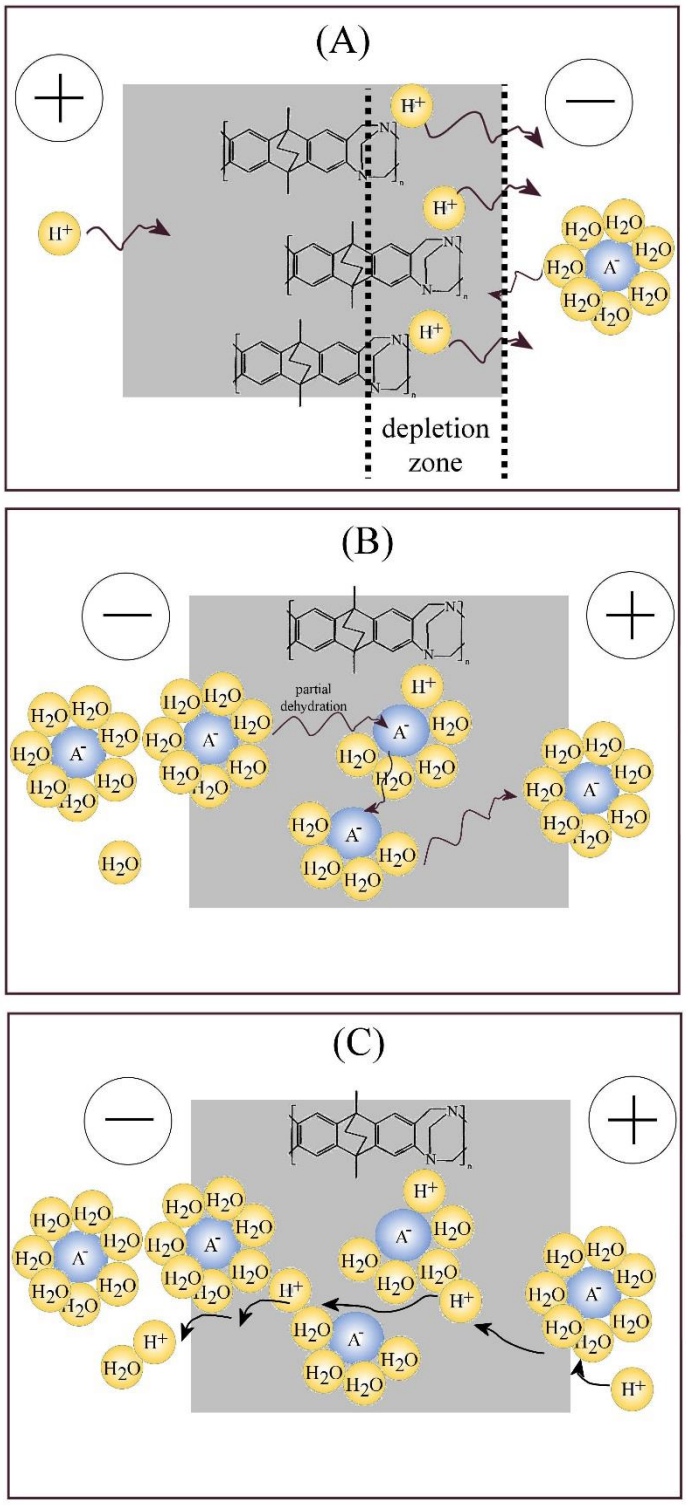

Figure 5.8. Schematic drawing of (A) the expulsion of protons at the PIM-EA-TB - solution interface causing a depletion layer with low conductivity, (B) the effect of partial dehydration in micropores aiding the transport of anions, and (C) flow of protons "catalysed" by the presence of partially hydrated anions.

In order to better compare the behaviour of the “thin” and “thick” PIM-EA-TB membranes for different anions, chronoamperometry data are shown in Figure 5.9. For “thin” PIM-EA-TB deposits switching times of ca. 1 s are observed and currents for the “open diode” (at negative applied potentials) systematically increase with potential from +/-1 V to +/-2 V and to +/-3 V. The sequence of anions consistently shows higher currents for hydrochloric and perchloric acid. For the “thick” membrane case switching times are considerably longer and anion as well as potential dependent. However, the sequence in current magnitude is again HCl > $HClO_4$ > H_3PO_4 > HCOOH.

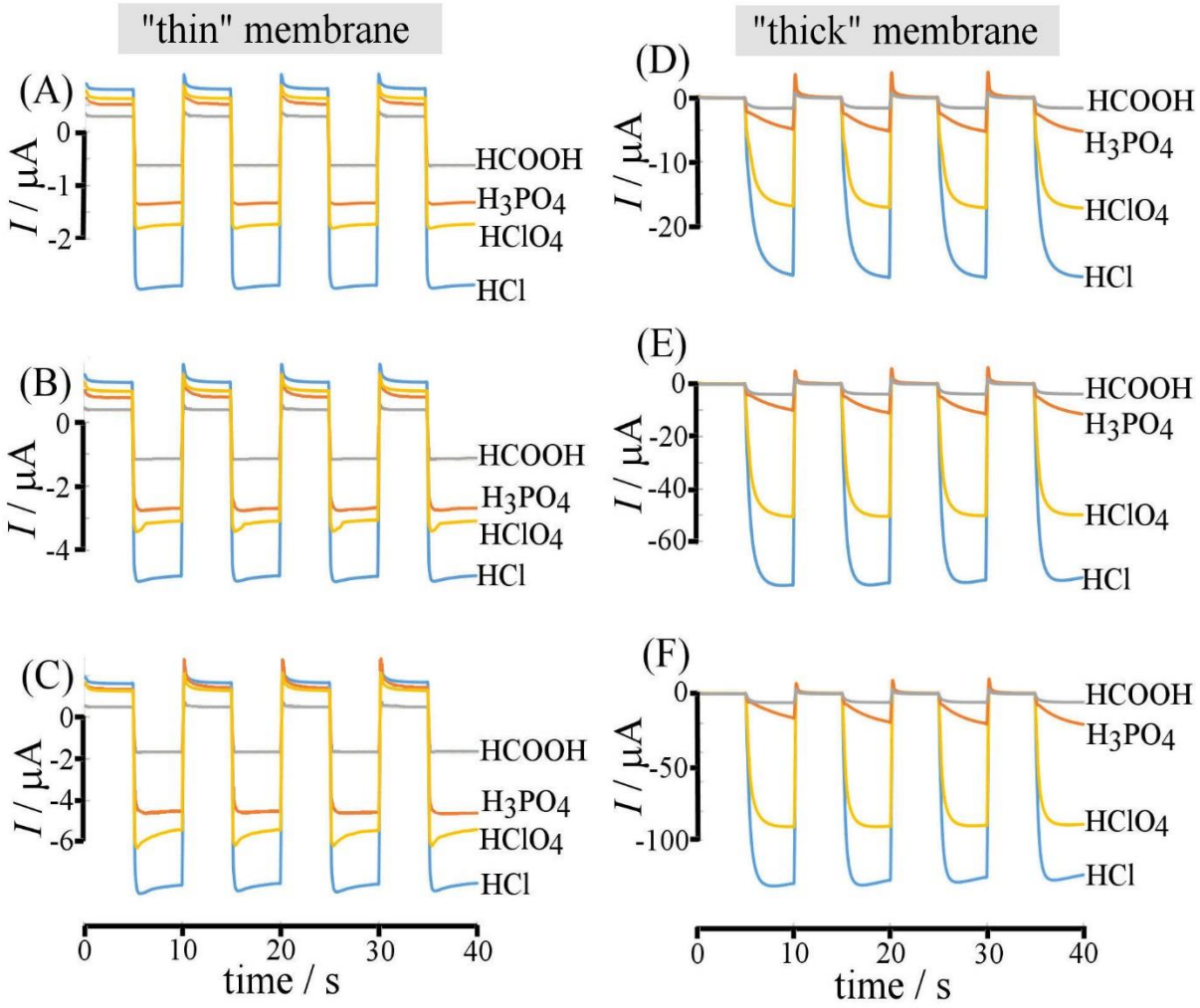

Figure 5.9. Chronoamperometry data for a thin film of PIM-EA-TB (7.5 µL of 1 mg mL^{-1} deposited on PET) switching from (A) +1 V to -1V, (B) +2 V to -2 V, and (C) +3 V to -3 V, and for a thick film of PIM-EA-TB (7.5 µL of 4 mg mL^{-1} deposited on PET) switching from (D) +1 V to -1 V, (E) +2 V to -2 V, and (F) +3 V to -3 V. Half cell solutions were aqueous 10 mM formic acid, phosphoric acid, perchloric acid or hydrochloric acid.

In addition to the steady state current responses, peak features are observed during some of the chronoamperometry experiments (Fig. 5.9). For thin film PIM-EA-TB membranes transient peaks are most clearly defined for perchloric acid experiments where they increase with applied potential (see Fig. 5.9A-C). For thick film chronoamperometry data transient peaks are observed only when "closing" the diode (presumably due to a slower time constant for the "opening" process, see Figure 9D-F). The area under a typical transient peak for the thin PIM-EA-TB membrane and for perchloric acid can be estimated as 1 μC. When considering the total amount of PIM-EA-TB deposited (monomer molecular weight = 200 Dalton; 7.5 μg = 25 nmol = 2.4 mC) it appears obvious that only a small fraction is actively involved in the transient process. However, when estimating the PIM-EA-TB volume only close to the pore (ca. 5 ng = 1.6 μC), the similarity to the measured 1 μC is intriguing. A PIM-EA-TB "charging" or "doping" mechanism does appear plausible with material only in the vicinity of the pore being affected. This is consistent with only material in the vicinity of the pore being responsible for the ionic diode effect. The transient charge of 1 μC is likely to reflect a surge of perchlorate anions (and protons to maintain charge neutrality) to develop an internal concentration gradient for protons and anions to be transported (see Fig. 5.8C). The higher the internal concentration of charges in the PIM-EA-TB film, the better the charge transport is possible (shorter hopping distances). In order to explain the considerably higher currents observed for the "thick" PIM-EA-TB membrane case additional charge generation processes within the polymer may be in operation. Further experiments for example investigating the local pH during operation of the ionic diode will be necessary.

The link between anion properties and charge mobility in the PIM-EA-TB membrane environment is strong with chloride and perchlorate clearly enhancing charge transport in particular for thick PIM-EA-TB membranes. This study of membrane processes is preliminary at this stage and further, more quantitative investigations of the charge transport phenomena in these mixed cation – anion conductor films based on PIM-EA-TB will be required for a wider range of ions, as a function of ionic strength and for mixed electrolyte solutions, and for other pore geometries. The potential for perchlorate extraction also needs further attention.

5.4 Conclusion

It has been shown that polymers of intrinsic microporosity such as PIM-EA-TB offer diverse new phenomena with applications in electrochemical systems. There is an opportunity to immobilize redox active molecules such as metallocenes to allow electrochemical redox cycling in a stable manner and without loss of reagent into the solution phase. This approach is of interest for example for the development of molecular redox battery technology[28]. Results demonstrate selective anion transport in particular with perchlorate and BF_4^- enhancing processes due to lower dehydration energies resulting in improved conductivity in the microporous environment. This result seems of interest also in the context of hydration affecting membrane pore ion mobility as seen for example in biological systems[29].

The role of anions in both protonation and proton transport in PIM-EA-TB has been explored and in particular the ability of chloride and perchlorate to "catalyse" proton transport (with resulting currents much higher compared to those for the open-pore mass transport limited rate) appears important. The ability of perchlorate to shed water molecules (due to its relatively low hydration energy) is likely to contribute to this anion selectivity. Future applications for the mixed cation/anion conducting PIM-EA-TB membrane material could be in electrocatalysis (e.g. with molecular electrocatalysts immobilised at inert electrode surfaces) and in electroanalysis (e.g. exploiting the ability of molecular species such as perchlorate to "switch" proton transport). Most intriguing appears to be the "ionic diode" behaviour with rectification ratios reaching $>10^3$ for thick PIM-EA-TB membranes in 10 mM HCl. New applications for ionic diodes could emerge in energy harvesting[30] or in "iontronics"[31].

5.5 References

1 A. Morozan and F. Jaouen, *Energy Environ. Sci.*, 2012, **5**, 9269–9290.

2 J. E. Halls, D. Jiang, A. D. Burrows, M. A. Kulandainathan and F. Marken, *Electrochemistry within metal-organic frameworks , in Electrochemistry*, Royal Society of Chemistry, Cambridge, 2013.

3 Y. Xu, S. Jin, H. Xu, A. Nagai and D. Jiang, *Chem Soc Rev*, 2013, **42**, 8012–8031.

4 N. B. McKeown and P. M. Budd, *Macromolecules*, 2010, **43**, 5163–5176.

5 N. B. Mckeown and P. M. Budd, *Chem. Soc. Rev.*, 2006, **35**, 675–683.

6 P. M. Budd, N. B. Mckeown, B. S. Ghanem, K. J. Msayib, D. Fritsch, L. Starannikova,

N. Belov, O. Sanfirova, Y. Yampolskii and V. Shantarovich, *J. Membr. Sci. J.*, 2008, **325**, 851–860.

7 N. B. Mckeown, B. Gahnem, K. J. Msayib, P. M. Budd, C. E. Tattershall, K. Mahmood, S. Tan, D. Book, H. W. Langmi and A. Walton, *Angew. Chemie*, 2006, **118**, 1836–1839.

8 P. M. Budd, K. J. Msayib, C. E. Tattershall, B. S. Ghanem, K. J. Reynolds, N. B. Mckeown and D. Fritsch, *J. Memb. Sci.*, 2005, **251**, 263–269.

9 H. Al Kutubi, L. Rassaei, W. Olthuis, G. W. Nelson, J. S. Foord, P. Holdway, M. Carta, R. Malpass-Evans, N. B. McKeown, S. C. Tsang, R. Castaing, F. T. R, M. D. Jones, D. He and F. Marken, *RSC Adv.*, 2015, **5**, 73323–73326.

10 Y. Rong, R. Malpass-evans, M. Carta, N. B. Mckeown, G. A. Attard and F. Marken, *Electrochem. commun.*, 2014, **46**, 26–29.

11 D. He, Y. Rong, Z. Kou, S. Mu, T. Peng, R. Malpass-Evans, M. Carta, N. B. McKeown and F. Marken, *Electrochem. commun.*, 2015, **59**, 72–76.

12 E. Madrid, Y. Rong, M. Carta, N. B. McKeown, R. Malpass-Evans, G. A. Attard, T. J. Clarke, S. H. Taylor, Y. T. Long and F. Marken, *Angew. Chemie*, 2014, **53**, 10751–10754.

13 E. Madrid, P. Cottis, Y. Rong, A. T. Rogers, J. M. Stone, R. Malpass-evans, M. Carta, B. Mckeown and F. Marken, *J. Mater. Chem. A Mater. energy Sustain.*, 2015, **3**, 15849–15853.

14 Y. Rong, R. Malpass-Evans, M. Carta, N. B. Mckeown, G. A. Attard and F. Marken, *Electroanalysis*, 2014, **26**, 904–909.

15 A. Kolodziej, S. D. Ahn, M. Carta, R. Malpass-Evans, N. B. McKeown, R. S. L. Chapman, S. D. Bull and F. Marken, *Electrochim. Acta*, 2015, **160**, 195–201.

16 S. D. Ahn, A. Kolodziej, R. Malpass-Evans, M. Carta, N. B. McKeown, S. D. Bull, A. Buchard and F. Marken, *Electrocatalysis*, 2016, **7**, 70–78.

17 O. P. Soldin, L. E. Braverman and S. . Lamm, *Drug Monit*, 2001, **23**, 316–331.

18 Y. Kim and S. Amemiya, *Anal. Chem.*, 2008, **80**, 6056–6065.

19 V. A. Nzengung, C. Wang and G. Harvey, *Environ. Sci. Technol.*, 1999, **33**, 1470–1478.

20 M. Carta, R. Malpass-Evans, M. Croad, Y. Rogan, J. C. Jansen, P. Bernardo, F. Bazzarelli and N. B. McKeown, *Science (80-.).*, 2013, **339**, 303–307.

21 A. A. J. Torriero, J. Sunarso and P. . Howlett, *Electrochim. Acta*, 2012, **82**, 60–68.

22 A. M. Bond and F. Scholz, *Langmuir*, 1991, **7**, 3197–3204.

23 A. M. Kelly, N. Katif, T. D. James and F. Marken, *New J. Chem.*, 2010, **34**, 1261–1265.

24 Y. Macrus, *Ion Properties*, New York, 1997.

25 A. J. Bard and L. R. Faulkner, *Electrochemical Methods: Fundamentals and Applications*, John Wiley, New York, second., 2011.

26 R. Mills and V. M. M. Lobo, *Self-Diffusion in Electrolyte Solution*, Elsevier, Amsterdam, 1989.

27 J. Weber, A. J. Wain and F. Marken, *Electroanalysis*, 2015, **27**, 1829–1835.

28 W. Tian, X. Mao, P. Brown, G. C. Rutledge and T. A. Hatton, *Adv. Funtional Mater.*, 2015, **25**, 4803–4813.

29 S. Y. Noskov and B. Roux, *J. Gen. Physiol.*, 2007, **129**, 135–143.

30 J. Gao, W. Guo, D. Feng, H. Wang, D. Zhao and L. Jiang, *J. Am. Chem. Soc.*, 2014, **136**, 12265–12272.

31 H. Chun and T. D. Chung, *Annu. Rev. Anal. Chem.*, 2015, **8**, 441–462.

Chapter 6: pH-Induced Reversal of Ionic Diode Polarity in 300 nm Thin Membranes Based on a Polymer of Intrinsic Microporosity

Chapter Abstract

"Ionic diode" (or current rectification) effects are potentially important for a range of applications including water purification. In this preliminary report, we observe novel ionic diode behaviour of thin (300 nm) membranes based on a polymer of intrinsic microporosity (PIM-EA-TB) supported on a poly-ethylene-terephthalate (PET) film with a 20 μm diameter microhole, and immersed in aqueous electrolyte media. Current rectification effects are observed for half-cells with the same electrolyte solution on both sides of the membrane for cases where cation and anion mobility differ (HCl, other acids, NaOH, etc.) but not for cases where cation and anion mobility are more alike (LiCl, NaCl, KCl, etc.). A pH-dependent reversal of the ionic diode effect is observed and discussed in terms of tentatively assigned mechanisms based on both (i) ion mobility within the PIM-EA-TB nano-membrane and (ii) a possible "mechanical valve effect" linked to membrane potential and electrokinetic movement of the membrane as well as hydrostatic pressure effects.

Graphical Abstract:

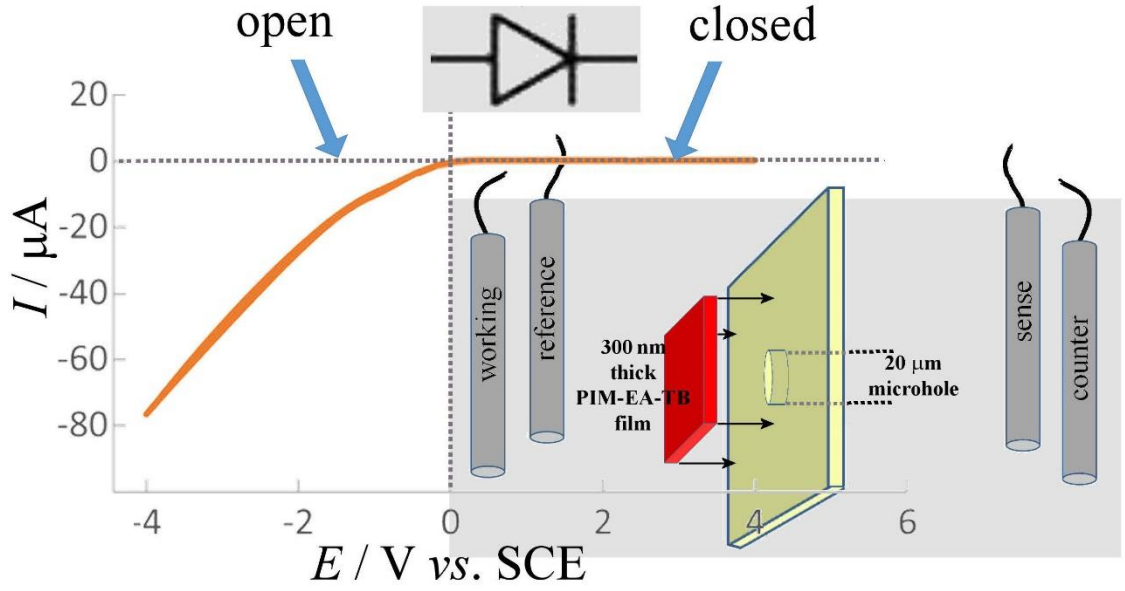

Chapter Publications

This chapter has been published in:

Y. Rong, Q. Song, K. Mathwig, E. Madrid, D. He, R. G. Niemann, P. J. Cameron, S. E.C. Dale , S. Bending, M. Carta, R. Malpass-Evans, N. B. McKeown and F. Marken, *Electrochemistry Communications*, ,**2016**, 69, 41-45.

Acknowledgements

I would like to thank Dr. Qilei Song for his help in making PIM thin films and Dr. Sara Dale for her help of AFM images.

6.1 Introduction

Interest in "ionic devices"[1–5] has increased over the recent years with the emergence of new nanopore technologies[6,7] and availability of new microporous materials[8]. The potential for applications of these devices ranges from analytical nanofluidic tools[9], natural cell pore mimics[10], to energy harvesting systems, and ionic rectifiers for desalination[11]. Ionic rectification (or "ionic diode"[12]) effects are well-known in particular for gel-junctions[13] and hydrogel materials[14]. Both nano-engineered nano-pores and novel microporous materials can contribute to the development of ionic rectifiers and devices. There are opportunities to exploit properties of new types of microporous materials (such as polymers of intrinsic microporosity or PIMs) for improved ionic diodes. In this preliminary report we explore the effects on ion flow by applying very thin PIM membranes produced by spin-coating followed by lift off and transfer.

Polymers of intrinsic microporosity[15,16] have emerged recently as a novel class of materials based on molecularly highly rigid structures that are highly processible (e.g. soluble in organic solvents for casting of films and membranes[17]) and highly porous with typical BET surface area values ≈1000 m^2g^{-1}[18]. Initial work focused on the gas-phase, but recently also liquid-phase applications have been explored based on stabilisation of fuel cell catalysts[19], "heterogenisation" of molecular catalysts[20,21], formation of novel microporous heterocarbon structures[22], and current rectification[23]. In previous work we employed solution casting methods to give relatively thick (typically 10 μm or more) PIM membranes. However, it is highly interesting to explore much thinner polymer nano-membranes. It is demonstrated here, that even very thin films of PIM-EA-TB (with typically 300 nm thickness) can be employed successfully for current rectification in ionic diode devices.

6.2 Experimental

6.2.1 Chemical Reagents

Polymer PIM-EA-TB was prepared following a literature procedure[18]. Hydrochloric acid (37%), perchloric acid (70%), sulfuric acid (98%) and phosphoric acid (85%), and electrolyte salts were obtained from Sigma-Aldrich or Fisher Scientific and used without further

purification. Solutions were prepared with deionized water of resistivity 18.2MΩ cm (at 20 ºC) from a Thermo Scientific water purification system.

6.2.2 Instrumentation

A potentiostat system (Ivium Compactstat) was employed with Pt wires as working/counter electrodes, and two KCl-saturated calomel reference electrodes (SCE, Radiometer, Copenhagen) as sense and reference electrode in a 4-electrode membrane cell (Figure 1A). The membrane sample was always on the side of the working electrode.

6.2.3 Preparation of Nano-membranes

A thin PIM-EA-TB film was spin-coated on a cover glass using 2 wt. % PIM-EA-TB in chloroform solution (Laurell WS-650Mz-23NPP, 2000 rpm for 1 min). Next, the PIM-EA-TB film was lifted off in water and then transferred to a PET film with a ca. 20 μm diameter micro-hole (supplied by Laser Micromachining Limited, St. Asaph, Denbighshire LL17 0JG, UK). AFM thickness measurements of the PIM-EA-TB film on a glass slide in dry ambient conditions (Fig.6.1B, C) reveal typically 300 nm thickness produced with this concentration of PIM-EA-TB.

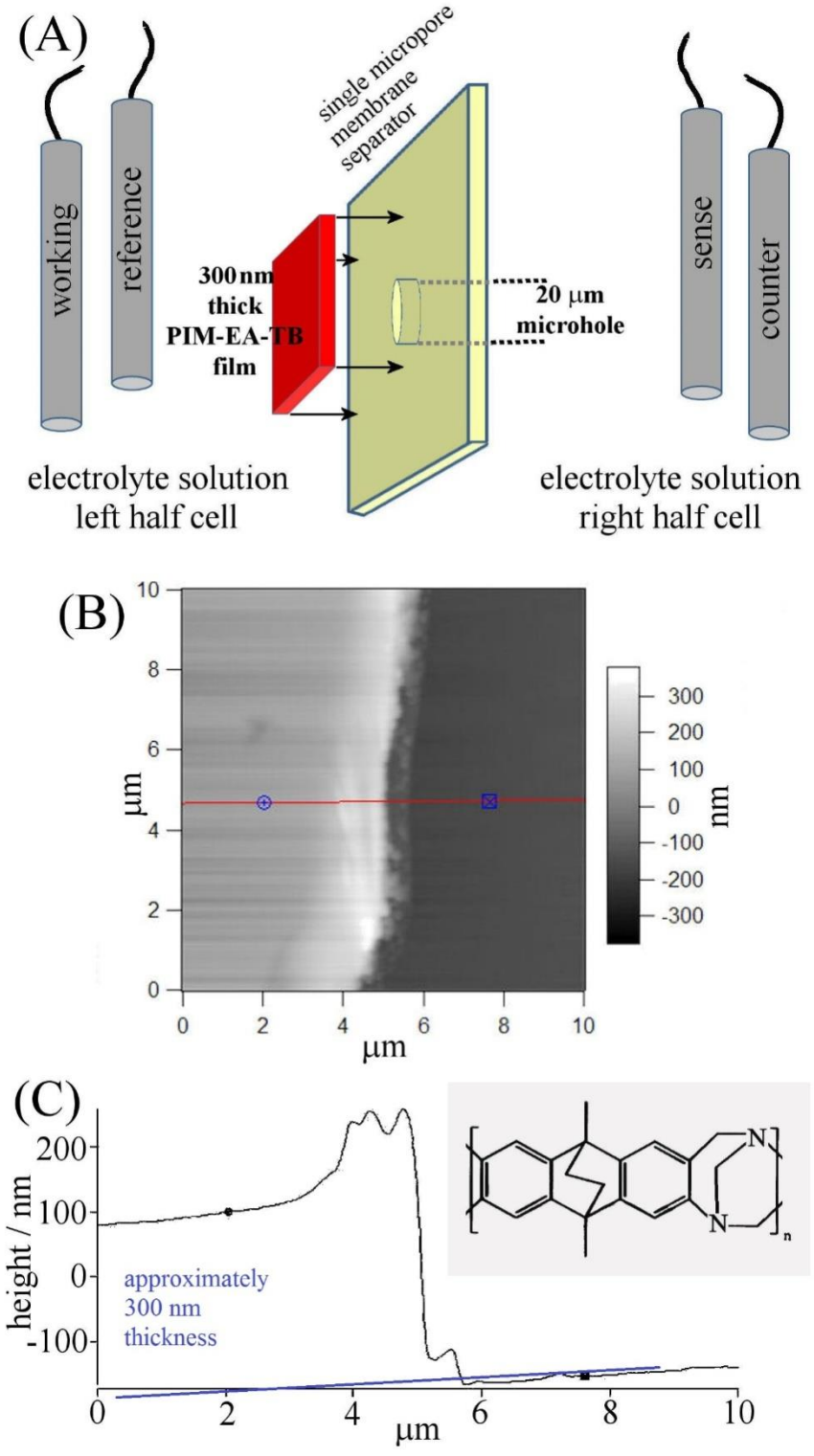

Figure 6. 1. (A) Schematic drawing of the 4-electrode membrane polarisation experiment based on a 20 μm diameter micro-hole that is covered with a typically 300 nm thin PIM-EA-TB membrane. (B) AFM image of the spin-coated PIM-EA-TB membrane after cutting to reveal the thickness. (C) Cross-sectional profile (inset molecular structure of PIM-EA-TB).

6.3 Results and Discussion

6.3.1 Electrolyte and pH Effects

Figure 6.2A shows cyclic voltammetry data for a 300 nm thin PIM-EA-TB film covering a 20 μm diameter micro-hole in a 6 μm thick PET film. The data for 10 mM HCl (Fig. 6.2Ai) clearly show very low currents in the positive potential range ("closed" diode) and significant currents in the negative potential range ("open" diode). Schematic diagrams in Figure 6.2E and 6.2F tentatively (following a mechanism suggested in earlier work[11]) explain this behaviour at least qualitatively based on protonation of the amine sites in PIM-EA-TB (see structure in Fig.6.1) leading to mixed proton and chloride conductivity. In the "open" diode state, the depletion effect may occur at the open side exposed to the electrolyte solution. In contrast, in the "closed" diode state depletion occurs in a restricted region and therefore causes a significant drop in current and the rectification effect. When extracting currents at -1V and +1V, the rectification ratio for the "nano-membrane" (defined here as I_{open}/I_{closed}) is 180 (compared to 576 reported recently for data obtained for much thicker PIM-EA-TB deposits[23]).

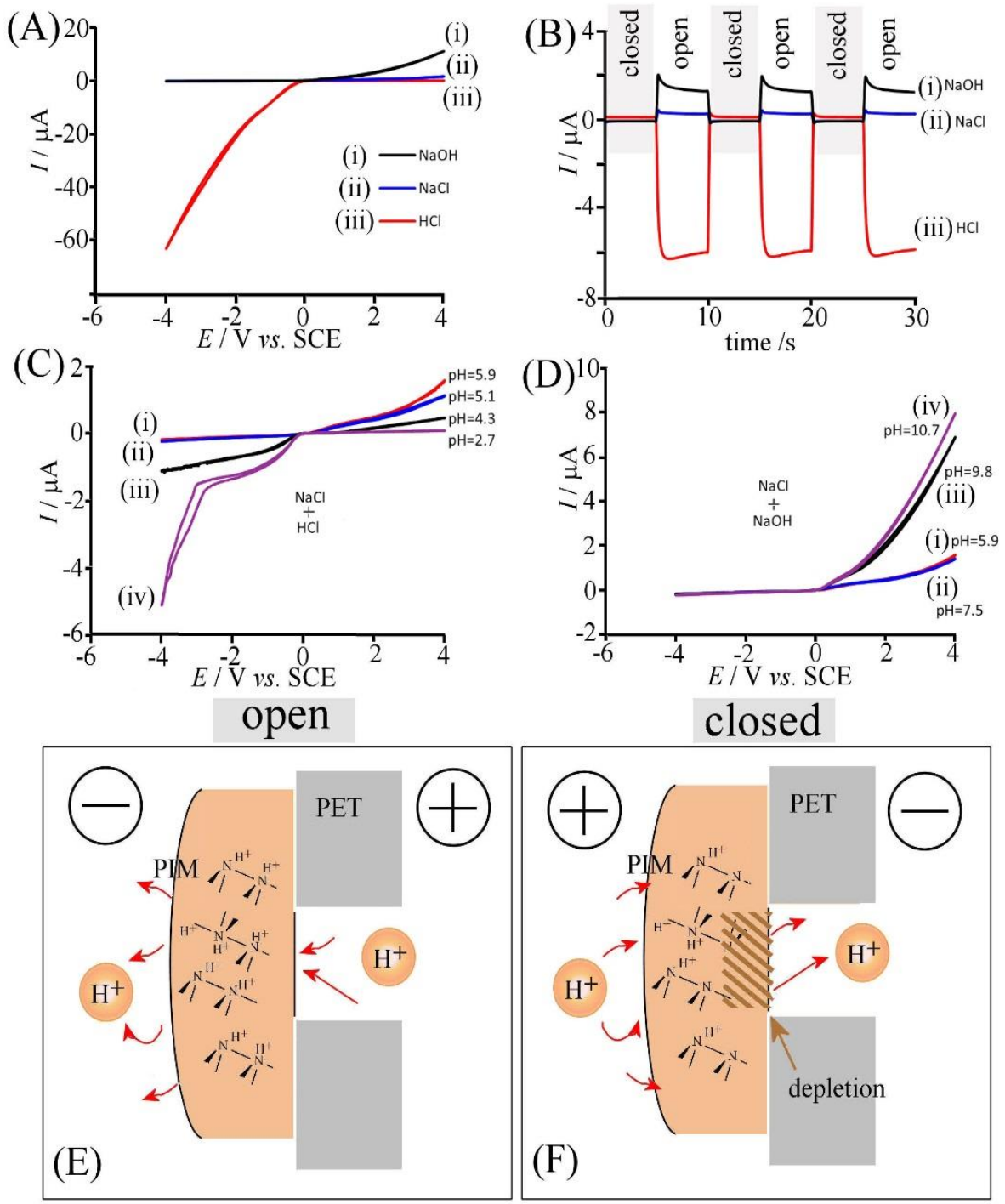

Figure 6. 2. (A) Cyclic voltammograms (50 mV s^{-1}) for a PIM-EA-TB membrane in 10 mM HCl, 10 mM NaCl, and 10 mM NaOH. (B) Chronoamperometry (+1 and -1 V) for 10 mM HCl, 10 mM NaCl, and 10 mM NaOH. (C) Cyclic voltammograms (50 mVs^{-1}) for 10 mM NaCl with the pH adjusted with HCl. (D) As before, but with the pH adjusted with NaOH. (E, F) Schematic drawing of the ionic diode in "open" and "closed" states. (Note, anions are present to maintain electrical neutrality and anions are likely to contribute to the transport in the open state)

Additional chronoamperometry experiments were conducted switching the applied potential between +1 V and -1 V (see Fig.6.2B) and it can be observed that the current switches rapidly from +0.03 μA to -5.0 μA consistent with a rectification ratio of 180. Similar experiments performed with 10 mM NaCl do not result in significant rectification effects although conductivity through the membrane is observed (see Fig.6.2Aii). That is, both Na^+ and Cl^- are likely to move through the porous PIM-EA-TB structure, but ion mobilities are similar and significant depletion effects do not arise. Interestingly, for the case of 10 mM NaOH, there is again a current rectification effect (see Fig.6.2Aiii). Chronoamperometry data in Figure 6.2Bii show that, when switching the potential from -1 V to +1 V, the current switches from -0.02 μA to 1.6μA, suggesting a difference in mobility for Na^+ and OH^- in PIM-EA-TB causing a reversal of the ionic diode polarity. Data in Figure 6.2C and 6.2D show the gradual change in rectification effects with pH consistent with an approximate pK_A for PIM-EA-TB at pH 4[23].

6.3.2 Ionic Strength Effects

When changing the concentration for HCl and for NaOH, currents increase but the rectification ratio at +1 V and -1 V remains approximately constant (Fig.6.3A-B). However, when surveying different types of acids, a clear trend is observed with HCl giving good rectification effects followed by $HClO_4$, H_2SO_4, and H_3PO_4 giving only poor rectification effects with rectification ratios of 180, 51, 8.0, and 6.7, respectively (Fig.6.3C). The poorer rectification effects with H_3PO_4 are likely to be linked to phosphoric acid exhibiting pK_A values higher than that of the PIM-EA-TB, and therefore providing additional protons to weaken the ion depletion effect. When comparing neutral electrolyte media for a range of different anions (see Fig.6.3D), significant rectification effects are observed also for BF_4^-, suggesting that the nature of the anion also can have a strong effect on current rectification phenomena in the PIM-EA-TB membrane.

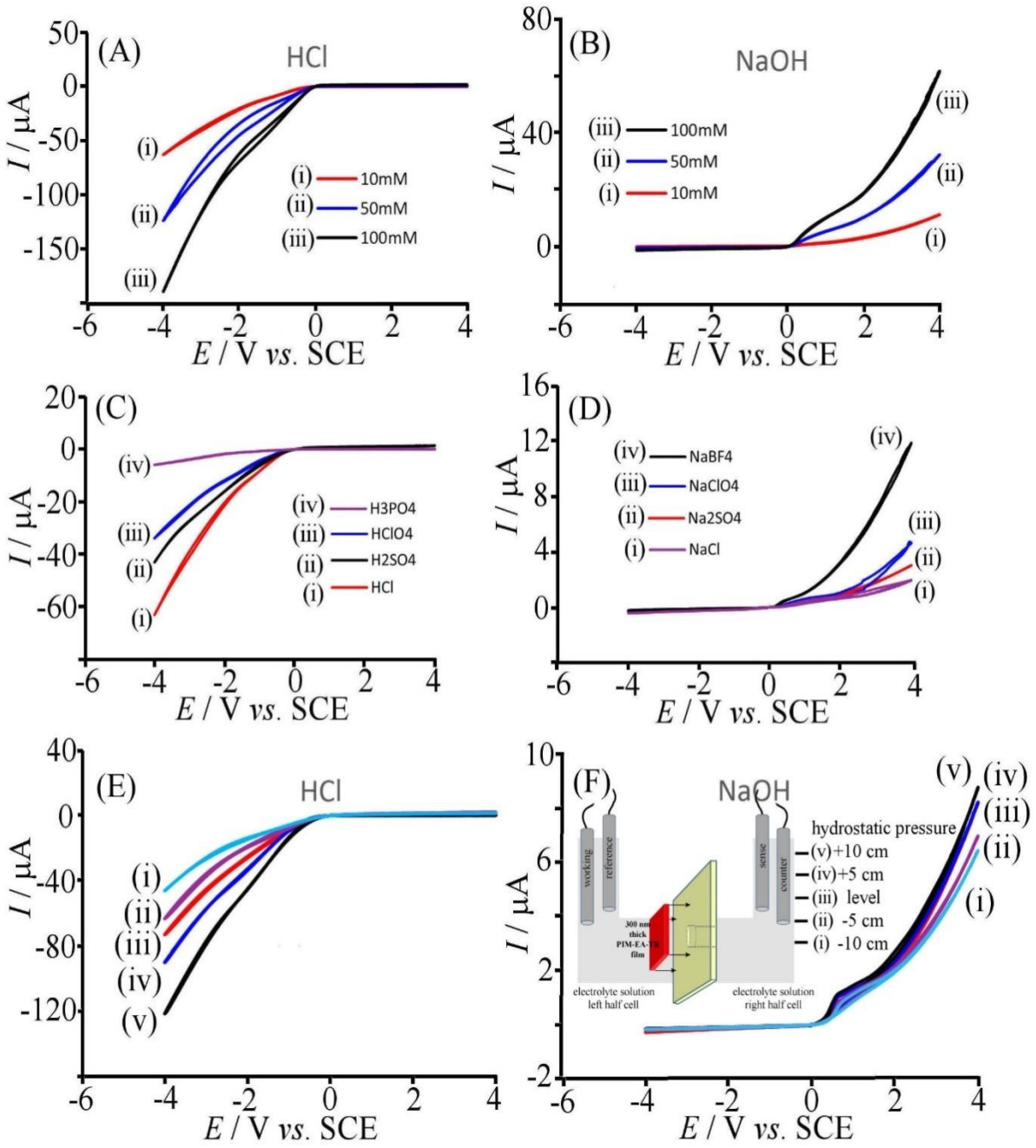

Figure 6. 3. (A) Cyclic voltammograms (50 mVs^{-1}) for PIM-EA-TB membrane in (i) 10 mM, (ii) 50 mM, and (iii) 100 mM HCl. (B) As above, but for (i) 10 mM NaOH, (ii) 50 mM NaOH, and (iii) 100 mM NaOH. (C) Cyclic voltammograms (50 mVs^{-1}) for a PIM-EA-TB membrane in 10 mM HCl (i), H_2SO_4 (ii), $HClO_4$ (iii), and H_3PO_4 (iv). (D) As above, but with 10 mM (i) Na_2SO_4, (ii) NaCl, (iii) $NaClO_4$ and (iv) $NaBF_4$. (E) Cyclic voltammograms (50 mVs^{-1}) for a PIM-EA-TB membrane in 10 mM HCl with varying hydrostatic pressure (see F inset, the fill-height of one half-cell relative to the second was systematically varied by adding or removing electrolyte to give (i) -10, (ii) -5, (iii) 0, (iv) +5, (v) +10 cm hydrostatic pressure in the counter relative to the working compartment). (F) As before, but for 10 mM NaOH.

6.3.3 Hydrostatic Pressure Effects

Measurements were performed for 10 mM HCl (Fig.6.3E) and for 10 mM NaOH (Fig.6.3F) by varying the hydrostatic pressure across the measurement cell by simply adding or removing electrolyte solution (see inset in Fig.6.3F, data for 0, +/-5, and +/-10 cm water column). For HCl the ionic diode effect is significantly affected by hydrostatic pressure, whereas the effects for NaOH are small. Strikingly, the "open diode" current is increased when additional pressure is applied. This suggests that further "opening" or "tuning" of the diode could be linked to a "mechanical valve" phenomenon, where "bulging" of the thin PIM-EA-TB nano-membrane over the 20 μm microhole will cause a geometry change and thereby contribute to additional changes in flow of current. Further work, for example revealing how membrane potential (associated to electrokinetic effects) and ion size effects are linked to the observed phenomena, will be necessary to identify, quantify, and exploit the processes behind these PIM nano-membrane-based current rectification effects.

6.4 Conclusion

It has been shown that a very thin (300 nm) PIM-EA-TB membrane can generate significant "ionic diode" effects and could therefore be employed in ionic rectifier-based devices. The switch in ionic diode polarity is novel and linked to the pH of the electrolyte. This phenomenon is explained here tentatively as based on (i) ion mobility differences within the PIM-EA-TB film and (ii) a valve-like opening of the membrane (driven by electrokinetic or hydrostatic effects) over the supporting PET film microhole. Further work will be required, experimentally and theoretically, to better understand ion mobility and reactivity within PIM films and to further develop and exploit these phenomena in areas such as energy harvesting and desalination.

6.5 References

1 H. Chun and T. D. Chung, *Annu. Rev. Anal. Chem*, 2015, **8**, 441–462.

2 L. Hegedus, N. Kirschner, M. Wittmann and Z. Noszticzius, *J. Phys. Chem. A*, 1998, **102**, 6491–6497.

3 G. Sun, S. Senapati and H.-C. Chang, *Lab Chip*, 2016, **16**, 1171–1177.

4 R. Zhao, G. He and Y. Deng, *Electrochem. commun.*, 2012, **23**, 106–109.

5 E. Madrid, Y. Rong, M. Carta, N. B. McKeown, R. Malpass-Evans, G. A. Attard, T. J. Clarke, S. H. Taylor, Y. T. Long and F. Marken, *Angew. Chemie*, 2014, **53**, 10751–10754.

6 J. K. Rosenstein, S. G. Lemay and K. L. Shepard, *Nanobiotechnol*, 2015, **7**, 475–493.

7 Z. S. Siwy and S. Howorka, *Chem Soc Rev*, 2010, **39**, 1115–1132.

8 E. Madrid, M. A. Buckingham, J. M. Stone, A. T. Rogers, W. J. Gee, A. D. Burrows, P. R. Raithby, V. Celorrio, D. J. Fermin and F. Marken, *Chem. Commun.*, 2016, **52**, 2792–2794.

9 A. Gencoglu and A. R. Minerick, *Microfluid Nanoflui*, 2014, **17**, 781–807.

10 N. Liu, Z. Yang, X. Ou, B. Wei and J. Zhang, *Microchim Acta*, 2016, **183**, 955–963.

11 E. Madrid, P. Cottis, Y. Rong, A. T. Rogers, J. M. Stone, R. Malpass-evans, M. Carta, B. Mckeown and F. Marken, *J. Mater. Chem. A Mater. energy Sustain.*, 2015, **3**, 15849–15853.

12 W. Guo, Y. Tian and L. Jiang, *Acc. Chem. Res.*, 2013, **46**, 2834–2846.

13 B. Lovrecek, A. Despic and J. O. M. Bockris, *J. Mater. Chem.*, 1959, **63**, 750–751.

14 H. Koo and O. D. Velev, *Biomicrofluidics*, 2013, **7**, 031501–031509.

15 P. M. Budd, B. S. Ghanem, S. Makhseed, N. B. Mckeown, K. J. Msayib and E. Tattershall, *Chem. Commun.*, 2004, **2**, 230–231.

16 N. B. McKeown and P. M. Budd, *Macromolecules*, 2010, **43**, 5163–5176.

17 F. Xia, M. Pan, S. Mu, R. Malpass-Evans, M. Carta, N. B. McKeown, G. A. Attard, A. Brew, D. J. Morgan and F. Marken, *Electrochim. Acta*, 2014, **128**, 3–9.

18 M. Carta, R. Malpass-Evans, M. Croad, Y. Rogan, J. C. Jansen, P. Bernardo, F. Bazzarelli and N. B. McKewon, *Science (80-.).*, 2013, **339**, 303–307.

19 D. He, Y. Rong, Z. Kou, S. Mu, T. Peng, R. Malpass-Evans, M. Carta, N. B. McKeown and F. Marken, *Electrochem. commun.*, 2015, **59**, 72–76.

20 S. D. Ahn, A. Kolodziej, R. Malpass-Evans, M. Carta, N. B. McKeown, S. D. Bull, A. Buchard and F. Marken, *Electrocatalysis*, 2016, **7**, 70–78.

21 Y. Rong, R. Malpass-evans, M. Carta, N. B. Mckeown, G. A. Attard and F. Marken, *Electrochem. commun.*, 2014, **46**, 26–29.

22 Y. Rong, D. He, A. Sanchez-fernandez, C. Evans, K. J. Edler, R. Malpass-evans, M. Carta, N. B. Mckeown, T. J. Clarke, S. H. Taylor, A. J. Wain, J. M. Mitchels and F. Marken, *Langmuir*, 2015, **31**, 12300–12306.

23 Y. Rong, A. Kolodziej, E. Madrid, M. Carta, R. Malpass-evans, N. B. Mckeown and F. Marken, *J. Electroanal. Chem.*, 2015, **779**, 241–249.

Chapter 7: Intrinsically Porous Polymer Retains Porosity in Vacuum Thermolysis to Supercapacitive Micropore Carbon

Chapter Abstract

Vacuum carbonisation of organic precursors usually causes considerable structural damage and collapse of morphological features. However, for a polymer with intrinsic microporosity (PIM-EA-TB with a Brunauer-Emmet-Teller (BET) surface area of 1027 m^2g^{-1}), it is shown here that the rigidity of the molecular backbone is retained even during 500 ^oC vacuum carbonisation with a novel type of microporous hetero-carbon being produced (both as powder or as thin film membrane). After carbonisation, the SEM morphology and the SAXS Guinier radius (ca. 38 nm) remain as does the cumulative pore volume. The BET surface area is decreased to 242 m^2g^{-1}, but microporosity is considerably increased. Electrochemical features include two different capacitance domains switching from ca. 30 Fg^{-1} (when oxidised) to ca. 147 Fg^{-1} (when reduced), a very low electron transfer reactivity towards oxygen and hydrogen peroxide, and a four-point-probe resistivity (dry) of approximately 40 MΩ/square for a 1-2 μm thick film.

Graphical Abstract:

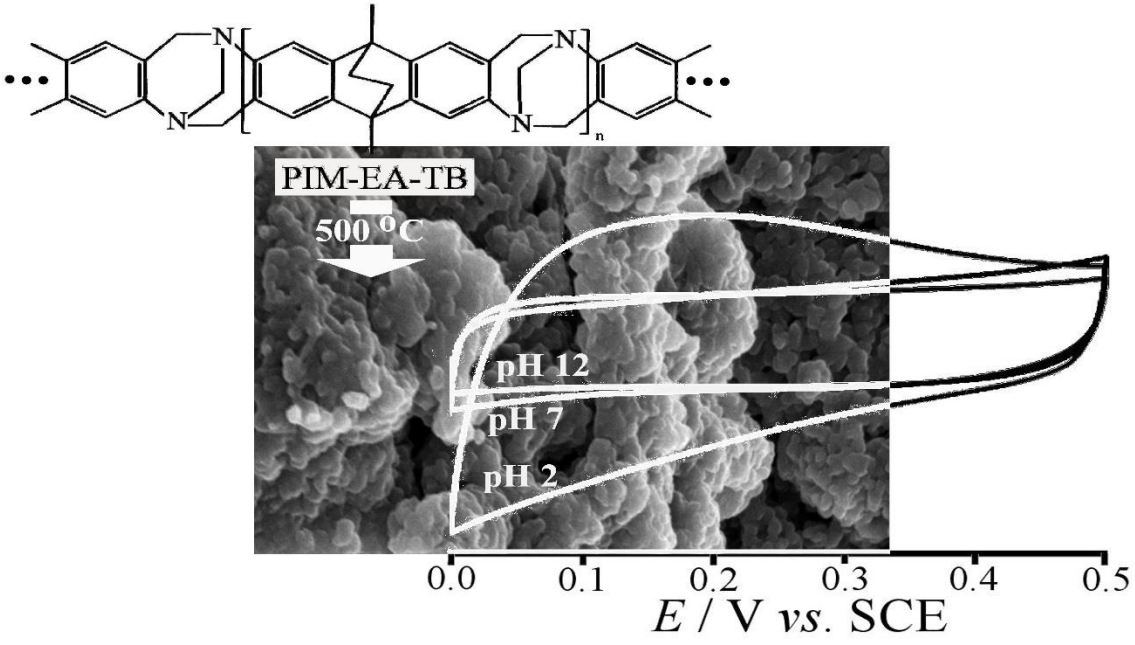

Chapter Publications

This chapter has been published in:

Y. Rong, D. He, A. Sanchez-Fernandez, C. Evans, K. J. Elder, R. Malpass-Evans, M. Carta, N. B. McKewon, T. J. Clarke, S. H. Taylor, A. J. Wain, J. M. Mitchels and F. Marken. *Langmuir,* **2015**, 31, 12300-12306.

Acknowledgements

I would like to thank Dr. Nick Terrill for assistance with the SAXS experiments and Diamond Light Source for access to beamline I22 (SM 11392-1) and thank Dr. Andy Wain for the SECM measurements that contributed to the results presented here.

7.1 Introduction

Vacuum carbonisation[1,2] offers a direct approach to the formation of porous carbon products[3–5] via conversion of organic precursor materials such as cellulose[6,7], starches[8,9], chitosan[10,11], poly-acrylonitrile[12,13], poly-pyridine[14], graphene oxide[15,16], or other types of carbon sources[17,18]. Charring may occur under mild conditions, but graphitisation only talks place at much higher temperatures (beyond 1000 ^{o}C) yielding more ordered and more electrically conducting forms of carbon[19,20]. In this case, a clear link between the precursor molecular structure and the carbonised product structure is not usually evident due to the complex fragmentation and backbone cross-linking processes occurring in such organic materials. Hence, controlling the physical and chemical properties of carbons produced in this way can be highly challenging. Synthesis methods for mesoporous carbons have been introduced based on clay additives controlling pore size[21]. Mild carbonisation without significant morphology changes has been reported recently for ZIF-8 type materials[22,23] and for rigid porous metal-organic framework materials[24,25], with applications, for example for CO_2 capture[23] and in battery systems[26]. Therefore, a highly rigid and thermally robust polymer of intrinsic microporosity (PIM) is employed to demonstrate the case of mild carbonisation without structural collapse and uniquely, without loss of backbone nitrogen functionalities. The remaining nitrogen functionality is associated with a proton-transfer-associated step in capacitance.

PIM materials[27] have been developed for applications in gas separation[28–30], and for gas sensing[31]. Recently, structures such as PIM-EA-TB (see Fig.7.1) have been shown to also provide novel properties for applications in electrocatalysis[32] or for electrochemically active membranes. The presence of protonation sites (two tertiary nitrogen functionalities in PIM-EA-TB, see Fig.7.1) affect ion conductivity and "ionic diode" phenomena[33]. It is shown here that these structural nitrogens as well as porosity are retained during mild carbonisation with interesting effects on the properties of the resulting supercapacitive microporous hetero-carbon.

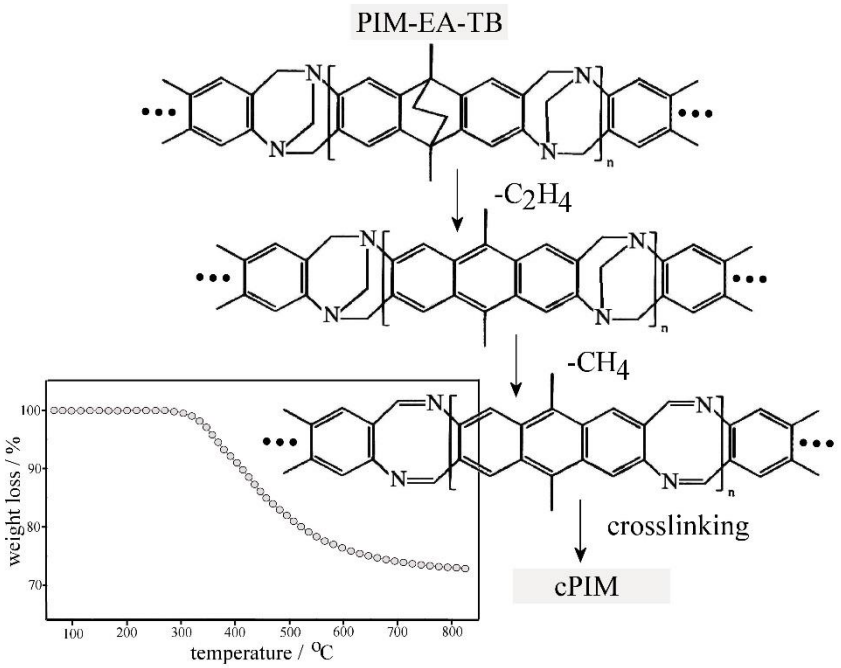

Figure 7. 1. Molecular structure of PIM-EA-TB and hypothetical scheme for thermolysis processes indicating ethylene and methane loss (corresponding to ca. 15% weight loss). Also shown in the thermogravimetric trace for PIM-EA-TB under nitrogen with ca. 18% weight loss at 500 °C.

In this report it is demonstrated that 500 °C vacuum carbonisation of PIM-EA-TB precursor results in the formation of a novel hetero-carbon material with (i) very high microporosity, (ii) low electrical conductivity, (iii) a high pH-switchable capacitance with two distinct proton concentration dependent potential domains, (iv) very low electron transfer reactivity towards oxygen and hydrogen peroxide, and (v) retention of morphology (as powder or film) during carbonisation.

7.2 Experimental

7.2.1 Chemical Reagents

Chloroform, phosphoric acid (85%) and sodium hydroxide were purchased from Aldrich and used without further purification. PIM-EA-TB was obtained following a literature recipe[34]. Solutions were prepared with filtered and deionized water of resistivity of 18.2 MΩ cm from a Thermo Scientific water purification system (ELGA).

7.2.2 Instrumentation

A potentiostat system (IVIUM Compactstat) was employed with a Pt wire counter electrode and a KCl-saturated calomel reference (SCE, Radiometer, Copenhagen). The working electrode was prepared from ITO coated glass (tin-doped indium oxide film sputter-coated onto glass, active area 10 mm × 10 mm, resistivity ca.15 Ω per square) obtained from Image Optics Components Ltd (Basildon, Essec, UK). SECM measurements were performed using 10 μm diameter Pt SECM probe controlled by a CHI 900B system (CH Instruments, Texas). Generator-collector experiments were undertaken by biasing the tip at a fixed potential of 0.6V (sufficient to oxidized H_2O_2) while sweeping the substrate potential at a tip-surface separation of approximately 5 μm.

Four-point probe measurements were performed with a film on a glass slide using a Jandel system. Electron micrographs were obtained on a field emission scanning electron microscope (JEOL FESEM6301F). XPS data were obtained on a Kratos Axis Ultra DLD system using a fixed anode monochromatic Al K_α X-ray source operating at 120 W. Thermogravimetric data (TGA) data were collected on a Setaram Setsys Evolution TGA instrument. The sample was heated under Ar from 20 ^oC until 800 ^oC at 10 K per minute. SAXS data was taken on beamline I22 at Diamond, using a Pilatus P3-2M detector, with 12.4keV X-rays, and a 6 m sample to detector distance, which gave a Q range of 0.003-0.35 $Å^{-1}$. The powder samples were held between two pieces of Kapton tape. Data was reduced using the DAWN small angle scattering pipeline, calibrated against silver behenate to obtain Q, and the background scattering from the Kapton tape subtracted prior to analysis.

For Brunauer-Emmet-Teller (BET) measurements on a Quantachrome Autosorb-1, each sample was degassed under vacuum at 120°C until the no further degassing was observed (ca 24 h). Using nitrogen as the adsorbing gas at -196 ^oC (77 K), an 80 point physisorption analysis was undertaken and the data analysed by the DFT method. The models used was N_2 at 77 K on carbon (slit pore, NLDFT equilibrium model). The surface area of the samples was calculated using the BET method using a 5-point analysis.

7.2.3 Procedure for Film Carbonization

A solution of 1 mg cm^{-3} PIM-EA-TB in chloroform was prepared and then deposited onto the ITO electrode by drying under ambient conditions. Carbonization of the PIM-EA-TB powder or film was performed at 500 ^{o}C for 3 h under vacuum (Edwards oil pump) in a custom-made quartz tube to fit the furnace (TSH12, Elite Thermal Systems Ltd.).

7.3 Results and Discussion

7.3.1 cPIM Film Electrodes I.: Formation and Characterisation

The PIM-EA-TB material (reference here as PIM) was obtained in powder form and dissolved in chloroform for casting of films on tin-doped indium oxide (ITO) coated glass substrates. Both powder and films were carbonized under vacuum at 500℃ in a quartz tube and for 3 h. Figure 7.2A shows scanning electron micrographs with the morphology of the original PIM powder (white) exhibiting agglomerated particles typically 80-300 nm in diameter. After vacuum heat treatment at 500℃, the carbonized PIM (cPIM) appears visually black but has retained particle diameter and morphology (Fig.7.2B). Similarly, thin transparent and colourless PIM films cast on ITO (Fig.7.2C) are carbonised to thin black hetero-carbon cPIM membranes (Fig.7.2D) with typically 1-2 μm thickness. Raman spectroscopy (532 nm excitation) reveals the associated structural changes with PIM exhibiting an underlying fluorescence and characteristic peaks (Fig.7.2E), whereas cPIM samples show no fluorescence and typical broad peaks at 1380 cm^{-1} (D-peak, disordered amorphous carbon) and at 1600 cm^{-1} (G-peak, graphitic carbon)[35] (see Fig.6.2F). SAXS analysis of the powder samples before and after carbonization suggest the sample contains features with a Guinier radius of gyration of 26 nm, in both cases (Fig.7.2G). If a spherical geometry is assumed, this corresponds to a radius around 34 nm.

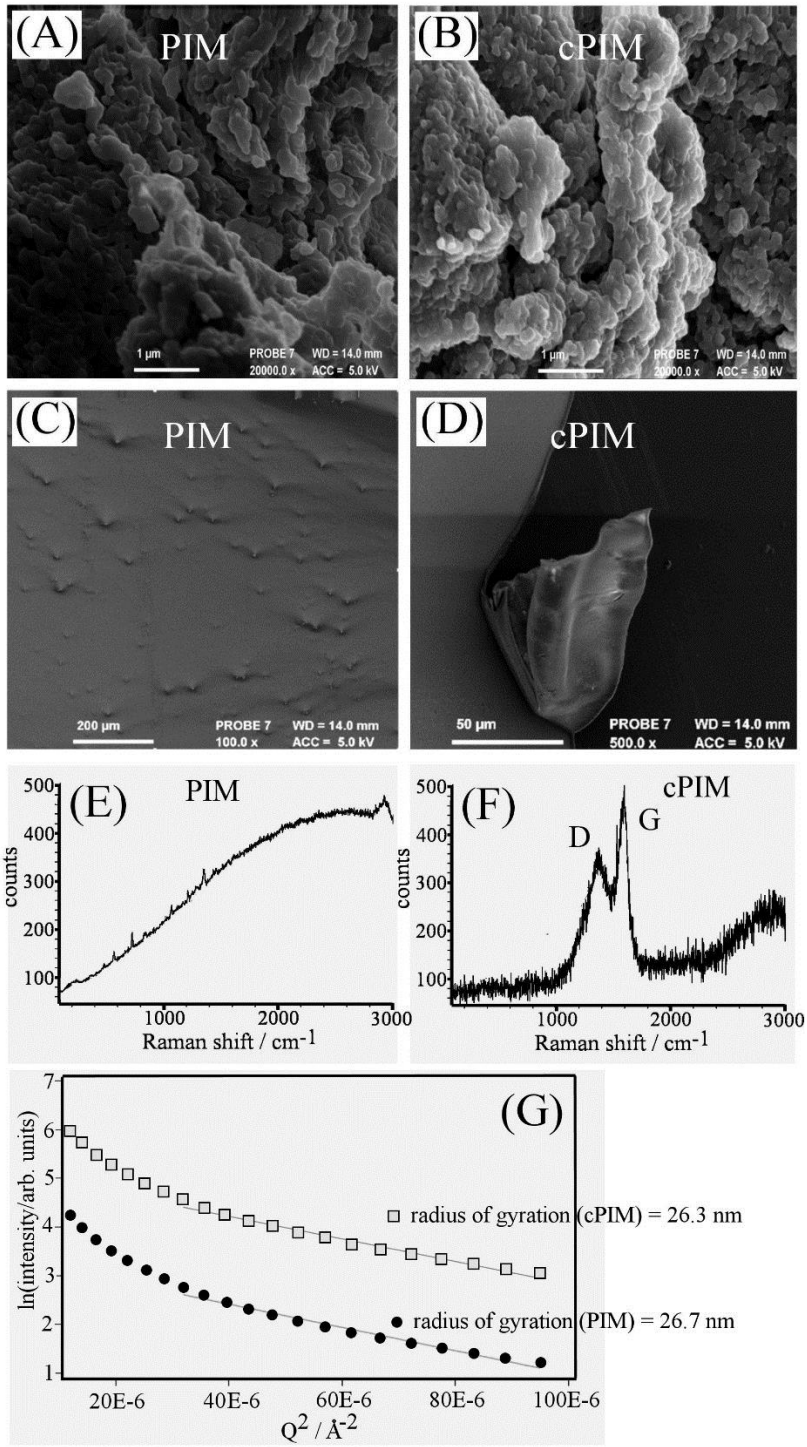

Figure 7. 2. FESEM images of (A) PIM powder (B) cPIM powder after 3h carbonization. (C) FESEM images of PIM film and (D) cPIM film on ITO after 3 h carbonization. (E) Raman spectra for PIM powder and (F) for cPIM powder. (G) SAXS data for PIM and cPIM powder samples.

In order to explore the changes in electrical conductivity going from PIM to cPIM material, films were prepared on a glass slide (60 μg cm^{-2}). Four-point probe measurements reveal no evidence for electrical conductivity for the PIM film but Ohmic conductivity for the cPIM film (resistivity 40 MΩ/square). This value for a ca. 1-2 μm thick film is six orders of magnitude lower compared to the typical conductivity of the ITO layer and therefore consistent with low electrical conductivity (*vide infra*).

Further insight into the elemental composition after carbonisation is obtained from XPS analysis (Fig.7.3). The survey scan for PIM polymer reveals the presence of nitrogen (mainly 399 eV for sp^2-type nitrogen with a shoulder at 401 eV for protonated or alkylated nitrogen[36]) and of carbon (mainly 285 eV for C-C and C-H). In terms of atom% ratios the material shows C: N: O 91.9: 6.56: 1.54, consistent with 7 atom% nitrogen (in approximate agreement with the molecular structure in Fig.7.1).

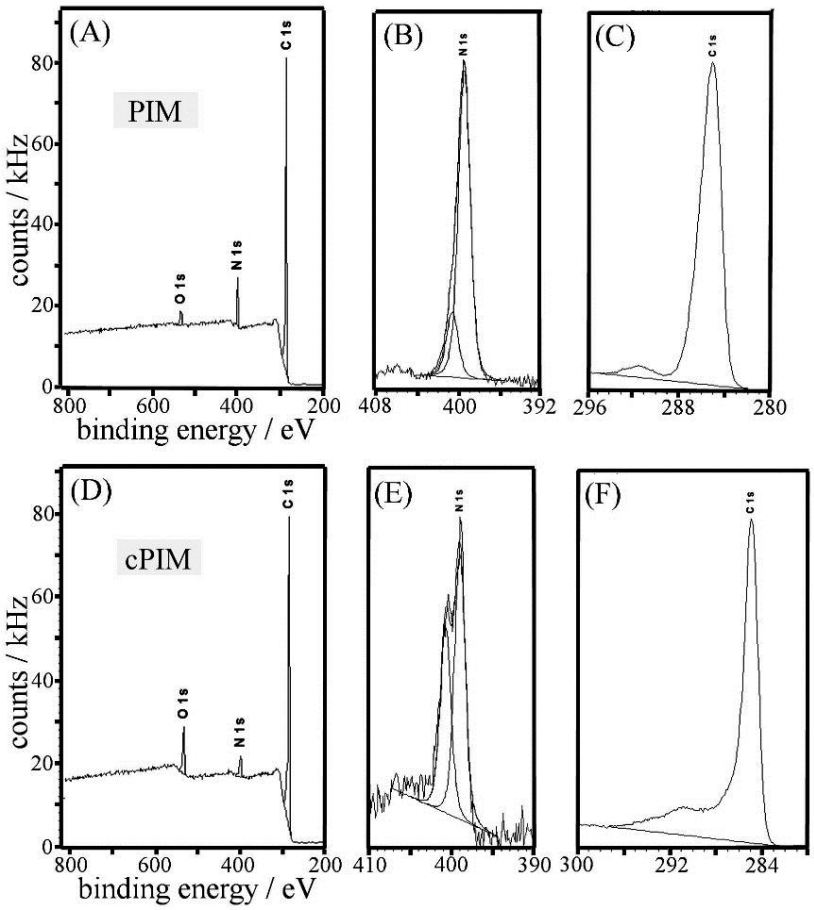

Figure 7. 3. XPS survey data, the N1s region, and the C1s region for PIM (A, B, C) and for cPIM (D, E, F).

After carbonisation, the cPIM material shows oxygen, nitrogen, and carbon components in the survey XPS scan (Fig.7.3D). The carbon 1s signal has changed only little (dominated by C-C/C-H), but the nitrogen signal now shows a clear split with more nitrogen being protonated or alkylated. The additional oxygen signal is likely to emerge from post-carbonisation reaction with air. The atom% ratio for C: N: O is now 89.8:4.44:5.76, which is indicative of only a minor loss of nitrogen, if any. The reaction scheme in Fig.7.1 could be a realistic description of the cPIM molecular structure evolution. The BET adsorption isotherm and pore size analysis (see Fig.7.4) confirm the retention of the rigid backbone structure during carbonisation of PIM powder.

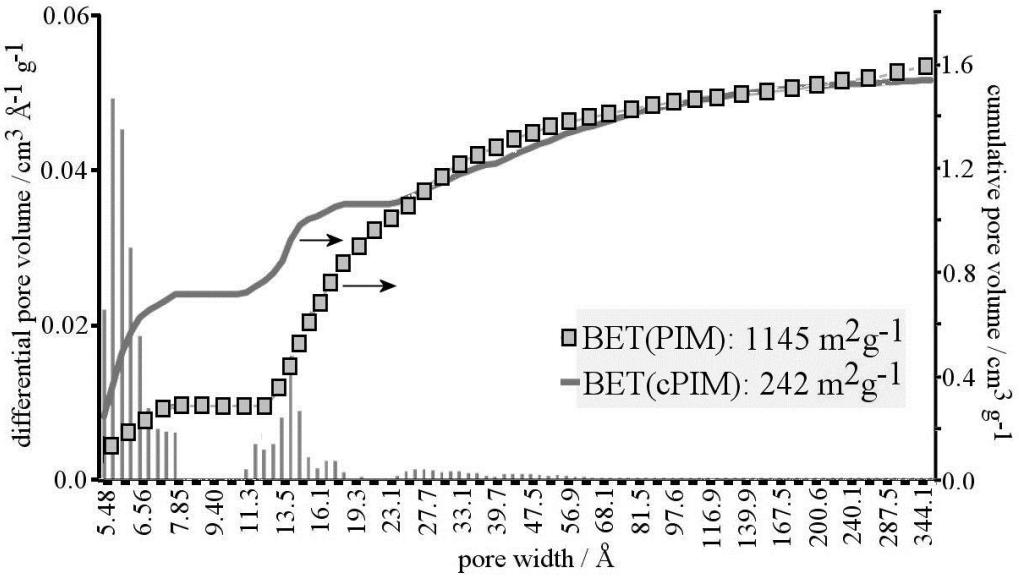

Figure 7. 4. Plots of data from the 80-point BET pore size analysis (N_2, 77K, slit pore NLDFT equilibrium model[37]) showing dominant pore sizes around 5.5 Å. A comparison of the cumulative pore volume for PIM (squares) and for cPIM (line) shows the switch from mesopores in PIM to micropores in cPIM.

The pore size analysis for cPIM powder shows a dominant pore size at ca. 5.5 Å or micropores responsible for half of the cumulative pore volume. A comparison to data for the PIM starting material (Fig.7.4) shows that the total cumulative pore volume has been retained (consistent with minimal morphology changes) but mesopores of ca. 14 Å size have been converted to the smaller micropores (due to crosslinking of polymer chains, see Fig.7.1). The BET volume in cPIM is reduced to 242 m^2g^{-1}. This value seems average (or even low) when compared for examples to novel graphene aerogel materials with up to an order of magnitude higher BET surface area[38]. However, for cPIM, the link from molecular precursor to 3D-carbon structure

and the absence of any templating agents are novel and potentially useful for the design of materials, for further optimization, or for the introduction of new functionalities.

7.3.2 cPIM Film Electrodes II.: Voltammetry and Capacitive Charging

Voltammetric characterisation of the cPIM film electrodes on ITO substrates was performed in aqueous buffer solution. In 0.1 M phosphate buffer pH 7 and in a potential range from 0.0 to 0.5 V vs. SCE, a well-defined capacitance response is observed (Fig.7.5A). Initially, for 15 μg and 30 μg films (thickness ca. ¼ or ½ μm) the capacitance scales linearly with the amount of cPIM deposit. However, for 60 μg and 120 μg the increase of capacitive current responses ceases, consistent with an "active thickness" (or a resistive diffusion layer thickness due to diffusion of either electrons or ions or both) of less than 1 μm. For thicker film "charge diffusion" requires more time (*vide infra*). When exploring the effect of pH on the capacitive current, an interesting switch to considerably higher capacitance is observed at pH 2 (Fig.7.5B). In fact, the onset of this increase in capacitance is seen already at pH 7 in the lower region of the potential window and the capacitance increase is shifted by ca. 0.3 V for a change in pH from 7 to 2. This Nernstian shift clearly proves the presence of a proton uptake reaction associated with the increase in capacitive current (e.g. protonation of nitrogen sites in cPIM associated with reduction). The effect can be compared to the step in capacitance in acidic solution observed for example in mesoporous heterocarbon materials from gelatin carbonization with the help of a silica template[39]. This is a feature uncommon for carbon and usually more associated with surface functionalities and well-defined molecular structures[40,41].

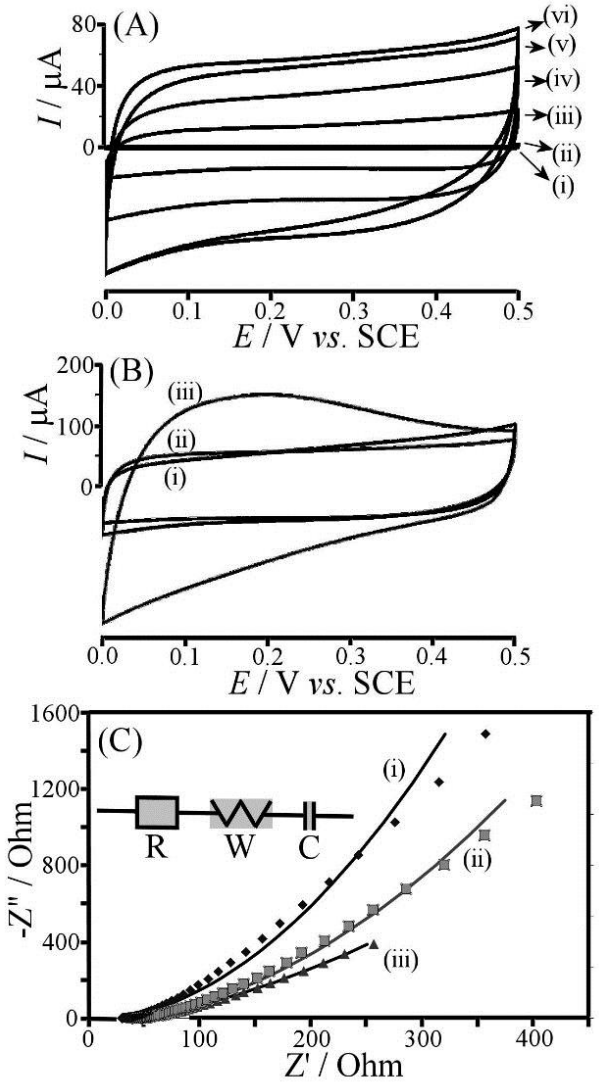

Figure 7.5. (A) Cyclic voltammograms (scan rate 50 mV s^{-1}) for different thicknesses of carbonized cPIM on ITO (with (i) bare ITO, (ii) 15 μg PIM, (iii) 15 μg cPIM, (iv) 30 μg cPIM, (v) 60 μg cPIM, and (vi) 120 μg cPIM) immersed in aqueous 0.1 M phosphate buffer pH 7. (B) As in A, but for 60 μg carbonized cPIM in 0.1 M phosphate buffer at (i) pH 12, (ii) pH 7, (iii) pH 2. (C) Nyquist plots for impedance data (0.0 V vs. SCE bias; 10 kHz to 0.1 Hz; 20 mV amplitude) for a 60 μg cPIM film immersed in 0.1 M phosphate buffer at (i) pH 12, (ii) pH 7, and (iii) pH 2.

Further study of the electrochemical impedance responses (Fig.7.5C) reveals characteristics consistent with those observed in cyclic voltammetry. A bare ITO electrode is observed to give a response consistent with an RC equivalent circuit (not shown) with R = 114 Ohm and C = 28 μF. The resistance R is dominated by the ITO sheet resistance, which is decreased during the vacuum heating process. After carbonization, when investigating a 60 μg cPIM film on ITO different types of responses are recorded at pH 12, 7, and 2. All of these are consistent with an

RWC equivalent circuit (see Fig.7.5C) revealing some "charge diffusion" as well as a capacitive element dominating at very low frequencies (see Table 7.1). At pH 2 the capacitance can be extrapolated to 8.8 mF for 60 μg cPIM equivalent to an approximate "supercapacitance" of 146 Fg^{-1}. This estimated value is linked to the high microporosity of the material and the Faradaic current component with proton uptake and can be compared for example to typical graphene nanoribbon materials[42], which exhibit typically 15 Fg^{-1}. Further improvements in "supercapacitance" and conductivity are likely to be achievable with further optimization of the carbonization process, although future application of the cPIM material are probably more likely in sensing or in mixed ion/electronic conductors.

Table 7. 1. Summary of impedance data for cPIM film electrodes on ITO substrates immersed in 0.1 M phosphate buffer pH 2, 7, and 12.

	R / Ohm	W / Ohm	C / mF
Bare ITO	114	-	0.028
cPIM pH 2	44	164	8.8
cPIM pH 7	44	262	2.0
cPIM pH 12	27	232	1.3

When investigating the electrochemical properties of cPIM films over a wider potential window additional features can be observed (Fig.7.6). With only PIM deposited (or a bare ITO) the reduction of ambient oxygen occurs with an onset at -0.2 V vs. SCE (Fig.7.6A). A much stronger oxygen reduction response is observed for a 15 μg cPIM film on ITO, but this can be traced back to the vacuum heat treatment activation of the underlying ITO substrate[43–45] (*vide infra*). The resulting reduction current of ca. 40 μA is consistent with ambient oxygen at the ITO substrate. When increasing the cPIM layer thickness (see Fig.7.6C) the capacitive current response increases, but the Faradaic current for oxygen reduction remains. Additional experiments were conducted with hydrogen peroxide, H_2O_2 (Fig.7.6D-F). The current for the reduction of H_2O_2 is observed at bare or PIM coated ITO as well as at the cPIM coated ITO. The current response is not diffusion controlled and therefore incomplete reduction occurs in

this potential range. Comparison of data with/without cPIM film suggests again that the carbonised polymer is not reactive and that the underlying ITO substrate is where the reduction occurs instead.

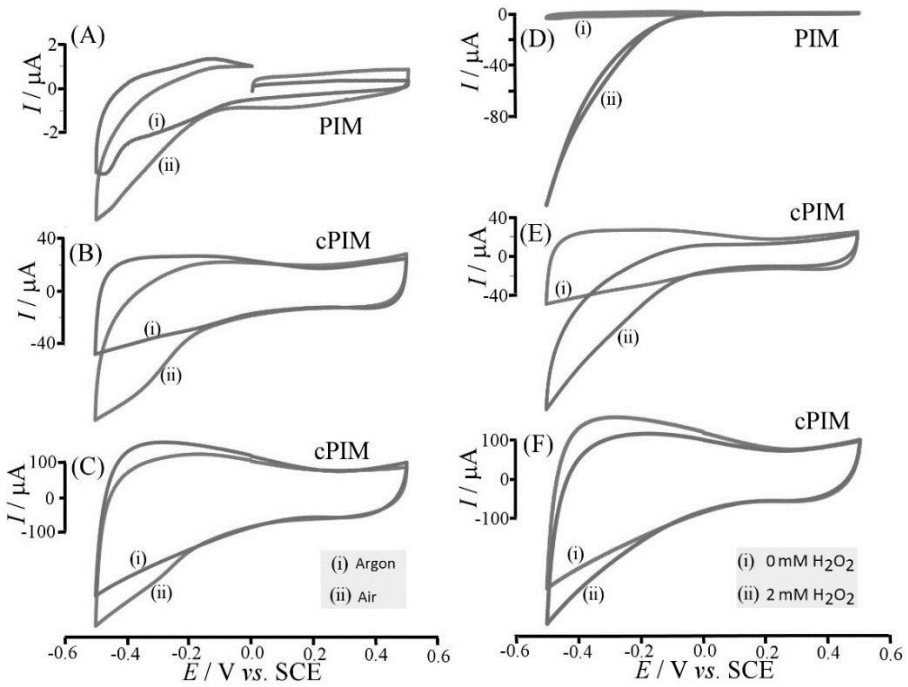

Figure 7. 6. (A,B,C) Cyclic voltammograms (scan rate 50 mVs^{-1}; (A) 15 μg PIM on ITO; (B) 15 μg cPIM on ITO; (C) 60 μg cPIM on ITO) in 0.1 M phosphate buffer pH 7 (i) in the absence and (ii) in the presence of air/oxygen. (D,E,F) as above, but for (i) 0 mM and (ii) 2 mM H_2O_2.

7.3.3 cPIM Film Electrodes III.: Oxygen Reduction and Scanning Electrochemical Microscopy

It appears that the cPIM material, although exhibiting an extremely high surface area and electrochemical reduction with insertion of protons, is not able to directly transfer electrons to oxygen or to hydrogen peroxide. This effect can be further demonstrated by scanning electrochemical microscopy (SECM[46,47]) employing a platinum microelectrode tip to measure the formation of hydrogen peroxide during oxygen reduction (Fig.7.7). The currents observed at bare ITO or cPIM coated ITO in nondeaerated phosphate buffer solution appear very similar in the second and following potential cycles (In the first potential cycle cPIM-coated ITO exhibits a stronger signal possibly due to some oxygen adsorption, see Fig. 7.7Bi). However,

the corresponding tip current signals (proportional to H_2O_2 concentration over the sample surface) reveal a lower signal in the presence of the cPIM film as well as a hysteresis/lag in the maximum H_2O_2 current. Therefore the oxygen reduction at the underlying ITO substrate does produce some hydrogen peroxide that is released more slowly through the cPIM film with a delay induced by slow diffusion through the film of carbonised carbon. This result confirms the very slow rate of electron transfer for both molecular oxygen and H_2O_2 in contact to microporous cPIM under reducing conditions. This effect is most likely due to the absence of reactive sites for electron transfer in cPIM. The unusual current 'crossing' of the current over bare ITO (line (i) in Fig. 7.7C) is likely to be associated with a surface reactivity change at the ITO electrode when scanning the potential more negative.

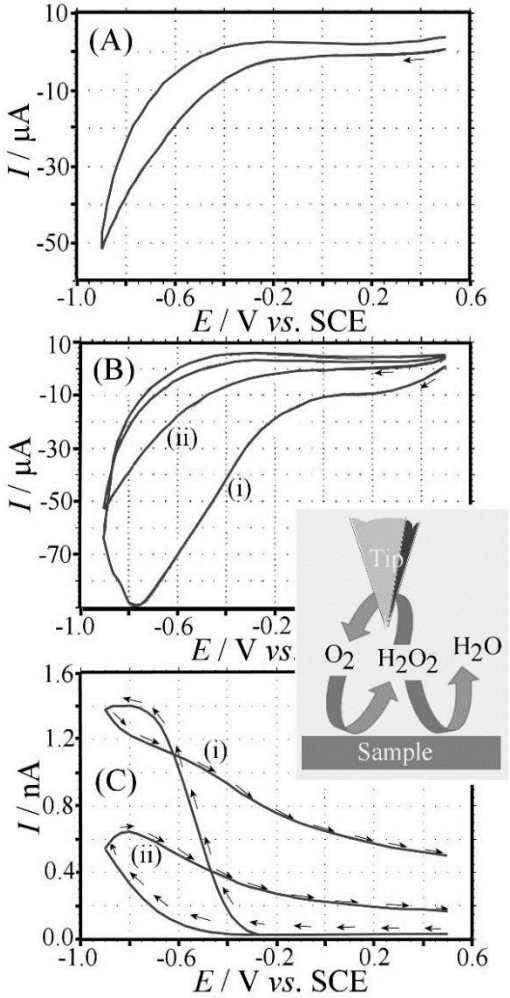

Figure 7. 7. Scanning electrochemical microscopy (SECM, scan rate 50 mVs^{-1}, tip potential 0.6 V vs. SCE, tip distance ca. 5 µm) data for (A) an ITO electrode (area) in 0.1 M phosphate buffer pH 7, (B) a 60 µg cPIM coated ITO electrode (area, 1st (i) and 2nd (ii) potential cycle shown), and (C) the corresponding tip current for (i) bare ITO and (ii) cPIM coated ITO. Inset shows schematic drawing of the detection principle.

7.4 Conclusion

It is intriguing to find a high surface area hetero-carbon with a very high level of microporosity and "supercapacitive" charging, but without significant electron transfer reactivity towards oxygen or towards hydrogen peroxide. This combination of properties could be beneficial due to the destructive effects of the oxygen reduction reaction (and the resulting reactive oxygen species) on carbon electrode materials. Such behaviour may lead to suppressed carbon corrosion, for example for energy/charge storage devices operating in the presence of ambient oxygen.

More generally, it has been shown that the highly rigid polymer of intrinsic microporosity (PIM-EA-TB) can be carbonised under mild conditions without loss of morphology and with a switch from meso- to enhanced microporosity. The ability of this new material to undergo redox-driven proton insertion/expulsion (like a molecular conducting polymer[48]) while exhibiting capacitive charging (more like a carbon[49]) is of interest and could have important potential applications in sensing (for example in Chem-FETs[50]). Further work will be required for this new class of carbonised PIM materials, in particular to investigate the effects of charge diffusion rates, carbonisation temperature, molecular precursor structure, and dimensionality on the properties of resulting microporous hetero-carbons. The potential for combined electron/ion conductivity needs to be investigated, for example, to develop effective conductors for lithium-ion battery composites. New class of designer carbons combining conductivity, microporosity, and heteroatoms or functional groups could be beneficial in selective adsorbents or in electrochemical desalination processes.

7.5 References

1 K. Sakaushi and M. Antonietti, *Bull. Chem. Soc. Jpn*, 2015, **88**, 386–398.

2 M. Antonietti, N. Fechler and T. Fellinger, *Chem. Mater.*, 2014, **26**, 196–210.

3 L. Lux, K. Williams and S. Ma, *CrystEngComm*, 2015, **17**, 10–22.

4 H. Nishihara and T. Kyotani, *Adv. Mater.*, 2012, **24**, 4473–4498.

5 S. Zhang, K. Dokko and M. Watanabe, *Mater. Horizons*, 2015, **2**, 168–197.

6 S. Dutta, A. Bhaumik and K. C. Wu, *Energy Environ. Sci.*, 2014, **7**, 3574–3592.

7 A. Vuorema, M. Sillanpää, L. Rassaei, M. J. Wasbrough, K. J. Edler, W. Thielemans, S. E. C. Dale, S. Bending and D. Wolverson, *Electroanalysis*, 2010, **22**, 619–624.

8 S. Zhao, C. Wang, M. Chen, J. Wang and Z. Shi, *J. Phys. Chem. Solids*, 2009, **70**, 1256–1260.

9 P. S. Shuttleworth, V. Budarin, R. J. White, M. Gun, R. Luque and J. H. Clark, *Chemistry (Easton).*, 2013, **19**, 9351–9357.

10 F. Xia, M. Pan, S. Mu, M. D. Jones and D. Wolverson, *Electroanalysis*, 2012, **8**, 1703–1708.

11 G. Sun, B. Li, J. Ran, X. Shen and H. Tong, *Electrochim. Acta*, 2015, **171**, 13–22.

12 D. Yang, S. Chaudhari, K. P. Rajesh and J. Yu, *ChemCatChem*, 2014, **6**, 1236–1244.

13 S. D. Ahn, B. Mao, S. I. Pascu, A. Vuorema and J. M. Mitchels, *Electroanalysis*, 2014, **26**, 69–75.

14 K. Lawrence, F. Xia, R. L. Arrowsmith, H. Ge, W. Nelson, J. S. Foord, N. D. M. Evans, J. M. Mitchels, S. E. Flower, S. W. Botchway, D. Wolverson, G. N. Aliev, T. D. James, I. Pascu and F. Marken, *Langmuir*, 2014, **30**, 11746–11752.

15 L. Liu, L. Liao, Q. Meng and B. Cao, *Carbon N. Y.*, 2015, **90**, 75–84.

16 J. Yan, Q. Wang, T. Wei, L. Jiang, M. Zhang, X. Jing and Z. Fan, *ACS Nano*, 2014, **8**, 4720–4729.

17 T. E. Long, B. Voit and O. Okey, *Advances in Polymer Science*, Springer, Switzerland, 2013.

18 K. Qian, A. Kumar, H. Zhang, D. Bellmer and R. Huhnke, *Renew. Sustain. Energy Rev.*, 2015, **42**, 1055–1064.

19 A. Ramos, I. Camea and A. B. Garcua, *Carbon N. Y.*, 2013, **59**, 2–32.

20 J. Tang, J. Liu, N. L. Torad, T. Kimura and Y. Yamauchi, *Nano Today*, 2014, **9**, 305–323.

21 G. Harikrishnan, T. U. Patro and D. V Khakhar, *Carbon N. Y.*, 2007, **45**, 531–535.

22 L. Hao, X. Liu, J. Wang, C. Wang, Q. Wu and Z. Wang, *Talanta*, 2015, **142**, 104–109.

23 S. Gadipelli and Z. Xiao, *ChemSusChem*, 2015, **8**, 2123–2132.

24 A. Aijaz, N. Fujiwara and Q. Xu, *J. Am. Chem. Soc.*, 2014, **136**, 6790–6793.

25 A. J. Amali, J. Sun and Q. Xu, *Chem. Commun.*, 2014, **50**, 1519–1522.

26 Z. Li and L. Yin, *Nanoscale*, 2015, **7**, 9597–9606.

27 N. B. Mckeown and P. M. Budd, *Chem. Soc. Rev.*, 2006, **35**, 675–683.

28 R. W. Baker and B. T. Low, *Macromolecules*, 2014, **47**, 6999–7013.

29 S. Kim and Y. M. Lee, *Prog. Polym. Sci.*, 2015, **43**, 1–32.

30 N. B. McKeown and P. M. Budd, *Macromolecules*, 2010, **43**, 5163–5176.

31 Y. Wang, N. B. Mckeown, K. J. Msayib, G. A. Turnbull, I. D. W. Samuel and O. S. Centre, *Sensors*, 2011, **11**, 2478–2487.

32 F. Xia, M. Pan, S. Mu, R. Malpass-Evans, M. Carta, N. B. McKeown, G. A. Attard, A. Brew, D. J. Morgan and F. Marken, *Electrochim. Acta*, 2014, **128**, 3–9.

33 E. Madrid, P. Cottis, Y. Rong, A. T. Rogers, J. M. Stone, R. Malpass-evans, M. Carta, B. Mckeown and F. Marken, *J. Mater. Chem. A Mater. energy Sustain.*, 2015, **3**, 15849–15853.

34 M. Carta, R. Malpass-Evans, M. Croad, Y. Rogan, J. C. Jansen, P. Bernardo, F.

Bazzarelli and N. B. McKewon, *Science (80-.).*, 2013, **339**, 303–307.

35 A. C. Ferrari, *Solid State Commun.*, 2007, **143**, 47–57.

36 M. Shibata, Y. Kimura and D. Yaginuma, *Polymer (Guildf).*, 2004, **45**, 7571–7577.

37 B. S. Ghanem, R. Swaidan, E. Litwiller and I. Pinnau, *Adv. Mater.*, 2014, **26**, 3688–3692.

38 H. Wang, X. Yuan, G. Zeng, Y. Wu, Y. Liu, Q. Jiang and S. Gu, *Adv. Colloid Interface Sci.*, 2015, **221**, 41–59.

39 A. Olejniczak, M. Lezabska, A. Pacula, P. Nowak, J. Wloch and J. P. Lukaszewicz, *Carbon N. Y.*, 2015, **91**, 200–214.

40 P. Lin and F. Yan, *Adv. Mater.*, 2012, **24**, 34–51.

41 A. Janosevic, B. Marjanovic, A. Rakic and G. Ciric-Marjanovic, *J. Serbian Chem. Soc.*, 2013, **78**, 1633–1836.

42 M. S. Goh and M. Pumera, *Electrochem. commun.*, 2010, **12**, 1375–1377.

43 R. Latz, K. Michael and M. Scherer, *Jpn. J. Appl. Phys.*, 1991, **30**, 149–151.

44 P. Vacca, M. Petrosino, R. Chierchia, A. Guerra, C. Minarini and A. Rubino, *Macromol.Symp*, 2007, **247**, 333–339.

45 A. M. Collins, G. J. Blanchard and F. Marken, *Electroanalysis*, 2012, 246–253.

46 S. Amemiya, A. J. Bard, F. F. Fan, M. V Mirkin and P. R. Unwin, *Annu. Rev. Anal. Chem*, 2008, **1**, 95–131.

47 G. Nagy and L. Nagy, *Fresenius J Anal Chem*, 2000, **366**, 735–744.

48 C. Li, H. Bai and G. Shi, *Chem Soc Rev*, 2009, **38**, 2397–2409.

49 A. J. Gross and A. J. Downard, *Anal. Chem.*, 2011, **83**, 2397–2402.

50 W. Vonau and U. Guth, *J Solid State Electrochem*, 2006, **10**, 746–752.

Chapter 8: High-Utilization Nano-Platinum Catalyst (Pt@cPIM) Obtained via Vacuum Carbonization in a Molecularly Rigid Polymer of Intrinsic Microporosity

Chapter Abstract

Polymers of intrinsic microporosity (PIM or here PIM-EA-TB) offer a highly rigid host environment into which hexachloroplatinate (IV) anions are readily adsorbed and vacuum carbonized (at 500 °C) to form active embedded platinum nanoparticles. This process is characterised by electron and optical microscopy, AFM, XPS, and electrochemical methods, which reveal that the PIM microporosity facilitates the assembly of nanoparticles of typically 1.0-2.5 nm diameter. It is demonstrated that the resulting carbonized "Pt@cPIM" from drop-cast films of ca. 550 nm average thickness, when prepared on tin-doped indium oxide or ITO, contain fully encapsulated but also fully active platinum nanoparticles in an electrically conducting heterocarbon host. Alternatively, for thinner films (50-250 nm) prepared by spin-coating, the particles become more exposed due to additional loss of the carbon host. In contrast to catalyst materials prepared by vacuum-thermolyzed hexachloroplatinate(IV) precursor, the platinum nanoparticles within Pt@cPIM retain high surface area, electrochemical activity, and high catalyst efficiency due to the molecular rigidity of the host. Data are presented for oxygen reduction, methanol oxidation, and glucose oxidation and in all cases the high catalyst surface area is linked to excellent catalyst utilization. Robust transparent platinum-coated electrodes are obtained with reactivity equivalent to bare platinum but with only 1 μg Pt cm^{-2} (i.e. ~ 100% active Pt nanoparticle surface is maintained in the carbonised microporous host).

Graphical Abstract:

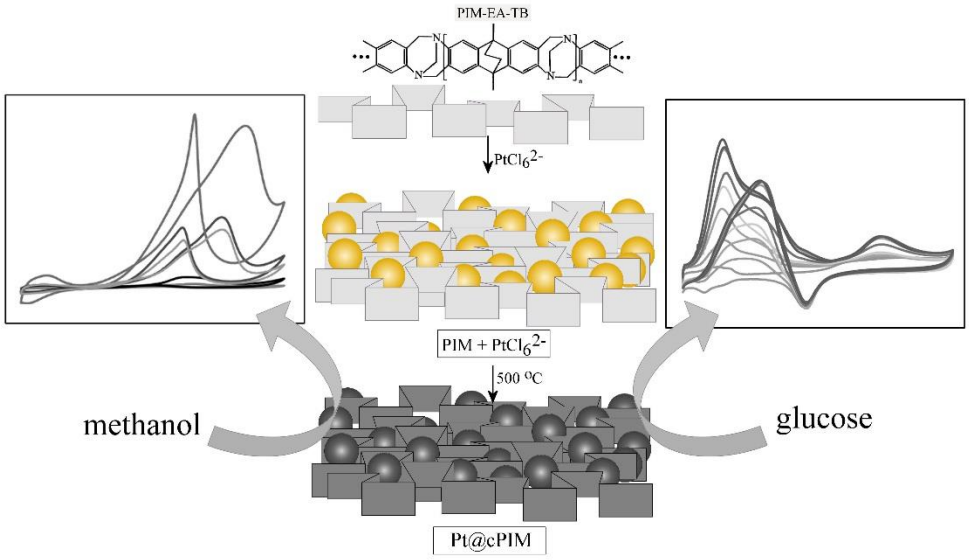

Chapter Publications

This chapter is under review:

Y. Rong, D. He, R. Malpass-Evans, M. Carta, N. B. McKeown, M. F. Gromboni, L. H. Mascaro, G. W. Nelson, J. S. Foord, P. Holdway, S. E. C. Dale, S. Bending, and F.Marken, *ACS Applied Surfaces and Interfaces.*

Acknowledgement

I would like to thank Dr. Sara Dale for her help in AFM images and thank Dr. Philip Holdway for his help in XPS measurements.

8.1 Introduction

The preparation and formulation of catalysts for applications in fuel cells[1] and in sensors[2] remain a highly active research topic. For example, the development of new types of porous substrate materials[3] offer catalysts with (i) better levels of performance[4,5], (ii) improved access into a wide range of reproducible and highly efficient catalyst composites[6], and/or (iii) access to more sustainable catalyst systems[7]. Many new inorganic[8] or carbon-based catalyst composite materials[9,10] are under development and, in particular, synthetic methods based on the carbonization of precursors to yield carbon-embedded catalysts[11,12] have proved beneficial. Novel and highly efficient types of carbon-embedded platinum catalysts have been obtained via carbonization. However, directly embedding active nano-platinum catalysts without loss of activity during carbonization in a one-step procedure is uncommon and desirable.

Platinum nanoparticles are the basis for the overwhelming majority of technical catalyst systems due to the durability of platinum and due to the special place platinum takes with respect to interfacial adsorption of reaction intermediates. Platinum nanoparticles are employed in PEM fuel cells[13], in methanol[14] and glucose[15] driven fuel cells, but also in many dye-sensitised solar cells[16] and in electrolysers for energy conversion[17]. The most active size range for platinum has been reported to be 2-6 nm (based on mass activity)[18]. However, the catalyst durability and corrosion characteristics are also important[19]. We have recently demonstrated that a new class of polymers with intrinsic microporosity (PIMs) can be employed to stabilise Pt nanoparticle performance for both anode and cathode activity[20,21].

Platinum nanoparticles provide very effective catalysts but suffer from high cost of the non-sustainable noble metal catalyst. Therefore, intense research efforts are directed towards either replacing platinum with cheaper and more sustainable metals (e.g. based on alloys of Fe, Co, Ni, etc[22].) or improving utilisation. The latter involves maximising the surface area and reactivity of platinum, for example, by embedding nanoparticles into porous hosts or substrates. Porous polymer materials are emerging as promising substrates (or precursors for porous substrates[23]) for the immobilisation and growth of platinum nano-catalysts[24]. Highly porous polymer structures that can retain microporosity during carbonization are particularly interesting. For PIM materials it has been suggested that carbonization occurs via cross-linking and without breaking the of the rigid polymer backbone strands[25].

Polymers of intrinsic microporosity (or PIMs[26]) exhibit micropore diameter of typically 0.5-2.0 nm and N_2-adsorption surface area values up to 1000 m^2g^{-1}. [27] They were originally developed for gas storage[28] and separation[29], but recently have also proven utility for electrochemical processes such as electrocatalysis[30], ionic devices[31], or electroanalysis[32]. Most work in PIM electrochemistry to date has been carried out with PIM-EA-TB (prepared from a diaminoethanoanthracene monomer polymerised via a Tröger base "TB" coupling; see structure in Fig.8.1). This polymer with highly rigid molecular structure exhibits N_2-adsorption surface area of 1024 m^2g^{-1} and is employed here with molecular weight of 70 kDa[30].

We have demonstrated previously that relatively gentle vacuum carbonization of PIM-EA-TB at 500 °C causes conversion of the microporous starting material into a microporous conducting hetero-carbon[25]. Although the electrical conductivity of the new carbon material was limited, thin films deposited onto tin-doped indium oxide (ITO) substrates were clearly capacitive and suitable for application as high surface area carbon film electrodes. A key feature in the conversion of PIM-EA-TB to the carbonized form (cPIM) is the retention of structural porosity/integrity. There were no changes in cumulative pore volume and no apparent changes in morphology upon vacuum carbonization[25]. Therefore, this hetero-carbon formation may offer ideal conditions for the co-formation/embedding of nano-catalysts with the following advantages: (A) the rigid PIM-EA-TB does not block/affect the catalytically active Pt particle surface and (B) after carbonization, porosity and connectivity are maintained to allow electrical contact and sufficient access for reactants to the active catalyst surface.

Here, we add a well-defined amount of platinum pre-cursor ($PtCl_6^{2-}$) by absorption into the porous protonated form of PIM-EA-TB and during subsequent vacuum carbonisation nano-particulate platinum is formed *in-situ* and without encapsulation or blocking of the active catalyst surface (Fig.8.1). The microporous hetero-carbon host surrounding the platinum nano-catalyst ensures good electrical connection and therefore excellent catalyst utilisation.

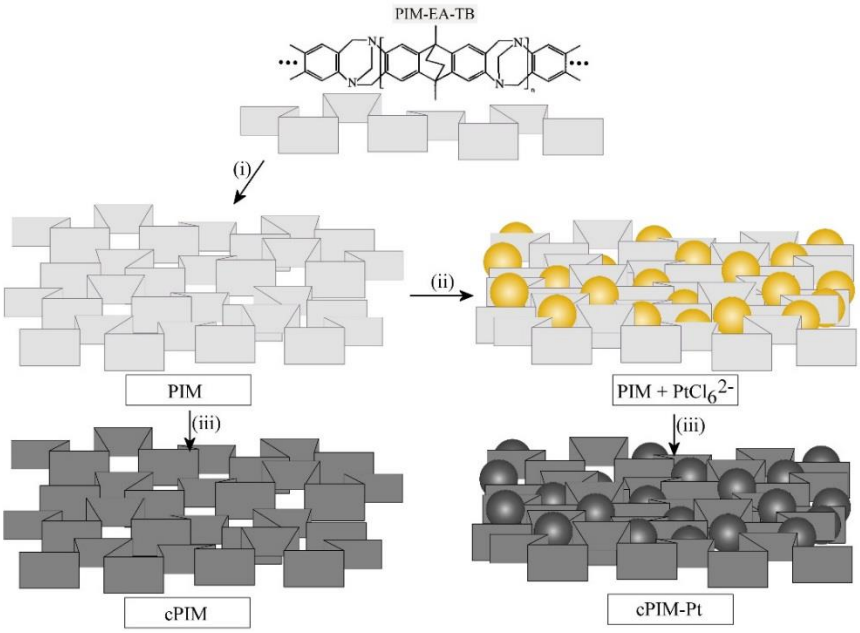

Figure 8.1. Schematic representation of (i) the formation of a film of PIM-EA-TB, (ii) absorption of $PtCl_6^{2-}$ into the film, and (iii) vacuum carbonisation at 500 °C to give highly porous hetero-carbon materials with/without nano-platinum catalyst.

It is shown that PIM-EA-TB as a precursor host material can be employed to generate/maintain platinum nanoparticle size (at typically 1.0-2.5 nm) and to improve nano-catalyst performance by building up thicker layers of catalyst (with additive performance). Catalysts are prepared in a simple one-step vacuum carbonization process in which the PIM-EA-TB polymer is converted into an electrically conducting host (of similar porosity) containing the platinum nanoparticle catalyst in a way that it is accessible to the solution phase. In contrast to solution casting, spin-coating produces very thin films which, when carbonized, give highly effective platinum catalyst layers on transparent tin-doped indium oxide (ITO) electrode surfaces.

8.2 Experimental

8.2.1 Chemical Reagents

Dipotassium platinum(IV)hexachloride, D-(+)-glucose, phosphoric acid (85%), sodium hydroxide, perchloric acid (96%), sodium chloride and chloric acid (30%) were purchased from Aldrich or Fisher Scientific and used without further purification. Carbonized PIM-EA-TB was

prepared following the literature recipe[33]. All solutions were prepared using deionized water (resistivity 18 MOhm cm at 22 °C) from a Thermo Scientific water purification system.

8.2.2 Instrumentation

Heating was performed in a TSH12 tube furnace (Elite Thermal System Ltd.). Pt nanoparticle materials were characterised by transmission electron microscopy (TEM) on a Jeol 1200EXII TEM system (with EDS and STEM). All electrochemical measurements were performed using an Ivium Compactstat potentiostat (The Netherlands) with platinum wire counter electrode and KCl-saturated calomel reference electrode (SCE, Radiometer REF401). The working electrode was prepared from ITO coated glass (tin-doped indium oxide films sputter-coated onto glass, active area 15 mm × 15 mm, resistivity ca. 15 Ω per square) obtained from Image Optics Components Ltd (Basildon, Essex, UK). XPS data were obtained on a Kratos Axis Ultra DLD system using a fixed anode monochromatic Al Kα X-ray source operating at 120 W.

8.2.3 Preparation of Thick Film Pt@cPIM on Tin-Doped Indium Oxide (ITO)

An aqueous platinum precursor solution was prepared by dissolving 10 mM K_2PtCl_6 in 0.5 M HCl (this solution was unstable as indicated by a slow colour change from yellow to orange and therefore stored in the dark at 4 ºC). A tin-doped indium oxide (ITO) electrode was coated with 60 μL (1 mg/mL in chloroform) PIM-EA-TB in a drop-cast process giving approximately 550 nm thick deposits. Next, the ITO with PIM-EA-TB layer was dipped into the platinum precursor solution for 5 minutes (to allow sufficient time for ion exchange), then rinsed with water, and dried under ambient conditions. The colour changed from clear to yellow. After the $PtCl_6^{2-}$ impregnation step, the ITO electrode was subjected to vacuum carbonisation under oil pump vacuum (ca. 0.1 mTorr) in a quartz tube to fit the tube furnace at 500 ℃ for 3 h to obtain cPIM-Pt with embedded platinum nanoparticles. Elemental analysis (Butterworth Analytical Laboratories, London) was performed for two samples: (A) for PIM-EA-TB treated with $Pt(IV)Cl_6^{2-}$: Pt 6.8% C 55.5% H 5.2% N 6.2% and (B) for cPIM-Pt: Pt 10.2% C 72.4% H 2.1% N 5.7%. Residual mass is likely to be associated here with inorganic components such as KCl. Note that in the ratio of platinum atoms to nitrogen atoms in PIM-EA-TB treated with

$Pt(IV)Cl_6^{2-}$ is 0.08 (or 8%), which suggests that only partial loading of the polymer was achieved.

8.2.4 Preparation of Thin Film Pt@cPIM on Tin-Doped Indium Oxide (ITO)

PIM-EA-TB was dissolved in chloroform to prepare solutions with four different concentrations (0.25%, 0.5%, 1% and 2% wt.). Spin-coating of these solutions (WS-650Mz-23NPP (Laurell Technologies) using a rotation rate of 1500 rpm for 1 minute and ITO substrates of 15 mm × 15 mm area resulted in different thicknesses of PIM-EA-TB (*vide infra*). Next, the coated electrode was immersed into the platinum precursor solution (as before) for 5 minutes, then rinsed with water and dried under ambient conditions. Then the ITO electrode was transferred to vacuum carbonisation under oil pump vacuum (ca. 0.1 mTorr) in a quartz tube at 500 ℃ for 3 h to give cPIM-Pt thin films with platinum nanoparticles embedded.

8.3 Results and Discussion

8.3.1 Formation and Characterisation of Thick Film Pt@cPIM

Drop-casting was employed with 60 μL of a PIM-EA-TB solution in chloroform (1 mg/mL) applied to an ITO electrode. With the measured film density of 1.1 g cm^{-3} for PIM-EA-TB[34], this allows an average film thickness to be estimated as 550 nm. With platinum bound into the film (see elemental analysis results in the experimental section) a coverage of about 6 μg Pt cm^{-2} is anticipated. Under $PtCl_6^{2-}$ absorption conditions employed here only approximately 8% of the nitrogen atoms in the polymer are associated with a platinum. The vacuum carbonization process when applied to a film of PIM-EA-TB on an ITO substrate is known to produce a nitrogen-containing hetero-carbon with significant electrical conductivity, the characteristic Raman signature for a graphitic structure, retained cumulative pore volume/morphology and the black coloration of carbon[25]. The N_2 adsorption data for PIM-EA-TB suggests a surface area of 1027 m^2 g^{-1} before carbonization and 242 m^2 g^{-1} after carbonization[25].

Here, PIM-EA-TB only is vacuum carbonized to give cPIM and with absorbed $PtCl_6^{2-}$ into the porous structure to give Pt@cPIM. Figure 8.2 shows transmission electron micrographic (TEM)

evidence for the presence of cPIM carbon material and for the embedded Pt nanoparticles in cPIM-Pt (contrast Fig.8.2A and 8.2B). Higher magnification (Fig.8.2D) allows individual particles to be analysed and the average particle size to be estimated as typically 1.0-2.5 nm. This value is in good agreement with the micropore size for the PIM-EA-TB polymer starting material (from N_2 gas adsorption isotherm data[31]). Electron diffraction data (Fig.8.2E and 8.2F) clearly confirm that the carbonization process leads to inclusion of platinum nanoparticles. The diffraction rings are consistent with Pt(331), Pt(222), Pt(311), Pt(220), Pt(200), and Pt(111) (compare JCPDS 4-0802 structure information[35]).

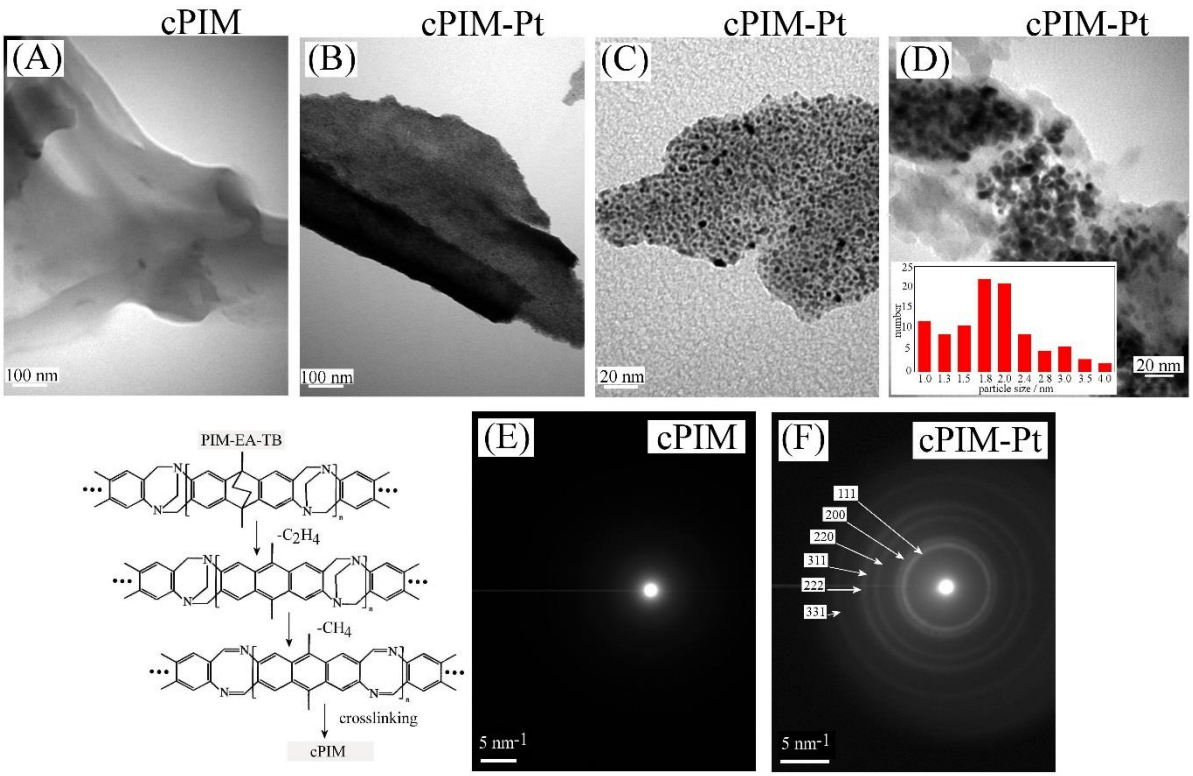

Figure 8. 2. Transmission electron micrographs for (A) thick cPIM, (B) thick cPIM-Pt, (C) thick cPIM-Pt, and (D) thin film cPIM-Pt with particle size analysis. Also shown is a schematic reaction pathway for carbonisation and diffraction pattern for (E) cPIM and (F) cPIM-Pt.

8.3.2 Formation and Characterisation of Thin Film Pt@cPIM

When employing spin-coating instead of drop-casting, better defined coatings of PIM-EA-TB can be produced. By changing the wt% or PIM-EA-TB in chloroform and keeping the spin coating conditions constant (see experimental) film thickness can be varied from about 50 to 250 nm (based on AFM cross-sectional data, see Fig.8.3D). These films are much more uniform compared to deposits formed by drop-casting. AFM images of bare ITO and cPIM

coated ITO are shown in Figure 8.3A and 8.3B consistent with a uniform coating. Perhaps surprisingly, when $PtCl_6^{2-}$ is absorbed into the PIM deposit prior to vacuum-carbonization, the morphology is affected and only much thinner deposits seem to remain (see Fig.8.3C). This observation is confirmed by SEM imaging.

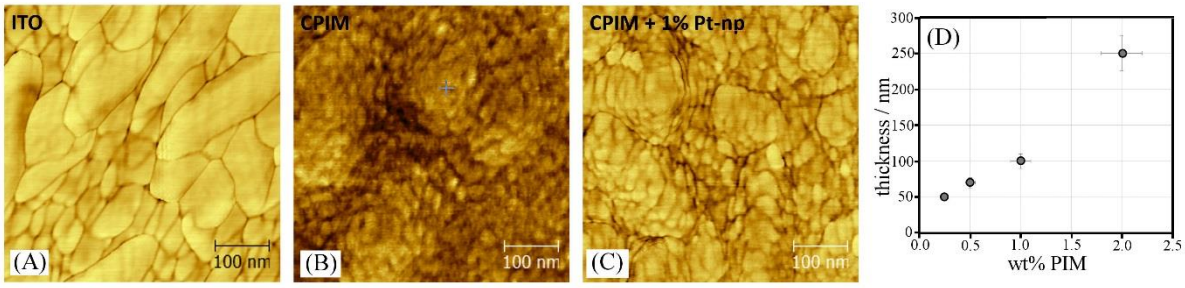

Figure 8. 3. Atomic force microscopy (AFM) images for (A) bare ITO, (B) cPIM-coated (1 wt%) ITO, and (C) cPIM-Pt (1 wt%) coated ITO. (D) Plot of cross-sectional height data for 0.25 wt%, 0.5 wt%, 1 wt%, and 2 wt% PIM-EA-TB in chloroform employed for spin coating.

Figure 8.4 shows both cross-sectional and morphological SEM images for different types of spin-coated PIM deposits on ITO. The PIM film in Fig.8.4A is formed from 1 wt% PIM in chloroform with an approximately 100 nm thin film clearly visible (containing $PtCl_6^{2-}$ as "stain"). Films of vacuum-carbonized PIM (without Pt) also form well-defined films (Fig.8. 4B). However, when exploring cross-sectional images of 1 wt% and 2 wt% PIM films with $PtCl_6^{2-}$ immobilised, it is apparent that a part of the carbon deposit is missing (removed by the vacuum carbonization process).

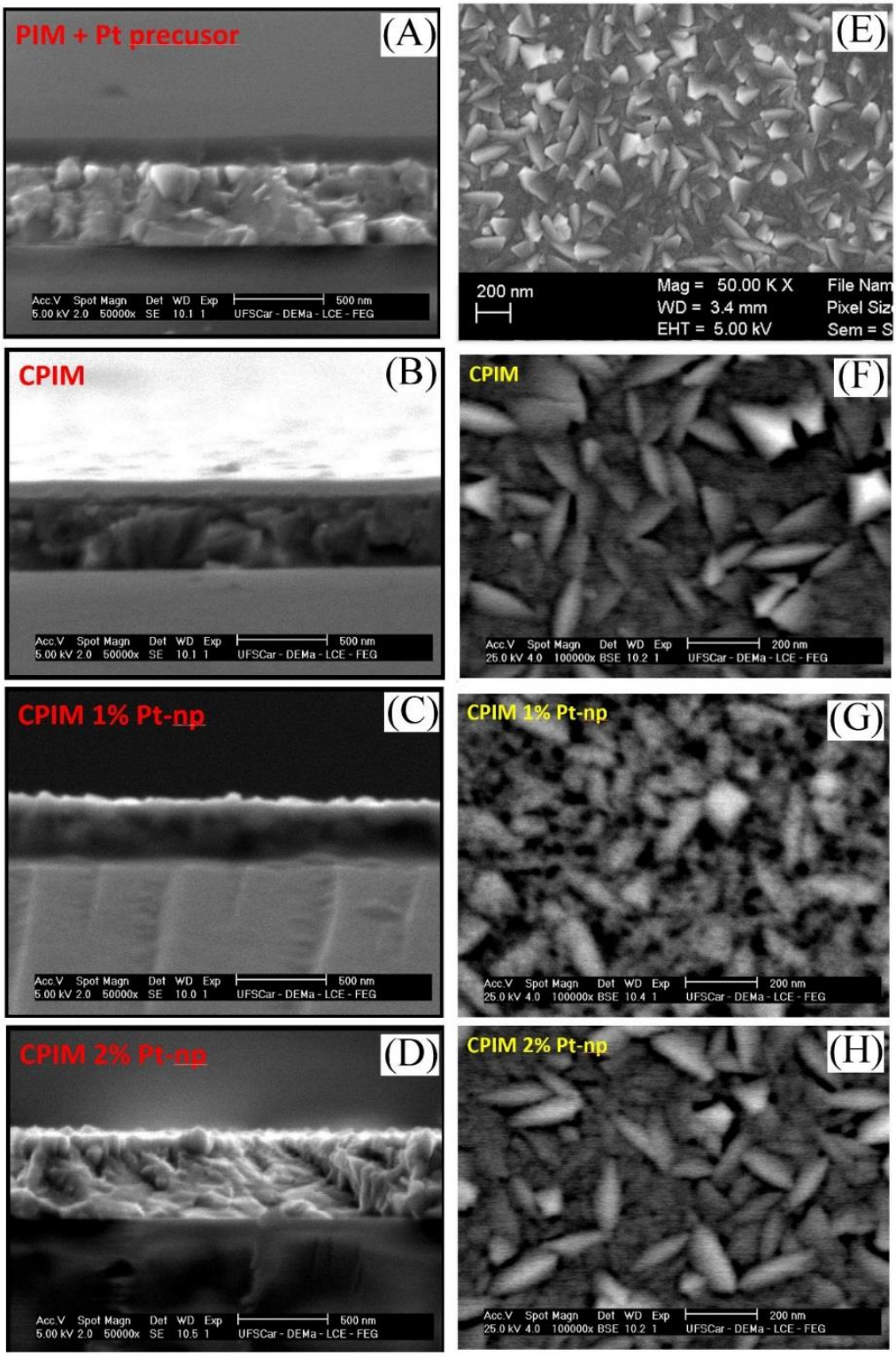

Figure 4. Cross-sectional scanning electron microscopy (SEM) images for (A) PIM-Pt (spin-coated from 1 wt%), (B) cPIM showing the carbonized film without platinum, (C) Pt@cPIM (spin-coated from 1 wt%), and (D) Pt@cPIM (spin-coated from 2 wt%). Loss of carbon material during carbonization for the platinum containing films is evident. Also shown are SEM images for (E) base ITO, (F) cPIM coated ITO, (G) Pt@cPIM (spin-coated from 1 wt%), and (H) Pt@cPIM (spin-coated from 2 wt%).

Additional morphological images (Fig. 8.4G and 8.4H) clearly show that platinum is present (as nano-structured deposit on top of the ITO crystals), but evidence for the amount of remaining cPIM substrate material is not clear. Next, XPS experiments were performed. Fig.8.5 shows survey data for PIM and PIM-Pt with the additional Pt signal clearly observed. After vacuum carbonization of a thin film of PIM-EA-TB (from 1 wt% solution), cPIM (Fig.8.5C) shows features identical to those reported recently[32]. The higher oxygen signals in cPIM compared to PIM are assigned to ingress and reactivity of oxygen after vacuum carbonization when the sample is exposed to the open atmosphere. Nitrogen is present after carbonization, but the level appears lower relative to that for carbon. For the Pt@cPIM film (Fig.8.5D) significant changes occur and signals from ITO are clearly evident (compared to Fig.8.5E). Carbon levels are higher compared to the bare ITO sample but lower when compared to the cPIM sample (Fig.8.5C). Characteristic Pt4f peaks are observed (see insets) with a splitting into 7/2 and 5/2 states. Binding energies for Pt4f in Fig.8.5B are consistent with the $PtCl_6^{2-}$ precurso[36]r and in Fig.8.5D with metallic platinum nanoparticles (see Table 1)[37].

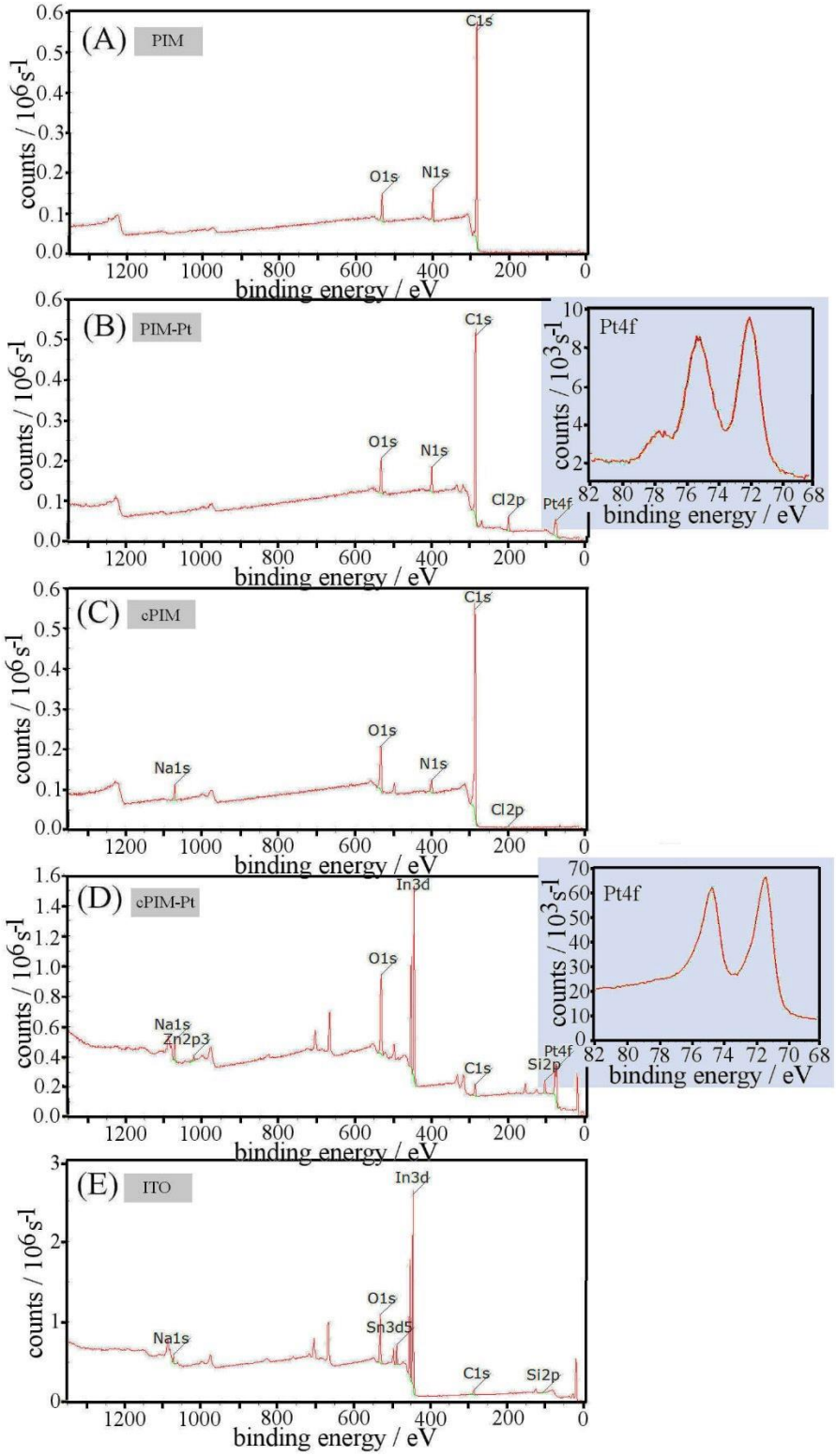

Figure 8. 5. XPS survey spectra for (A) PIM-EA-TB, (B) PIM-EA-TB with Pt precursor absorbed, (C) carbonised PIM, (D) carbonised PIM-EA-TB with Pt precursor, and (E) a bare ITO electrode substrate. Insets show Pt4f data for PIM-Pt and Pt@cPIM.

Table 1. Summary of XPS data for PIM-Pt and Pt@cPIM.

	PIM-Pt		Pt@cPIM	
Element	Peak / eV	At%	Peak / eV	At%
C1s	285.00 [a]	13.42	285.00 [a]	80.94
O1s	531.42	51.34	532.62	7.77
$Pt4f_{7/2}$	72.11	4.35	71.38	0.79

[a] the C1s binding energy was used as reference point with 285.00 eV.

It can be concluded that the vacuum carbonisation of thin film PIM is somewhat affected by the presence of $PtCl_6^{2-}$ (in part possibly due to the formation of volatile carbon halides) but that consistently platinum metal in the form of nanoparticles is formed. Even for the thin film Pt@cPIM deposits, there is remaining carbon to act as substrate and conductive support for the catalyst. The electrocatalytic reactivity of these materials is investigated next.

8.3.3 Electrocatalytic Oxygen Reduction

Platinum catalysts are employed widely in fuel cells and particularly in the oxygen reduction reaction[38], which provides an enormous challenge for sustainable production. The reduction of oxygen is reported to be associated mainly with (i) reduction of O_2 to a peroxide intermediate and (ii) further reduction to water (equation 8.1)[39].

$$O_2(aq) + 2\ H^+(aq) + 2\ e^-(m) \rightarrow H_2O_2(ads) \quad (8.1a)$$

$$H_2O_2(ads) \leftrightarrow H_2O_2(aq) \quad (8.1b)$$

$$H_2O_2(ads) + 2\ H^+(aq) + 2\ e^-(m) \rightarrow 2\ H_2O(aq) \quad (8.1c)$$

Recent work on PIM-EA-TB stabilised platinum catalysts in oxygen reduction processes has been reported where the platinum nanoparticles and the carbon substrate were "protected" against accelerated corrosion[21]. Here, platinum nanoparticles are embedded into a hetero-carbon host with sufficient porosity to allow reagent access to the catalyst and with sufficient electrical conductivity to allow effective potential control. Fig.8.6A shows cyclic voltammetry data for "thick film" Pt@cPIM catalyst for the reduction of oxygen saturated 0.1 M phosphate buffer pH 7 (trace iii). The reduction peak is detected at about 0.0 V vs. SCE. When comparing with the reduction of 2 mM H_2O_2 in argon-degassed solution a similar reduction response is observed (trace ii) in addition to the voltammetric signal for the corresponding H_2O_2 oxidation. It seems likely that the reduction of oxygen under these conditions occurs predominantly with H_2O as product (4-electron, see equation 8.1). Fig.8.6B shows data for the corresponding processes at a 2 mm diameter Pt disk electrode confirming the assigned mechanism.

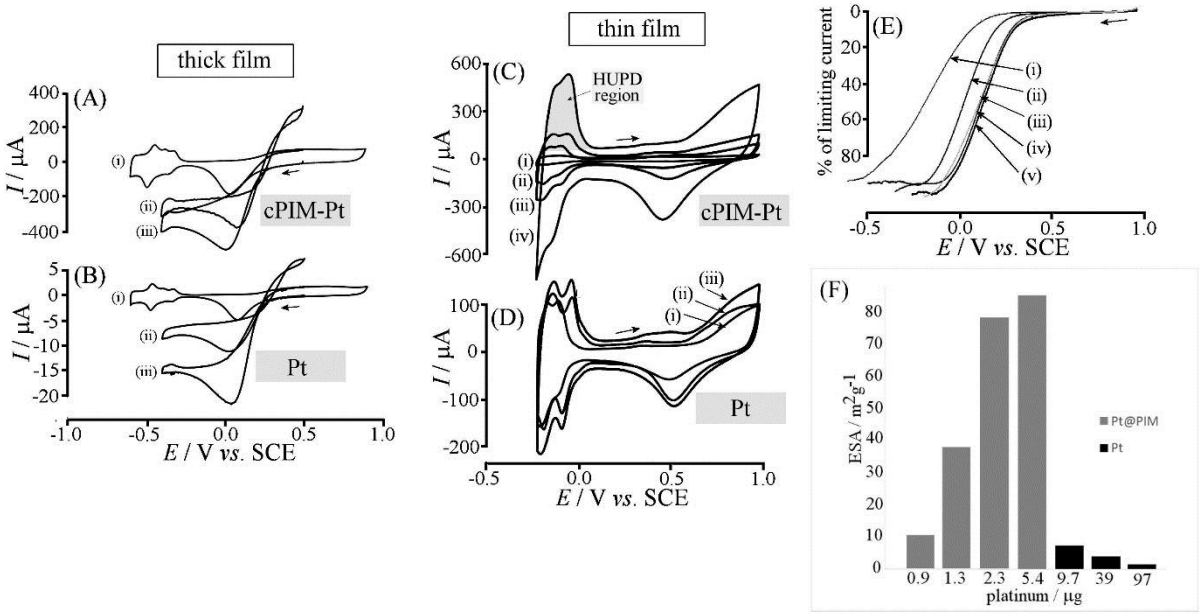

Figure 8.6. (A) Cyclic voltammograms (scan rate 50 mVs^{-1}; 1 cm^2 thick Pt@cPIM) for (i) argon-degassed solution, (ii) 2 mM H_2O_2, and (iii) oxygen-saturated in 0.1 M phosphate buffer pH 7 for thick film Pt@cPIM. (B) As above for a 2 mm diameter Pt disc electrode. (C) Cyclic voltammograms (scan rate 100 mVs^{-1}; 2.2 cm^2 thin Pt@cPIM) for argon-degassed 0.1 M $HClO_4$ for (i) 0.9, (ii) 1.3, (iii) 2.3, and (iv) 5.4 μg Pt and (D) pure Pt deposits for (i) 9.7, (ii) 39, and (iii) 97 μg Pt. (E) Normalised cyclic voltammograms for the reduction of oxygen in 0.1 M perchloric acid for thin Pt@cPIM (i) 0.9, (ii) 1.3, (iii) 2.3, and (iv) 5.4 μg Pt and (v) for pure Pt deposit 9.7 μg Pt. (F) Plot of electrochemically active surface area (ESA, estimated from HUPD region assuming 210 $\mu C\ cm^{-2}$) versus platinum amount deposited.

Figure 8.6C shows cyclic voltammetry data obtained with "thin film" Pt@cPIM with increasing film thickness and platinum coverage values of (i) 0.9, (ii) 1.3, (iii) 2.3, and (iv) 5.4 μg cm^{-2} Pt. The surface area of platinum increases systematically with Pt@cPIM film thickness as seen from the hydrogen-UPD region (see Fig.8.6C) and the oxide region. Similar experiments without PIM were performed by directly depositing H_2PtCl_6 platinum precursor onto ITO and thermal conversion without polymer (Fig.8.6D). For this set of samples surface area of platinum can be seen to remain well below that observed for Pt@cPIM. Accordingly, the surface area and therefore the catalytic activity/utilisation of Pt@cPIM are much improved due to the templating effect of the polymer. Fig.8.6E shows data for the reduction of oxygen under gentle hydrodynamic agitation (bubbling oxygen). The catalytic effect of approximately 2.3 μg (or ca. 1 μg cm^{-2}) Pt in Pt@cPIM approaches that of bare platinum.

The electrochemically active surface area (ESA) for platinum nanoparticles was estimated by cyclic voltammetry in 0.1 M $HClO_4$ solution (saturated with argon). Figure 6C shows characteristic peaks for hydrogen adsorption (H_{ads}) at -0.09 V and -0.17 V vs SCE. The ESA value can be calculated by measurement of charge under the hydrogen electro-adsorption curve (Q_H) using equation 8.2[40].

$$ESA = \frac{Q_H}{Q_{ref}} = \frac{Q_H}{210\ \mu C\ cm^{-2}} \qquad (8.2)$$

Data are summarised in Fig.8.6F. The ESA value for platinum nanoparticles supported on carbonized PIM is substantially higher compared to that for platinum produced without PIM. Data for ESA and for catalytic activity are also summarised in Table 8.2. Note that the ESA relative to the geometric surface area of the electrode reaches unity at about 1-2 μg cm^{-2}. That is a 1-2 μg cm^{-2} deposit offers a platinum surface similar to a bare platinum electrode.

Table 2. Summary of film deposits in terms of specific electrochemical surface area (ESA), ESA relative to geometric surface area, and methanol oxidation peak currents (see below).

Amount of Pt / μg (on a 15 mm × 15 mm ITO)	0.9	1.3	2.3	5.4	9.8	39	97.5
ESA / $m^2\ g^{-1}$	10.6	38.0	78.4	84.5	7.5	4.1	1.6
ESA [a] / $m^2\ m^{-2}$	0.04	0.23	0.83	2.07	0.32	0.71	0.67
I_{peak} [b] / uA	85	249	1675	3827	665	1353	1352
i_{peak} [b] /A m^{-2}	0.38	1.11	7.44	17.0	2.96	6.01	6.01
Specific catalytic current / A g^{-1}	93	191	728	708	68	35	14

[a] area of platinum per geometric surface area of the electrode

[b] anodic peak current for 1 M methanol in 0.1 M $HClO_4$ during forward scan with 50 mV s^{-1} scan rate (see Fig.8.7).

8.3.4 Electrocatalytic Methanol Oxidation

Next, the reactivity of Pt@cPIM towards methanol oxidation is investigated. Small molecules[41,42] and in particular methanol oxidation to CO_2 (equation 8.3) has been extensively studied as a fuel cell process[43,44]. Platinum is commonly employed as catalyst in methanol fuel cell devices[45].

$$CH_3OH(aq) \rightarrow CH_2O(aq) + 2\ H^+(aq) + 2\ e^-(m) \quad (8.3a)$$

$$CH_2O(aq) \rightarrow HCOOH(aq) + 2\ H^+(aq) + 2\ e^-(m) \quad (8.3b)$$

$$HCOOH(aq) \rightarrow CO_2(aq) + 2\ H^+(aq) + 2\ e^-(m) \quad (8.3c)$$

Figure 8.7A shows cyclic voltammetry data for the oxidation of 1 M methanol in aqueous 0.1 M $HClO_4$ at "thin film" Pt@cPIM catalyst with (i) 0.9, (ii) 1.3, (iv) 2.3, and (v) 5.4 μg Pt. Trace (iii) shows data for a 39 μg Pt deposit without PIM support. Figure 7B shows data for only

platinum deposited from precursor onto ITO. The inset shows a plot correlating the peak current for methanol oxidation with the amount of Pt in Pt@cPIM. At substantially lower loading with Pt the Pt@cPIM catalyst performs substantially better. Figure 8.7E compares catalytic current per gram of platinum to give a measure of specific catalytic efficiency. A loading of 2.3 or 5.4 μg platinum appears to give the most effective methanol oxidation catalysts.

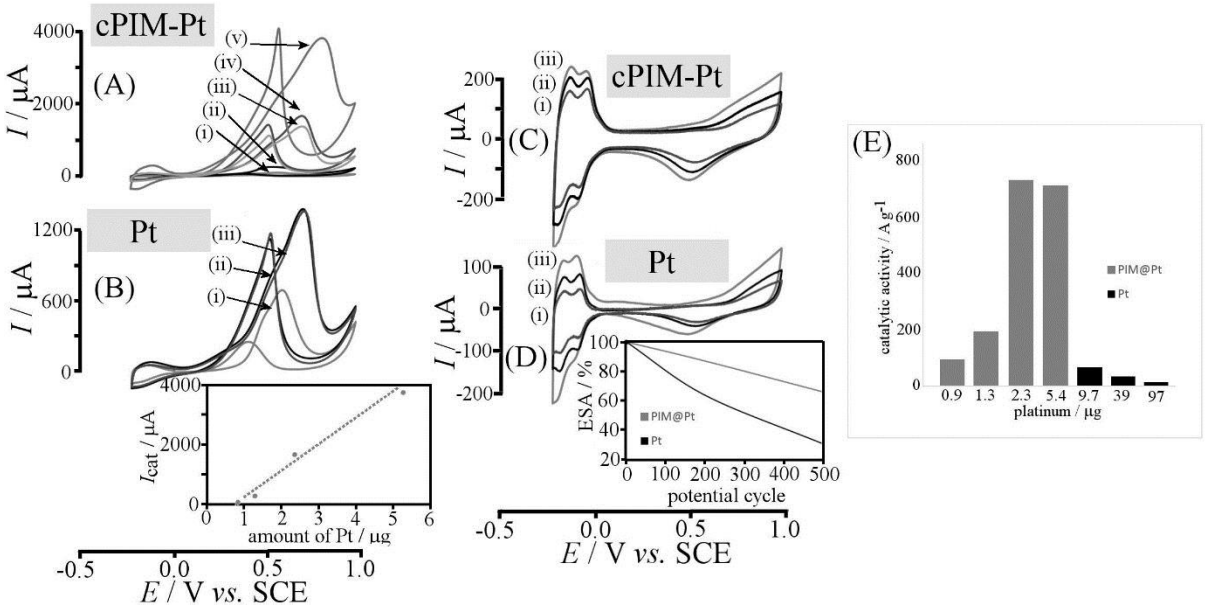

Figure 8.7. Cyclic voltammograms (scan rate 50 mVs^{-1}) for the oxidation of 1 M methanol in 0.1 M perchloric acid (A) at thin film Pt@cPIM with (i) 0.9, (ii) 1.3, (iv) 2.3, and (v) 5.4 μg Pt and (iii) 39 μg pure Pt and (B) at pure Pt deposits for (i) 9.7, (ii) 39, and (iii) 97 μg Pt. Inset shows catalytic methanol oxidation current versus amount of Pt for thin film Pt@cPIM. (C) Accelerated degradation testing (multi-cycle voltammograms with scan rate 50 mVs^{-1}) performed in 0.1 M perchloric acid for Pt@cPIM and (D) for pure Pt deposit. The inset shows the loss of active platinum surface area. (E) Plot of the specific mass activity versus amount of Pt for different types of electrodes on ITO.

Additional experiments were performed to investigate the accelerated degradation of platinum catalyst under conditions of continuous potential cycling in aqueous 0.1 M $HClO_4$ (Fig.8.7C and 8.7D). Over 500 consecutive potential cycles the Pt@cPIM catalyst performs substantially better (ca. 30 % loss of Pt activity) compared to the directly deposited Pt (ca. 70 % loss of Pt activity).

8.3.5 Electrocatalytic Glucose Oxidation

Glucose oxidation occurs on platinum electrode surfaces (mainly on catalytically active 100 surfaces) at relatively negative potentials within the hydrogen UPD region. The reaction mechanism is complex, but the main process has been suggested to be associated with a 2-electron transformation from glucose to gluconic acid or gluconolactone[46] (equation 8.4).

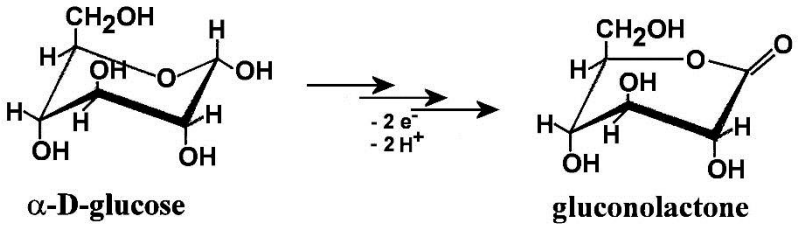

α-D-glucose gluconolactone

(8.4)

Figure 8.8A shows cyclic voltammetry data for the oxidation of 10 mM glucose in 0.1 M phosphate buffer pH 7 as a function of scan rate. A first oxidation peak is observed at -0.4 V vs. SCE consistent with literature reports[47]. This oxidation peak seems to originate from the (111)×(100) UPD region which in turn implies that hydrogen adsorption onto the platinum surface is an intermediate reaction step in the process described by equation 3. In Figure 8B data obtained at a bare 2 mm diameter Pt disk electrode is shown and very similar features are observed. Figure 8.8C and 8.8D report the effect of changing the glucose concentration over a range from 2 to 14 mM in 0.1 M phosphate buffer pH 7. Well-defined peak currents are detected that correlate with glucose concentration up to approximately 10 mM. Beyond this point the current becomes independent of the glucose concentration due to a lack of reactive surface sites. Both cPIM-Pt and bare platinum exhibit very similar trends when currents are normalised according to surface area (ESA). The difference in relative magnitude of the catalytic currents (ca. 1:100) at bare platinum and cPIM-Pt can be explained based on the electrochemically active surface area (ESA), which is ca. 4.3 cm^2 for thick film cPIM-Pt compared to 0.04 cm^2 for a 2 mm diameter platinum disk.

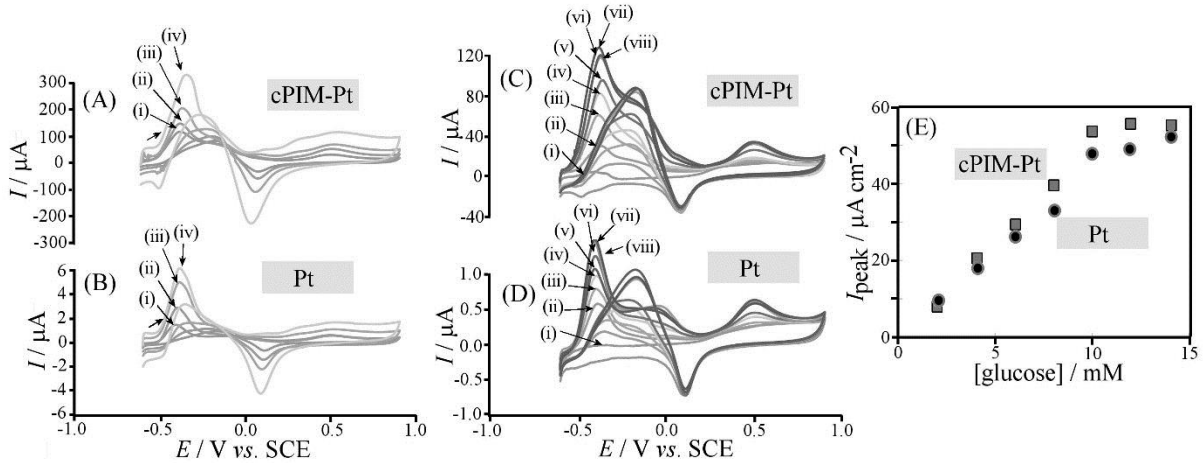

Figure 8. 8. Cyclic voltammograms (scan rate (i) 5, (ii) 10, (iii) 20, (iv) 50 mVs^{-1}) for the oxidation of 10 mM glucose in 0.1 M phosphate buffer pH 7 (A) at a thick film Pt@cPIM electrode and (B) at a bare 2 mm diameter Pt disk electrode. Next, cyclic voltammograms for the oxidation of (i) 0, (ii) 2, (iii) 4, (iv) 6, (v) 8, (vi) 10, (vii) 12, (viii) 14 mM glucose in 0.1 M phosphate buffer pH 7 at (C) thick film Pt@cPIM and (D) a bare 2 mm diameter Pt disk electrode. (E) Plot of the normalised peak current density for glucose oxidation (based on ESA) versus glucose concentration.

The oxidation of glucose on platinum is known to be very sensitive to poisons such as chloride[48,49] and even phosphate. The effect of adding chloride is demonstrated in Figure 8.9A and 8.9B for Pt@cPIM and for bare Pt, respectively. Both types of catalyst show substantial loss of activity in the presence of chloride. This needs to be taken into consideration in particular when using SCE reference electrodes, which tend to "leak" some chloride with time, in addition, phosphate buffer concentration effects the catalyst performance. Figure 8.9C and 8.9D show data for the oxidation of glucose in (i) 1.0, (ii) 0.1, and (iii) 0.01 M phosphate buffer pH 7. Both types of electrodes show similar trends with much improved catalysis at lower phosphate buffer concentration.

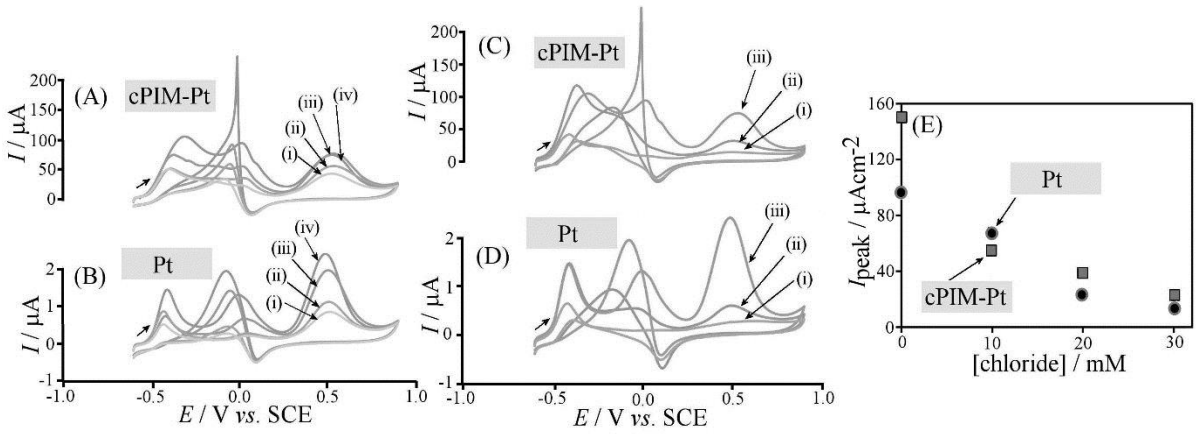

Figure 8.9. Cyclic voltammograms (scan rate 50 mVs^{-1}) for the oxidation of glucose in 0.1 M phosphate buffer pH 7 in the presence of (i) 0, (ii) 10, (iii) 20, (iv) 30 mM chloride (NaCl) at (A) thick film cPIM-Pt and (B) bare 2 mm diameter platinum. Next, cyclic voltammograms (scan rate 50 mVs^{-1}) for the oxidation of 10 mM glucose in aqueous (i) 1.0 M, (ii) 0.1 M, (iii) 0.01 M phosphate buffer pH 7 at (C) thick film cPIM-Pt and (D) bare 2 mm diameter platinum disk. (E) Plot of the catalytic glucose oxidation current peak density (based on ESA) versus chloride concentration.

Based on these data, it can be suggested that the microporous cPIM catalyst support for both thick film and thin film cases offers (i) sufficient electrical conductivity to allow catalysis at platinum nanoparticles, (ii) negligible surface blocking effects for embedded nanoparticles, and (iii) sufficient porosity to allow oxygen, methanol, glucose and similar small molecules access to the embedded catalyst nanoparticles.

8.4 Conclusion

It has been demonstrated that PIM-EA-TB can be employed to immobilise a $PtCl_6^{2-}$ precursor for platinum by simple absorption from aqueous solution. Gentle vacuum carbonization then allows platinum nanoparticle catalyst of 1.0-2.5 nm diameter to be formed. The substrate is converted to a microporous hetero-carbon with the ability to conduct electrons and without the problem of blockage of catalytic sites on platinum. Three types of relevant redox processes were investigated: (i) the reduction of oxygen, (ii) the oxidation of methanol and (iii) the oxidation of glucose. For each case, good performance of the Pt@cPIM nano-catalyst is observed. A coverage of typically 1 µg cm^{-2} of Pt provided by Pt@cPIM appears to be as catalytically reactivity as bare platinum. This estimate can be compared to the geometric area

calculated for an amount of platinum of ~ 1 μg cm^{-2} in the form of platinum nanoparticles of 2.5 nm diameter. This would indeed result in approximately 1 cm^2 geometric surface area. Therefore cPIM-Pt appears to provide *maximum* utilisation with all particles accessible and active. At this stage, many experimental parameters remain unexplored and further study of platinum loading, carbonization conditions, and different types of PIMs will be necessary.

We anticipate that the vacuum carbonization of PIMs with a range of different catalyst precursors will provide a general methodology for the production of high performance catalysts for various applications in electrochemistry. Instead of directly coating electrodes with films of PIM precursors, it will be beneficial to prepare bulk catalyst materials, which are then employed as an ink to apply to suitable electrode surfaces. The rigidity in the molecular backbone of PIMs ensures minimal loss of catalyst surface activity whilst high temperature carbonization allows the metal catalyst to form and restructures the matrix to an electrically conducting but still microporous substrate. Further work is planned to explore other types of reactions and applications.

8.5 References

1 H. Mistry, A. S. Varela, S. Kuhl, P. Strasser and B. R. Cuenya, *Nat. Rev. Mater*, 2016, **1**, 16009.

2 M. Zhou and S. Guo, *ChemCatChem*, 2015, **7**, 2744–2764.

3 Y. Xu and B. Zhang, *Chem. Soc. Rev.*, 2014, **43**, 2439–50.

4 S. Sharma and B. G. Pollet, *J. Power Sources*, 2012, **208**, 96–119.

5 J. Biener, M. Stadermann, M. Suss, M. A. Worsley, M. M. Biener, K. A. Rose, T. F. Baumann, J. S. King and A. Wittstock, *Energy Environ. Sci.*, 2011, **4**, 656.

6 W. Xia, A. Mahmood, R. Zou and Q. Xu, *Energy Environ. Sci.*, 2015, **8**, 1837–1866.

7 L. Liu, Y. P. Zhu, M. Su and Z. Y. Yuan, *ChemCatChem*, 2015, **7**, 2765–2787.

8 C. R. Kim, T. Uemura and S. Kitagawa, *Chem. Soc. Rev.*, 2016, **45**, 1–18.

9 Q. Li, N. Mahmood, J. Zhu, Y. Hou and S. Sun, *Nano Today*, 2014, **9**, 668–683.

10 P. Xu, X. Han, B. Zhang, Y. Du and H.-L. Wang, *Chem. Soc. Rev.*, 2014, **43**, 1349–60.

11 H. Fan and W. Shen, *ChemSusChem*, 2015, **8**, 2004–2027.

12 Z.-L. Xie and D. S. Su, *Eur. J. Inorg. Chem.*, 2015, **2015**, 1137–1147.

13 L. Su, W. Jia, C.-M. Li and Y. Lei, *ChemSusChem*, 2014, **7**, 361–78.

14 R. N. Singh, R. Awasthi and C. S. Sharma, *Int. J. Electrochem. Sci*, 2014, **9**, 5607–5639.

15 A. Brouzgou and P. Tsiakaras, *Top. Catal.*, 2015, **58**, 1311–1327.

16 M. Wu and T. Ma, *J. Phys. Chem. C*, 2014, **118**, 16727–16742.

17 S. Marini, P. Salvi, P. Nelli, R. Pesenti, M. Villa, M. Berrettoni, G. Zangari and Y. Kiros, *Electrochim. Acta*, 2012, **82**, 384–391.

18 E. Antolini, *Appl. Catal. B Environ.*, 2016, **181**, 298–313.

19 L. Li, L. Hu, J. Li and Z. Wei, *Nano Res.*, 2015, **8**, 418–440.

20 D. He, Y. Rong, M. Carta, R. Malpass-Evans, N. B. McKeown and F. Marken, *RSC Adv.*, 2016, **6**, 9315–9319.

21 D. He, Y. Rong, Z. Kou, S. Mu, T. Peng, R. Malpass-Evans, M. Carta, N. B. McKeown and F. Marken, *Electrochem. commun.*, 2015, **59**, 72–76.

22 W. Xia, A. Mahmood, Z. Liang, R. Zou and S. Guo, *Angew. Chemie - Int. Ed.*, 2016, **55**, 2650–2676.

23 A. Afraz, A. A. Rafati, A. Hajian and M. Khoshnood, *Electrocatalysis*, 2015, **6**, 220–228.

24 T. Xue, Z. P. Sun, L. Wei, X. Wang and J. M. Lee, *Int. J. Hydrogen Energy*, 2013, **38**, 2754–2759.

25 Y. Rong, D. He, A. Sanchez-fernandez, C. Evans, K. J. Edler, R. Malpass-evans, M. Carta, N. B. Mckeown, T. J. Clarke, S. H. Taylor, A. J. Wain, J. M. Mitchels and F. Marken, *Langmuir*, 2015, **31**, 12300–12306.

26 N. B. Mckeown and P. M. Budd, *Chem. Soc. Rev.*, 2006, **35**, 675–683.

27 N. B. McKeown and P. M. Budd, *Macromolecules*, 2010, **43**, 5163–5176.

28 N. B. McKeown, P. M. Budd, K. J. Msayib, B. S. Ghanem, H. J. Kingston, C. E. Tattershall, S. Makhseed, K. J. Reynolds and D. Fritsch, *Chem. - A Eur. J.*, 2005, **11**, 2610–2620.

29 S. Kim and Y. M. Lee, *Prog. Polym. Sci.*, 2015, **43**, 1–32.

30 Y. Rong, R. Malpass-evans, M. Carta, N. B. Mckeown, G. A. Attard and F. Marken, *Electrochem. commun.*, 2014, **46**, 26–29.

31 E. Madrid, Y. Rong, M. Carta, N. B. McKeown, R. Malpass-Evans, G. A. Attard, T. J. Clarke, S. H. Taylor, Y. T. Long and F. Marken, *Angew. Chemie*, 2014, **53**, 10751–10754.

32 Y. Rong, R. Malpass-Evans, M. Carta, N. B. Mckeown, G. A. Attard and F. Marken, *Electroanalysis*, 2014, **26**, 904–909.

33 M. Carta, R. Malpass-Evans, M. Croad, Y. Rogan, J. C. Jansen, P. Bernardo, F. Bazzarelli and N. B. McKewon, *Science (80-.).*, 2013, **339**, 303–307.

34 Y. Rogan, R. Malpass-Evans, M. Carta, M. Lee, J. C. Jansen, P. Bernardo, G. Clarizia, E. Tocci, K. Friess, M. Lanč and N. B. McKeown, *Chem. Eng. Res. Bull.*, 2014, **2**, 4874.

35 J. Xie, Q. Zhang, W. Zhou, J. Y. Lee and D. I. C. Wang, *Langmuir*, 2009, **25**, 6454–6459.

36 A. Drelinkiewicz, J. W. Sobczak, E. Sobczak, M. Krawczyk, A. Zieba and A. Waksmundzka-Góra, *Mater. Chem. Phys.*, 2009, **114**, 763–773.

37 J. M. Kinyanjui, R. Harris-burr, J. G. Wagner, N. R. Wijeratne and D. W. Hatchett,

Macromolecules, 2004, **37**, 8745–8753.

38 M. Shao, Q. Chang, J.-P. Dodelet and R. Chenitz, *Chem. Rev.*, 2016, **116**, 3594–3657.

39 V. Stamenkovic, N. M. Markovic and J. Ross P.N., *J. Electroanal. Chem.*, 2001, **500**, 44–51.

40 C. E. Hotchen, G. A. Attard, S. D. Bull and F. Marken, *Electrochim. Acta*, 2014, **137**, 484–488.

41 J. Jiang and A. Kucernak, *J. Electroanal. Chem.*, 2003, **543**, 187–199.

42 J. Jiang and A. Kucernak, *J. Electroanal. Chem.*, 2002, **533**, 153–165.

43 J. N. Tiwari, R. N. Tiwari, G. Singh and K. S. Kim, *Nano Energy*, 2013, **2**, 553–578.

44 D. S. Falcão, V. B. Oliveira, C. M. Rangel and A. M. F. R. Pinto, *Renew. Sustain. Energy Rev.*, 2014, **34**, 58–70.

45 Y. W. Lee, S. Cha, K. W. Park, J. I. Sohn and J. M. Kim, *J. Nanomater.*, 2015, **2015**.

46 S. Park, H. Boo and T. D. Chung, *Anal. Chim. Acta*, 2006, **556**, 46–57.

47 Y. Holade, C. Morais, K. Servat, T. W. Napporn and K. B. Kokoh, *Phys. Chem. Chem. Phys.*, 2014, **16**, 25609–20.

48 N. Job, M. Chatenet, S. Berthon-Fabry, S. Hermans and F. Maillard, *J. Power Sources*, 2013, **240**, 294–305.

49 J. Weber, A. J. Wain, G. A. Attard and F. Marken, *Electroanalysis*, 2016, 1–8.

Chapter 9: Summary, Conclusion, and Future Work

Polymers of intrinsic microporosity (PIMs) were first synthesised about ten years ago and, as a new calls of microporous material, they have received much attention because of their outstanding properties and wide potential for applications in gas separation, gas storage, sensing, energy storage etc. Microporous materials may introduce interesting and novel effects and functionality also in electrochemical technology. Therefore, one aim of this thesis was to explore the properties of PIMs in view of electrochemical energy technology and sensing. In exploratory work a completely new class of materials (PIMs) is brought into electrochemical technology (fuel cells, sensing, electrosynthesis, solar cells, etc.). Most experimental work was performed with PIM-EA-TB, which is one of the most interesting PIMs with a highly rigid and contorted molecular structure to generate permanent microporosity and with a high surface area of around 1000 m^2 g^{-1}. Here, the fundamental electrochemical properties and the potential application of PIM-EA-TB are investigated chapter-by-chapter.

In Chapter 3, PIM-EA-TB is demonstrated to act as an effective protection layer for nano-particulate catalysts. The intrinsic micropores are beneficial for the selection of species with different sizes. It can block the access to the catalyst for interfering species with big molecular sizes and thereby suppress poisoning from proteins. When protonated, PIM-EA-TB exhibits some degree of anion selectivity. This can be exploited to reduce the access of chloride to the catalyst surface in competition with other species, so the catalysts (here gold nanoparticles) are able to work effectively in higher chloride concentration. In future, efforts will be made to improve the micropore structure of PIMs to give better selectivity and performance.

In Chapter 4, PIM-EA-TB was successfully used to immobilise a water-insoluble molecular catalyst. Tetraphenylporphyrinato iron(III) (FeTPP) was hosted in the PIM-EA-TB film. Oxygen reduction and hydrogen peroxide oxidation/reduction were demonstrated with FeTPP as catalyst embedded in a PIM-EA-TB film. The density of the catalysts and the pH had a significant effect on the catalytic performance. A novel organogel film was made by adding 4-(3-phenyl-propyl)-pyridine (PPP) to record the electrolysis of FeTPP under liquid|liquid ion transfer voltammetry conditions. This example offers the possibility for the molecular catalysts to be hosted by PIMs in a separate phase for further investigation and applications in sensing.

In Chapter 5, PIM-EA-TB was employed to immobilise redox active ferrocene to allow stable redox cycling without loss of reagent into the solution phase. Different types of anions were compared with perchlorate and BF_4^- enhancing processes due to the lower dehydration energy. The effect of anions was also investigated in the protonation and proton transport processes in the PIM-EA-TB films, especially for perchlorate. The ionic diode effect was observed for thick PIM-EA-TB membranes in membrane voltammetry experiments. Further applications will be possible in electroanalysis (e.g. selectivity to different molecular species) and in energy harvesting.

In Chapter 6, extremely thin PIM-EA-TB membranes were produced by floating and transfer, to investigate the ionic diode effect in membrane covered microholes. The change of pH of the electrolyte led to the switch in ionic diode polarity. The mechanism behind this novel phenomenon was suggested to be associated with the ion mobility difference in the PIM-EA-TB film and protonation causing a switch from mixed ion conduction to anion conduction. An additional current was observed in the "open" side of the diode by changing the relative solution pressure, which was explained by a mechanical valve effect of the PIM membrane. Further work is needed to identify the ion transport process in PIM films and to develop a better insight into the ionic diode effect.

In Chapter 7, a novel heterocarbon was produced based on the vacuum carbonization of PIM-EA-TB. The rigid backbone structure and the intrinsic microporosity in the precursor material remained after carbonization. The resulting new carbonized PIM (or cPIM) exhibited high capacitance and interestingly, the capacitance was observed to change at different pH values. This could be attributed to the protonation of nitrogen sites. Carbonized PIM-EA-TB was demonstrated to be inert towards electron transfer to oxygen and hydrogen peroxide, which was not common for carbon materials and probably caused of the lack of reactive electron transfer sites in cPIM. Further work will be required to determine the effect of different parameters such as carbonization temperature and molecular precursor structure on the properties of resulting microporous carbon.

In Chapter 8, a general methodology for production of metal nanoparticles was developed based on a PIM-EA-TB precursor that is carbonized with metal ($PtCl_6^{2-}$) adsorbed. Uniform 1.0-2.5 nm platinum nanoparticles were formed automatically in the matrix of carbonized PIM. The amount of platinum could be controlled by changing the thickness of PIM films. The microporous structure of PIM ensures the maximum utilization of platinum nanoparticles. The rigid molecular structure of PIM-EA-TB seemed to suppress catalyst surface blocking and therefore a very high level of utilisation was achieved. An amount of 1 μg of platinum nanoparticles embedded in cPIM (or Pt@cPIM) was determined to possess around 1 cm^2 electrochemically active surface area. Three redox processes studied included oxygen reduction, methanol oxidation, and glucose oxidation. Compared with bulk platinum, a much better utilisation of catalyst was observed for platinum nanoparticles in Pt@cPIM, which is linked to the high surface area of the nanoparticles. This "one-step" methodology offers the possibility to produce different kinds of highly reactive metal nanoparticles and alloys in order to improve the performance and stability of catalysts.

In summary, PIM-EA-TB was introduced into the field of electrochemistry and investigated for new applications for catalytic electrodes and in ion transporting membranes. Further research will be needed to fully understand the underlying mechanisms and to improve the performance of PIM-EA-TB. Compared with other amorphous nanoporous structures, PIMs are chemically well-defined materials and easily processible, which can be a major benefit. The rigidity of the molecular structure and the intrinsic microporosity play the key role to the exceptional properties of PIMs. Further efforts will be necessary to first understand the relationship between the properties and molecular structure and then optimise the synthesis of PIMs to provide pore shape control and pore size distribution as well as pore charge control. In future, PIMs are likely to offer new microporous materials solutions in particular in electrochemical sensing and energy conversion and storage.